
The semi-analytic theory and computation of finite-depth standing water waves

Ahmad Abassi · Jon Wilkening

December 30, 2024

Abstract We propose a Stokes expansion ansatz for finite-depth standing water waves in two dimensions and devise a recursive algorithm to compute the expansion coefficients. We implement the algorithm on a supercomputer using arbitrary-precision arithmetic. The Stokes expansion introduces hyperbolic terms that require exponentiation of power series, which we handle efficiently using Bell polynomials. Although exact resonances occur at a countable dense set of fluid depths, we prove that for almost every depth, the divisors that arise in the recurrence are bounded away from zero by a slowly decaying function of the wave number. A direct connection between small divisors and imperfect bifurcations is observed. They are found to activate secondary standing waves that oscillate non-uniformly in space and time on top of the primary wave, with different amplitudes and phases on each bifurcation branch. We compute new families of standing waves using a shooting method and find that Padé approximants of the Stokes expansion continue to converge to the shooting method solutions at large amplitudes as new small divisors enter the recurrence. Closely spaced poles and zeros of the Padé approximants are observed that suggest that the bifurcation branches are separated by branch cuts.

Keywords standing water waves · finite depth · Stokes expansion · conformal map · bifurcation · Padé approximation

MSC Classification 76B15, 35C20, 37G15, 65N22, 65N35, 68W10

1 Introduction

Standing water waves have a long scientific history dating back at least to 1831, when Faraday observed beautiful patterns of ink at the surface of milk driven by a tuning force. Standing waves in the ocean are believed to be responsible for microseisms [1,2] and can play an important role in the dynamics of wave breaking [3]. Their resonances must be accounted for in the design of oscillating wave energy converters [4] and breakwaters

A. Abassi
Department of Mathematics, University of California, Berkeley, CA 94720-3840
E-mail: zaid_abassi@berkeley.edu

J. Wilkening
Department of Mathematics, University of California, Berkeley, CA 94720-3840
E-mail: wilkening@berkeley.edu

[5] to maximize efficiency and minimize violent impacts during storms. Two-dimensional standing waves can be viewed as symmetric, time-periodic solutions of the free-surface Euler equations in an enclosed container [6] or as a superposition of identical counter-propagating spatially periodic traveling waves [7,8]. Low-order perturbation expansion techniques for standing waves were developed by Penney and Price [6], Tadjbakhsh and Keller [9] (considering the finite-depth case), Concus [10,11] (considering the effects of surface tension), and Verma and Keller [12] (considering standing waves in rectangular three-dimensional containers). Roberts [13] and Marchant and Roberts [14] carried out high-order perturbation expansions numerically to study short-crested waves, which include standing waves as a special case.

For the infinite-depth case with zero surface tension, Schwartz and Whitney [15] proposed an arbitrary-order semi-analytic theory of standing waves using a conformal mapping formulation of the equations. They computed their expansions to 29th order in quadruple-precision floating-point arithmetic. Amick and Toland [16] devised an ingenious implicit function theorem argument to prove the ‘‘Schwartz and Whitney conjecture’’ that their algorithm does not break down. They showed that although there are infinitely many exact resonances, each resonant equation is solvable the first time it enters the system, and the free parameter associated with each resonance is uniquely determined by the solvability condition at the next higher order. Iooss presented an alternative proof of the Schwartz and Whitney conjecture based on normal forms [17] and generalized the results to the case of several dominant modes.

An important open question that was not resolved by Amick and Toland is whether the coefficients in these formal asymptotic expansions grow slowly enough that the resulting series has a positive radius of convergence. In the present paper, we generalize the Schwartz and Whitney algorithm to handle standing waves of finite depth and explore the growth rates of the coefficients of the Stokes expansion through numerical computation. In [18], we will show how to include the effects of surface tension in infinite depth. Each step of these recursive algorithms involves computing forcing terms that arise from lower-order terms in the expansion and dividing them by the numbers

$$\lambda_{p,j} = p \frac{\tanh(p\mu_0)}{\tanh \mu_0} - j^2 \quad \text{or} \quad \lambda_{p,j}^{\text{cap}} = \frac{1 + Bp^2}{1 + B} p - j^2, \quad (1.1)$$

where the first formula is for the finite depth case while the second is for gravity-capillary waves in infinite depth [18]. Here μ_0 is a dimensionless fluid depth parameter, $B = \frac{4\pi^2\tau}{\rho g L^2}$ is the (inverse) Bond number [19], τ is the surface tension, ρ is the fluid density, L is the wavelength, g is the acceleration of gravity, and the integers p and j are the wave number and angular frequency of the mode being computed (after non-dimensionalization).

In infinite depth with zero surface tension ($B = 0$), every pair (p, j) with $p = j^2$ leads to a zero divisor that has to be treated specially [15,16,18]. Zero divisors also arise at specific finite depths. Physically, $\lambda_{p,j} = 0$ means that within linear water wave theory, the frequency of the p th spatial harmonic is an integer multiple, j , of the fundamental frequency. An interesting feature of standing waves is that these resonant depths form a countable dense subset of the positive real numbers [11]. We make a new observation that this does not automatically imply that for all depths, the divisors in (1.1) become small. For example, for the gravity-capillary wave problem, when $B = 1$, we use a result from elliptic curve theory [20] to show that $|\lambda_{p,j}^{\text{cap}}| \geq 1$ for $p \geq 2$ and $j \in \mathbb{Z} = \{0, \pm 1, \pm 2, \dots\}$, even though there is a sequence of resonant Bond numbers that converges to $B = 1$. In the finite depth problem, we find that there are no depths where $\lambda_{p,j}$ is bounded away from zero, but for

every $\delta > 0$ and almost every fluid depth (in the Lebesgue sense), there is an $a > 0$ such that $|\lambda_{p,j}| \geq \min(a, p^{-1/2-\delta})$ for all $p \geq 2$ and $j \in \mathbb{Z}$. While this lower bound presumably does not ensure a positive radius of convergence, it limits the growth rate of the Stokes expansion coefficients sufficiently that Padé approximants of the Stokes expansion appear to be convergent at large amplitudes in our numerical experiments.

For both traveling waves [21,22,23,24] and standing waves [25,26,27,28,29,30], harmonic resonance leads to non-uniqueness. Combination waves [21] with multiple dominant modes co-exist with pure waves of one dominant mode, and there are often perfect or imperfect bifurcations connecting the various families. The resulting branching behavior of standing waves near resonant depths has been studied extensively by Mercer and Roberts [26], Smith and Roberts [27], and Wilkening and Yu [29]. In the present work, we investigate the role of small divisors in the formation of these bifurcation branches. We observe sudden changes in the growth rate of the Stokes coefficients when especially small divisors $\lambda_{p,j}$ enter the recursion. We investigate this in detail for depths $\mu_0 \in \{1/4, 3/5, 1\}$. For $\mu_0 = 1$, there is a cluster of 3 small divisors that each yields an imperfect bifurcation in the solution curve computed using a shooting method [31,29]. Following the side branches associated with the (p, j) small divisor leads to visible secondary “standing waves on standing waves” with p spatial oscillations that execute j temporal oscillations over one cycle of the primary wave. Similar secondary waves have been reported in various settings [26,27,28,29,19], including standing waves in three-dimensional fluids [30]. Solutions on the side branches differ in how the amplitude and phase of the secondary wave matches up with the phase of the primary wave. We explore the effects of nonlinearity on the shapes of the secondary waves, which deviate from the sinusoidal patterns of linear water wave theory that led to the small divisors.

In a model problem, Roberts [24] showed that a nonlinear Shanks transform can extend the validity of non-resonant asymptotic expansions across discontinuities in the bifurcation curves associated with nearby harmonic resonances. We adopt this strategy and study the convergence of Padé approximants of the Stokes expansions, which continue to improve in accuracy (relative to the shooting method) as more terms are included in their continued fraction representation, even at large amplitudes where successive terms in the Stokes expansion diverge wildly. Poles in the Padé approximation allow for accurate branch jumping. We achieve errors between 10^{-32} and 10^{-27} on both sides of the first two imperfect bifurcations we observe in the $\mu_0 = 1$ case. We use the poles to locate new bifurcation branches and present a new method of identifying which harmonic resonance will be most strongly activated on each branch. We often find multiple Padé poles in gaps between turning points [27] of the wave height. This suggests that the turning points are branch points and the poles on the branch cut act as a quadrature formula to approximate a Cauchy integral with the same branch point singularity structure at its endpoints [32,33,34].

2 Preliminaries

In this section we introduce the conformal map used to represent the fluid motion in finite depth, non-dimensionalize the partial differential equations governing water waves, propose an ansatz for a Stokes expansion of the solution in powers of an amplitude parameter, derive the governing equations of the spatial Fourier modes of the solution, and show how to use Bell polynomials to efficiently re-expand the hyperbolic sine or cosine of a power series.

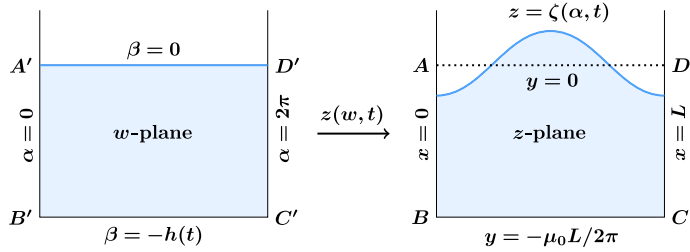


Fig. 1 The conformal map transforms conformal space (left) to physical space (right). The dotted line on the right illustrates a mean free-surface height of zero in physical space.

2.1 The conformal map and governing equations

We consider standing waves on an inviscid, irrotational, incompressible two-dimensional fluid of finite depth. We denote the velocity potential in physical space by $\phi(x, y, t)$, where the fluid velocity satisfies $\mathbf{u} = \nabla\phi$. We identify \mathbb{R}^2 with the complex plane and parameterize the free surface and surface velocity potential by

$$\zeta(\alpha, t) = \xi(\alpha, t) + i\eta(\alpha, t), \quad \varphi(\alpha, t) = \phi(\xi(\alpha, t), \eta(\alpha, t), t). \quad (2.1)$$

The kinematic condition and dynamic Bernoulli equation governing the time evolution of the free surface are

$$\begin{aligned} \zeta_t \cdot \mathbf{n} &= \mathbf{u} \cdot \mathbf{n} = \frac{\partial\phi}{\partial n}, \\ \phi_t &= -\frac{1}{2}|\nabla\phi|^2 - g\eta + C(t), \end{aligned} \quad (2.2)$$

where \mathbf{n} is the outward normal to the free surface, g is the acceleration of gravity, the subscript t is a partial derivative, and $C(t)$ is an arbitrary function of time but not space, which accounts for the fact that only gradients of the velocity potential have physical significance. This term can be set to zero, but we find that it is useful to retain it in the finite-depth problem. Here we neglect the effects of surface tension, which would introduce a curvature term in the Bernoulli equation; see [18]. The governing equation for the surface velocity potential is obtained from the Bernoulli equation using

$$\varphi_t = \phi_t + \nabla\phi \cdot \zeta_t, \quad (2.3)$$

where $\partial\phi/\partial n$ is computed from ϕ by applying the Dirichlet-Neumann operator [35].

We assume the standing wave and fluid velocity are spatially periodic with period L in physical space. In the infinite-depth case, Schwartz and Whitney [15], Amick and Toland [16], and Dyachenko et al [36] introduce a conformal map to pull back the fluid domain to the complex lower half-plane. We follow the same plan, but since the fluid depth is finite, the pre-image of the conformal map is a strip rather than a half-plane. As illustrated in figure 1, we introduce

$$w = \alpha + i\beta \quad (2.4)$$

as the spatial variable in conformal space and let

$$z(w, t) = x(w, t) + iy(w, t), \quad \zeta(\alpha, t) = z(\alpha, t) \quad (2.5)$$

denote the conformal map and its restriction to the real axis, which is mapped to the free surface of the fluid. We choose the period of the conformal domain to be fixed at 2π and

denote the lower boundary of the strip by $\beta = -h(t)$, which evolves in time [37, 38, 39]. We denote the conjugate harmonic function to ϕ in physical space by ψ , which is the stream function, and define the complex velocity potential in conformal space by

$$\Phi(w, t) = \phi(x(w, t), y(w, t), t) + i\psi(x(w, t), y(w, t), t). \quad (2.6)$$

The Cauchy-Riemann equations give $\phi_y = -\psi_x$, so

$$\mathbf{u} \cdot \mathbf{n} = (\phi_x, -\psi_x) \cdot \frac{(-\eta_\alpha, \zeta_\alpha)}{s_\alpha} = -\frac{\text{Im}\{\Phi_w\}}{s_\alpha}, \quad (2.7)$$

where $s_\alpha = |\zeta_\alpha(\alpha, t)|$ is the arclength element of the parameterization. From (2.2), (2.3), (2.6) and (2.7), we obtain

$$\begin{aligned} \zeta_\alpha \eta_t - \eta_\alpha \zeta_t &= -\text{Im}\{\Phi_w\}, \\ \partial_t \text{Re}\{\Phi\} - \text{Re}\left\{\frac{\Phi_w}{z_w} \zeta_t\right\} + \frac{1}{2} \left|\frac{\Phi_w}{z_w}\right|^2 + g\eta &= C(t). \end{aligned} \quad (2.8)$$

As shown in [39], it follows from Cauchy's theorem and the fact that z_t/z_w is an analytic function in the strip $-h(t) < \beta < 0$ that

$$h_t = -\frac{1}{2\pi} \int_0^{2\pi} \frac{\text{Im}\{\Phi_w(\alpha, t)\}}{s_\alpha^2} d\alpha. \quad (2.9)$$

In the construction of this paper, it is not necessary to impose (2.9) explicitly since it follows from (2.8) and Cauchy's theorem.

We are searching for standing water waves, which are symmetric time-periodic solutions of (2.8). Let T denote the temporal period. Following Schwartz/Whitney [15] and Amick/Toland [16], we non-dimensionalize the variables via

$$Z(w, t) = \frac{2\pi}{L} z \left(w, \frac{T}{2\pi} t \right), \quad F(w, t) = \frac{2\pi T}{L^2} \Phi \left(w, \frac{T}{2\pi} t \right), \quad S = \frac{gT^2}{2\pi L} \quad (2.10)$$

and introduce an auxiliary function, $W(w, t) = F_w/Z_w$, which, when conjugated, is a dimensionless velocity pulled back from physical to conformal space,

$$\bar{W}(w, t) = \frac{T}{L} \mathbf{u}(x(w, t), y(w, t), t). \quad (2.11)$$

Expressing (2.8) in terms of the dimensionless variables gives

$$-F_w + WZ_w = 0, \quad (-h(t) \leq \beta \leq 0), \quad (2.12a)$$

$$\text{Im}(F_\alpha - Z_\alpha \bar{Z}_t) = 0, \quad (\beta = 0), \quad (2.12b)$$

$$\text{Re}\left(F_t + \frac{1}{2} W\bar{W} - iSZ - WZ_t\right) = C(t), \quad (\beta = 0). \quad (2.12c)$$

2.2 The Stokes expansion ansatz

Building on the infinite-depth conformal mapping framework of Schwartz and Whitney [15,16] and finite-depth graph-based formulations [9,14,28], we propose the following ansatz for the Fourier representations of Z , W , and F :

$$Z(w, t) = w + ih(t) - i\mu_0 + \sum_{p=1}^{\infty} a_p(t) \frac{\sin[p(w + ih(t))]}{\cosh(p\mu_0)}, \quad (2.13a)$$

$$W(w, t) = \sum_{p=1}^{\infty} b_p(t) \frac{\sin[p(w + ih(t))]}{\cosh(p\mu_0)}, \quad (2.13b)$$

$$F(w, t) = \sum_{p=0}^{\infty} c_p(t) \frac{\cos[p(w + ih(t))]}{\cosh(p\mu_0)}. \quad (2.13c)$$

On the bottom boundary, where $w = \alpha - ih(t)$, we have

$$\frac{2\pi}{L} \operatorname{Im}\{z(w, t)\} = \operatorname{Im}\{Z(w, t)\} = -\mu_0, \quad \operatorname{Im}\{W(w, t)\} = 0, \quad \operatorname{Im}\{F(w, t)\} = 0. \quad (2.14)$$

This shows that $\mu_0 L / 2\pi$ is the fluid depth in physical space, that the vertical component of velocity is zero on the bottom boundary, and that the stream function is constant (in fact zero) on the bottom boundary, indicating that there is no fluid flux crossing this boundary.

We employ identical ϵ -expansions to those of Schwartz and Whitney [15,16] for the coefficients $a_p(t)$, $b_p(t)$ and $c_p(t)$, and for the dimensionless period parameter S . However, in the finite-depth setting we must also expand the strip width $h(t)$ in terms of the standing wave amplitude:

$$a_p(t) = \sum_{n=0}^{\infty} \alpha_{p,n}(t) \epsilon^{p+2n}, \quad b_p(t) = \sum_{n=0}^{\infty} \beta_{p,n}(t) \epsilon^{p+2n}, \quad c_p(t) = \sum_{n=0}^{\infty} \gamma_{p,n}(t) \epsilon^{p+2n}, \quad (2.15a)$$

$$S = \sum_{n=0}^{\infty} \sigma_n \epsilon^{2n}, \quad h(t) = \mu_0 + \sum_{n=1}^{\infty} \mu_n(t) \epsilon^{2n}. \quad (2.15b)$$

Here ϵ is the standing wave amplitude; the functions $\alpha_{p,n}(t)$, $\beta_{p,n}(t)$, $\gamma_{p,n}(t)$, and $\mu_n(t)$ are real-valued; the coefficients σ_n are real constants; and the coefficient μ_0 is a positive constant, the non-dimensionalized fluid depth in physical space (see figure 1 above). As in the infinite-depth problem, the amplitude is defined as half the vertical crest to trough height after non-dimensionalization, i.e.,

$$\epsilon = \frac{1}{2} \operatorname{Im} \left(Z(0, 0) - Z(\pi, 0) \right) = \sum_{m=0}^{\infty} a_{2m+1}(0) \frac{\sinh[(2m+1)h(0)]}{\cosh[(2m+1)\mu_0]}, \quad (2.16)$$

where the right-hand side must still be expanded in powers of ϵ with the coefficient of the linear term evaluating to 1 and the others evaluating to 0.

On the free surface, the sine and cosine terms in (2.13) may be written

$$\begin{aligned} \sin[p(\alpha + ih)] &= \cosh(ph) \sin(p\alpha) + i \sinh(ph) \cos(p\alpha), \\ \cos[p(\alpha + ih)] &= \cosh(ph) \cos(p\alpha) - i \sinh(ph) \sin(p\alpha), \end{aligned} \quad (2.17)$$

so the spatial Fourier coefficients of the real and imaginary parts of $Z(\alpha, t)$, $W(\alpha, t)$ and $F(\alpha, t)$ will involve products of the form

$$\frac{u_p(t) \cosh[ph(t)]}{\cosh(p\mu_0)} \quad \text{or} \quad \frac{u_p(t) \sinh[ph(t)]}{\cosh(p\mu_0)}, \quad (2.18)$$

where $u_p(t)$ represents $a_p(t)$, $b_p(t)$ or $c_p(t)$. One advantage of the conformal mapping approach over previous graph-based formulations [6,9,14,28] is that the argument $ph(t)$ of the hyperbolic functions in (2.18) is an ϵ -expansion with terms depending only on time (and not also space); see section 2.4 below. An advantage of the graph-based formulation is that it extends to three-dimensional short-crested waves [14], covering standing waves as a special case.

2.3 Time-evolution of the spatial Fourier modes

Substitution of the ansatz (2.13) in the auxiliary equation (2.12a) gives

$$\begin{aligned} \frac{(pc_p + b_p)}{\cosh(p\mu_0)} + \sum_{k=1}^{p-1} \frac{ka_k b_{p-k}}{2 \cosh(k\mu_0) \cosh[(p-k)\mu_0]} \\ + \sum_{k=1}^{\infty} \frac{ka_k b_{p+k} - (k+p)a_{k+p} b_k}{2 \cosh(k\mu_0) \cosh[(p+k)\mu_0]} = 0, \end{aligned} \quad (p \in \mathbb{N}). \quad (2.19)$$

Similarly, the kinematic free-surface equation (2.12b) gives

$$\dot{h} + \sum_{k=1}^{\infty} ka_k \dot{a}_k \frac{\sinh(2kh)}{2 \cosh^2(k\mu_0)} + \dot{h} \sum_{k=1}^{\infty} k^2 a_k^2 \frac{\cosh(2kh)}{2 \cosh^2(k\mu_0)} = 0 \quad (2.20a)$$

and

$$\begin{aligned} (\dot{a}_p - pc_p) \frac{\sinh(ph)}{\cosh(p\mu_0)} + 2\dot{h}pa_p \frac{\cosh(ph)}{\cosh(p\mu_0)} - \sum_{k=1}^{p-1} \frac{(p-k)a_{p-k} \dot{a}_k \sinh[(p-2k)h]}{2 \cosh[(p-k)\mu_0] \cosh(k\mu_0)} \\ + \sum_{k=1}^{\infty} \left((p+k)a_{p+k} \dot{a}_k + ka_k \dot{a}_{p+k} \right) \frac{\sinh[(p+2k)h]}{2 \cosh(k\mu_0) \cosh[(p+k)\mu_0]} \\ + \dot{h} \sum_{k=1}^{\infty} \left((p+k)a_{p+k} ka_k + ka_k (p+k)a_{p+k} \right) \frac{\cosh[(p+2k)h]}{2 \cosh(k\mu_0) \cosh[(p+k)\mu_0]} \\ + \dot{h} \sum_{k=1}^{p-1} (p-k)a_{p-k} ka_k \frac{\cosh[(p-2k)h]}{2 \cosh[(p-k)\mu_0] \cosh(k\mu_0)} = 0, \end{aligned} \quad (p \in \mathbb{N}), \quad (2.20b)$$

where a dot represents a time-derivative. In the Bernoulli equation (2.12c), we choose the integration constant $C(t)$ so that $\dot{c}_0 = 0$, which allows us to set $c_0(t) = 0$ and commence the series for F in (2.13c) from $p = 1$. This leads to

$$\begin{aligned} \dot{c}_p \frac{\cosh(ph)}{\cosh(p\mu_0)} + Sa_p \frac{\sinh(ph)}{\cosh(p\mu_0)} + \sum_{k=1}^{\infty} \frac{b_k b_{p+k} \cosh[(p+2k)h]}{2 \cosh(k\mu_0) \cosh[(p+k)\mu_0]} \\ - \sum_{k=1}^{p-1} \frac{b_{p-k} b_k \cosh[(p-2k)h]}{4 \cosh[(p-k)\mu_0] \cosh(k\mu_0)} - \sum_{k=1}^{\infty} \frac{b_{p+k} \dot{a}_k + b_k \dot{a}_{p+k}}{2 \cosh(k\mu_0) \cosh[(p+k)\mu_0]} \cosh(ph) \\ + \sum_{k=1}^{p-1} \frac{b_{p-k} \dot{a}_k}{2 \cosh[(p-k)\mu_0] \cosh(k\mu_0)} \cosh(ph) = 0, \end{aligned} \quad (p \in \mathbb{N}). \quad (2.21)$$

The $p = 0$ term in the ansatz $Z(w, t) = w + i \sum_{p=0}^{\infty} a_p(t) e^{-ipw}$ for the infinite-depth case [16, 18] has been replaced by $[h(t) - \mu_0]$ in (2.13a). We only need to solve for $a_p(t)$, $b_p(t)$ and $c_p(t)$ with $p \geq 1$ since we set $c_0(t) = 0$ above and $b_0(t)$ is absent in the ansatz (2.13b) due to $\sin(0) = 0$.

2.4 Bell polynomials and the exponential of a power series

In the equations of the previous section, there appear terms involving the hyperbolic sine and cosine of integer multiples of the strip width, $h(t)$, which has a Stokes expansion in powers of ϵ . An efficient formula [40] to re-expand the exponential of a power series is given by

$$\exp\left(\sum_{k=0}^{\infty} a_k x^k\right) = e^{a_0} \sum_{n=0}^{\infty} \frac{B_n(a_1 1!, \dots, a_n n!)}{n!} x^n, \quad (2.22)$$

where the complete Bell polynomials $B_n(x_1, \dots, x_n)$ are defined recursively by

$$B_0 = 1, \quad B_{n+1}(x_1, \dots, x_{n+1}) = \sum_{i=0}^n \binom{n}{i} B_{n-i}(x_1, \dots, x_{n-i}) x_{i+1}, \quad (n \geq 0). \quad (2.23)$$

For our specific setting, we need $\cosh(qh)$ and $\sinh(qh)$ for various integers $q \in \mathbb{Z}$, so we expand

$$\begin{aligned} \exp(qh) &= \sum_{n=0}^{\infty} B_{q,n}(t) \epsilon^{2n}, & B_{q,n}(t) &= \frac{e^{q\mu_0}}{n!} B_n(q\mu_1(t)1!, \dots, q\mu_n(t)n!), \\ \cosh(qh) &= \sum_{n=0}^{\infty} c_{q,n}(t) \epsilon^{2n}, & \sinh(qh) &= \sum_{n=0}^{\infty} s_{q,n}(t) \epsilon^{2n}, \end{aligned} \quad (2.24)$$

where

$$c_{q,n}(t) = \frac{B_{q,n}(t) + B_{-q,n}(t)}{2}, \quad s_{q,n}(t) = \frac{B_{q,n}(t) - B_{-q,n}(t)}{2}. \quad (2.25)$$

Using (2.23), we obtain

$$B_{q,0}(t) = e^{q\mu_0}, \quad B_{q,n}(t) = q \sum_{i=1}^n \frac{i}{n} B_{q,n-i}(t) \mu_i(t), \quad (n \geq 1). \quad (2.26)$$

Roberts [13] and Marchant and Roberts [14] derived an identical recurrence from first principles (without employing Bell polynomials) in a graph-based formulation of the short-crested wave problem. In the special case of standing waves in this graph-based approach, one has to evaluate factors of e^{qy} (infinite-depth) or $\cosh[q(\mu_0 + y)]$ (finite-depth) in the velocity potential expansion at $y = \eta^{\text{graph}}(x, t) = \sum_{\nu \geq 1} \eta_{\nu}^{\text{graph}}(x, t) \epsilon^{\nu}$. Replacing n by ν and $\mu_i(t)$ by $\eta_i^{\text{graph}}(x, t)$ in (2.26) and calling the result $\tilde{B}_{q,\nu}(x, t)$ leads to a function that depends on both x and t . $B_{q,n}(t)$ is represented by $O(n)$ temporal Fourier coefficients while $\tilde{B}_{q,\nu}(x, t)$ contains $O(\nu^2)$ non-zero Fourier modes in both time and space. Only even powers of ϵ are present in (2.24), so the sum (2.26) contains half as many terms as the corresponding sum for $\tilde{B}_{q,\nu}(x, t)$ at a given order ϵ^{ν} with $\nu = 2n$. This reduces the memory and computational costs of the data structures required to re-expand the hyperbolic functions in the conformal mapping approach of the present work.

3 ODEs for the Stokes coefficients and a recursive algorithm

Substitution of the Stokes expansions (2.15) into the equations (2.19)–(2.21) governing the time-evolution of the spatial Fourier modes yields a system of ODEs for the Stokes coefficients,

$$\dot{\mu}_n + T_{0,n}^1 = 0, \quad (\text{I})$$

$$\beta_{p,n} + p\gamma_{p,n} + T_{p,n}^2 = 0, \quad (\text{II})$$

$$\dot{\alpha}_{p,n} - p\gamma_{p,n} + T_{p,n}^3 = 0, \quad (\text{III})$$

$$\dot{\gamma}_{p,n} + \sigma_0 \tanh(p\mu_0)\alpha_{p,n} + T_{p,n}^4 = 0, \quad (\text{IV})$$

where $p \geq 1$ and $n \geq 0$. Formulas for the forcing terms $T_{p,n}^r$ are derived in the electronic supplementary material. We require that solutions of this system have certain symmetries and functional forms, namely, that $\mu_n(t)$ and $\alpha_{p,n}(t)$ are even trigonometric polynomials of the form

$$\mu_n(t) = \sum_{j \in E_{2n}} \mu_{n,j} e^{ijt} = \sum_{j=0}^{2n} \mu_{n,j} H_j \left(e^{ijt} + e^{-ijt} \right), \quad (\mu_{n,j} \in \mathbb{R}), \quad (3.1)$$

$$\alpha_{p,n}(t) = \sum_{j \in E_{p+2n}} \alpha_{p,n,j} e^{ijt} = \sum_{j=0}^{p+2n} \alpha_{p,n,j} H_j \left(e^{ijt} + e^{-ijt} \right), \quad (\alpha_{p,n,j} \in \mathbb{R}), \quad (3.2)$$

where $\mu_{n,-j} = \mu_{n,j}$, $\alpha_{p,n,-j} = \alpha_{p,n,j}$,

$$E_\nu = \{ \nu - 2m \mid 0 \leq m \leq \nu \} \\ = \{ -\nu, -\nu + 2, \dots, \nu - 2, \nu \}, \quad H_j = \begin{cases} 1/2, & j = 0, \\ 1, & j \geq 1, \end{cases} \quad (3.3)$$

and a prime on a sum indicates that terms in the given range should be included only if the summation index has the same parity as the upper limit. Moreover, $\beta_{p,n}(t)$ and $\gamma_{p,n}(t)$ are odd trigonometric polynomials of the form

$$\beta_{p,n}(t) = \sum_{j \in E_{p+2n}} i\beta_{p,n,j} e^{ijt} = i \sum_{j=1}^{p+2n} \beta_{p,n,j} \left(e^{ijt} - e^{-ijt} \right), \quad (\beta_{p,n,j} \in \mathbb{R}), \quad (3.4)$$

$$\gamma_{p,n}(t) = \sum_{j \in E_{p+2n}} i\gamma_{p,n,j} e^{ijt} = i \sum_{j=1}^{p+2n} \gamma_{p,n,j} \left(e^{ijt} - e^{-ijt} \right), \quad (\gamma_{p,n,j} \in \mathbb{R}), \quad (3.5)$$

where $\beta_{p,n,0} = \gamma_{p,n,0} = 0$, $\beta_{p,n,-j} = -\beta_{p,n,j}$, and $\gamma_{p,n,-j} = -\gamma_{p,n,j}$. The symmetry assumptions (3.1), (3.2), (3.4) and (3.5) mostly take the place of initial conditions for the ODEs, but we also need to impose

$$\alpha_{1,0}(0) = \coth(\mu_0), \quad \sum_{q=0}^n \sum_{k=0}^{n-q} \frac{\alpha_{2q+1,k}(0) s_{2q+1,n-q-k}(0)}{\cosh[(2q+1)\mu_0]} = 0, \quad (n \in \mathbb{N}), \quad (\text{i})$$

$$\mu_n(0) + \sum_{q=1}^n \sum_{k=0}^{n-q} \sum_{l=0}^{n-q-k} \frac{q}{4 \cosh^2(q\mu_0)} \alpha_{q,k}(0) \alpha_{q,l}(0) s_{2q,n-q-k-l}(0) = 0, \quad (n \in \mathbb{N}). \quad (\text{ii})$$

Here (i) is a consequence of the amplitude definition (2.16) and (ii) ensures that the fluid depth is independent of ϵ . As shown in figure 1 above, the bottom boundary is at $y =$

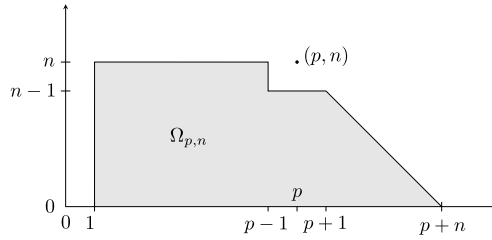


Fig. 2 The set $\Omega_{p,n}$ consists of the integer lattice points in the shaded region, including its boundary.

$-\mu_0 L/2\pi$, but we also need to specify the mean free-surface height. It is easy to show that $(\partial/\partial t) \int_0^{2\pi} \eta \zeta_\alpha d\alpha = 0$, so mass is conserved in time and the mean free-surface height will remain zero if it is zero initially. We obtain (ii) using (2.13a) together with (2.17) in $\int_0^{2\pi} \text{Im}\{Z(\alpha,0)\} \text{Re}\{Z_w(\alpha,0)\} d\alpha = 0$.

At this stage, following [16] for the infinite-depth case, it is useful to replace (II) and (III) by the equivalent conditions

$$\ddot{\alpha}_{p,n} + p\sigma_0 \tanh(p\mu_0)\alpha_{p,n} + S_{p,n} = 0, \quad (S_{p,n} = \dot{T}_{p,n}^3 + pT_{p,n}^4), \quad (\text{II}^*)$$

$$\beta_{p,n} + \dot{\alpha}_{p,n} + T_{p,n}^2 + T_{p,n}^3 = 0. \quad (\text{III}^*)$$

This allows us to solve (II*), (III*) and (IV) sequentially to obtain $\alpha_{p,n}$, $\beta_{p,n}$ and $\gamma_{p,n}$, respectively. Here we have eliminated $\gamma_{p,n}$ from the equations for $\alpha_{p,n}$ and $\beta_{p,n}$, though lower-order terms $\gamma_{p,j}$ with $j < n$ appear in the formulas for the forces $T_{p,n}^3$ and $T_{p,n}^4$.

Our goal in the remainder of this section is to demonstrate the existence of a solution of (I), (II*), (III*), (IV), (i) and (ii) by proposing an algorithm in the spirit of [16]. Let

$$\Omega_{p,n} = \left\{ (q, m) \mid q \geq 1, 0 \leq m \leq n, q + m \leq p + n, (q, m) \neq (p, n) \right\}, \quad (3.6)$$

which are the integer lattice points in the region shown in figure 2. We also define the following sets of functions and real numbers for $n \in \mathbb{N}$:

$$\mathcal{M}_n = \{\mu_0, \mu_1(t), \dots, \mu_n(t)\}, \quad \Sigma_n = \{\sigma_0, \dots, \sigma_n\}. \quad (3.7)$$

Each $\mu_k(t)$ is required to be of the form (3.1), and μ_0 is a given parameter of the problem statement, namely, the fluid depth in physical space after non-dimensionalization.

Similar to the infinite-depth case [16], the forcing terms $T_{0,n}^1$, $T_{p,n}^2$, $T_{p,n}^3$, and $T_{p,n}^4$ are functions of $\alpha_{q,m}$, $\beta_{q,m}$, and $\gamma_{q,m}$ for $(q, m) \in \Omega_{p,n}$. In addition, $T_{0,n}^1$ depends on \mathcal{M}_{n-1} ; $T_{p,n}^3$ and $T_{p,n}^4$ depend on \mathcal{M}_n ; and $T_{p,n}^4$ depends on Σ_n . To say that $\Omega_{p,n}$ is known means that $\alpha_{q,m}$, $\beta_{q,m}$, and $\gamma_{q,m}$ are known for all $(q, m) \in \Omega_{p,n}$. When $n = 0$, we have for $p \geq 2$

$$\Omega_{p,0} = \{(1,0), \dots, (p-1,0)\}. \quad (3.8)$$

For convenience and consistency, we define $\Omega_{0,n} = \Omega_{1,0} = \emptyset$ for $n \geq 0$. In particular, for $(p, n) = (1, 0)$, the forcing terms $T_{1,0}^r$ are zero for $r = 2, 3, 4$. This allows us to immediately solve (II*), (III*), (IV) and (i) to conclude that

$$\begin{aligned} \sigma_0 &= \text{coth}(\mu_0), & \beta_{1,0} &= \text{coth}(\mu_0) \sin(t), \\ \alpha_{1,0} &= \text{coth}(\mu_0) \cos(t), & \gamma_{1,0} &= -\text{coth}(\mu_0) \sin(t). \end{aligned} \quad (3.9)$$

From this point, σ_0 will be considered a known constant of the problem.

3.1 Non-resonant depths and small divisors

Equation (II*) is a second-order, linear, non-homogeneous ODE with constant coefficients, much like the analogous equation (IV*) in [16]. The forcing term $S_{p,n}$ in (II*) will be shown to be an even trigonometric polynomial of the form $\sum_{j \in E_{p+2n}} S_{p,n,j} e^{ijt}$, where E_v was defined above in (3.3) and $S_{p,n,j} = pT_{p,n,j}^4 - jT_{p,n,j}^3$ for $j \in E_{p+2n}$. Thus, (II*) may be written

$$\lambda_{p,j} \alpha_{p,n,j} = -S_{p,n,j}, \quad \lambda_{p,j} = p \frac{\tanh(p\mu_0)}{\tanh \mu_0} - j^2, \quad (j \in E_{p+2n}). \quad (3.10)$$

It has a unique solution of the form (3.2) provided that $\lambda_{p,j} \neq 0$ for $j \in E_{p+2n}$. Here $p \geq 1$, $n \geq 0$, and we can restrict attention to $j \geq 0$ since $\alpha_{p,n,-j} = \alpha_{p,n,j}$. We always have $\lambda_{1,1} = 0$, which is a special case that determines σ_n for $n \geq 1$, as shown in the proof of Lemma 3.2 below. Since $1 < \frac{\tanh(p\mu_0)}{\tanh \mu_0} < p$ for $p \geq 2$ and $\mu_0 \in (0, \infty)$, any solution of $\lambda_{p,j} = 0$ with $p \geq 2$ will satisfy $\sqrt{p} < j < p$. It follows from $j < p$ that if j and p have the same parity, then $j \in E_{p+2n}$ for all $n \geq 0$. Thus, $S_{p,n} = \sum_{l \in E_{p+2n}} S_{p,n,l} e^{ilt}$ contains the term $S_{p,n,j} e^{ijt}$ already when $n = 0$. (This is not true for gravity-capillary waves [18], where $\lambda_{p,j}^{\text{cap}}$ in (1.1) can be zero with $j > p$.) The Stokes expansion ansatz (2.15) is expected to break down at resonant depths since it would be surprising if a cancellation caused $S_{p,0,j} = 0$ to occur at exactly the same depth that led to $\lambda_{p,j} = 0$.

In the infinite depth case with zero surface tension, $\lambda_{p,j} = p - j^2$ is zero whenever $p \geq 2$ is a perfect square and $j = \sqrt{p}$. Nevertheless, imposing compatibility conditions leads to existence and uniqueness of a formal expansion solution. This is a key point and challenge in the work of [16]. In the finite-depth case, Concus [11] proved that for any real interval (a, b) with $0 < a < b < \infty$, there exists a $\mu_0 \in (a, b)$ and integers $p \geq 2$, $j \geq 1$ such that $\lambda_{p,j}$ in (3.10) is zero. His proof is easily adapted to produce j and p of the same parity. It follows that the resulting resonant depths are dense in the positive real numbers. They are enumerated by $p \geq 5$ and $\sqrt{p} < j < p$ with $p - j$ even since $\tanh(p\mu_0) / \tanh \mu_0$ decreases monotonically from p to 1 as a function of $\mu_0 \in (0, \infty)$. Tables containing the first several resonant depths with this enumeration are given in [14].

The complement of this countable dense set of resonant depths has full Lebesgue measure, and consists of depths μ_0 for which the recursive algorithm described below will not lead to a division by zero at any order. For these non-resonant depths, it is desirable to know how small the $\lambda_{p,j}$ may become and what effect such small divisors have on the recursive solution. Let us define

$$\lambda_p = \min_{j \in p+2\mathbb{Z}} |\lambda_{p,j}|. \quad (3.11)$$

When necessary for clarity, we will write $\lambda_p(\mu_0)$ and $\lambda_{p,j}(\mu_0)$. The next lemma and theorem show that all rational depths are non-resonant, and almost every depth μ_0 leads to a sequence $\{\lambda_p(\mu_0)\}_{p=2}^{\infty}$ that is bounded below by a slowly decaying function of p .

Lemma 3.1 *Let μ_0 be a positive algebraic number and let $p \geq 2$ be an integer. Then $p \frac{\tanh(p\mu_0)}{\tanh \mu_0}$ is transcendental and $\lambda_{p,j}$ in (3.10) is nonzero for all integers j .*

Proof Suppose μ_0 and p satisfy the hypotheses and that $r = p \frac{\tanh(p\mu_0)}{\tanh \mu_0} = p \frac{e^{2\mu_0} + 1}{e^{2\mu_0} - 1} \frac{e^{2p\mu_0} - 1}{e^{2p\mu_0} + 1}$ is an algebraic number. After rearranging, we obtain

$$(r - p)e^{2(p+1)\mu_0} - (r + p)e^{2p\mu_0} + (r + p)e^{2\mu_0} + (p - r)e^0 = 0.$$

All four exponents are distinct algebraic numbers. By the Lindemann-Weierstrass theorem [41], the coefficients of the exponentials are zero, implying that $p = r = -r$, a contradiction to $p \geq 2$. So r is transcendental and there is no integer j satisfying $r = j^2$.

Theorem 3.1 *For each $\delta > 0$, the set*

$$\mathcal{E}_\delta = \left\{ \mu_0 > 0 \mid \exists a > 0 \text{ such that } \forall p \geq 2, \lambda_p(\mu_0) \geq \min(a, p^{-\frac{1}{2}-\delta}) \right\} \quad (3.12)$$

has full Lebesgue measure. If $\delta > \frac{1}{2}$ and $\mu_0 > 0$ is rational, then $\mu_0 \in \mathcal{E}_\delta$. For $\delta \leq 0$, \mathcal{E}_δ has Lebesgue measure 0. For $\delta \leq -\frac{1}{2}$, \mathcal{E}_δ is the empty set.

We prove this theorem in the electronic supplementary material and outline the key steps of the proof here. The first assertion makes precise the claim that for almost every fluid depth, $\min_{2 \leq q \leq p} \lambda_q$ is positive for $p \geq 2$ and does not decay to zero much faster than $1/\sqrt{p}$ as $p \rightarrow \infty$. To prove it, we show that $\mu_0 \notin \mathcal{E}_\delta \Rightarrow \tanh \mu_0 \in \mathcal{F}_\delta$, where

$$\mathcal{F}_\delta = \left\{ x \in \mathbb{R} \mid \exists \text{ infinitely many pairs } (p, j) \in \mathbb{Z} \times \mathbb{N} \text{ s.t. } \left| x - \frac{p}{j^2} \right| < \frac{1}{j^{3+\delta}} \right\}, \quad (3.13)$$

which has been proved [42] to have Hausdorff dimension $\frac{3}{3+\delta}$ and Lebesgue measure zero. It follows [43] that \mathcal{E}_δ has full Lebesgue measure. We use a theorem of Schmidt [44] to prove that \mathcal{E}_δ has measure zero for $\delta \in (-\frac{1}{2}, 0]$. For the $\delta \leq -\frac{1}{2}$ result, we use Weyl's equidistribution theorem [45] that if x is irrational then $\{j^2 x \mid j \in \mathbb{N}\}$ is equidistributed on $[0, 1]$ modulo 1. Our proof that rational depths belong to \mathcal{E}_δ for $\delta > \frac{1}{2}$ makes use of Lambert's continued fraction [46] for $\tanh \mu_0$ to establish that the irrationality exponent of $\tanh \mu_0$ is 2 via the method of [47]. It may be possible to replace $\delta > \frac{1}{2}$ by $\delta > 0$ for rational depths, but we do not know how to take advantage of p/j^2 appearing with j squared in (3.13). One can estimate values of δ for which a is not too small numerically. For example, $\mu_0 = 1/16$ appears to belong to \mathcal{E}_δ with $\delta = 0.07$ and $a = 0.0155$, based on checking λ_p for $2 \leq p \leq 6.24 \times 10^{22}$. This is shown in the electronic supplementary material, where we also argue that these lower bounds on small divisors are important for the convergence of Padé approximants of the Stokes expansion. There is an asymmetry in which a approaches 0 as μ_0 approaches a fixed resonant depth through the rationals, but a is positive for a fixed rational depth μ_0 , even though there are sequences of resonant depths approaching μ_0 .

3.2 Recursive algorithm

In this section we assume μ_0 is not a resonant depth. For every integer $\nu \geq 1$, we define a set of lattice points

$$L_\nu = \{ (p, n) \mid n \geq 0, p \geq 1, p + 2n \leq \nu \}, \quad (3.14)$$

as well as a corresponding set of ordered triples

$$\Gamma_\nu = \{ (\alpha_{p,n}, \beta_{p,n}, \gamma_{p,n}) \mid (p, n) \in L_\nu \}, \quad (3.15)$$

where $\alpha_{p,n}$, $\beta_{p,n}$ and $\gamma_{p,n}$ are assumed to be of the form (3.2), (3.4) and (3.5), respectively. We now state an induction hypothesis, \mathcal{P}_ν , for $\nu \geq 1$. The proof establishes the validity of the algorithm, and thus the existence and uniqueness of a solution of (I), (II*), (III*), (IV), (i) and (ii).

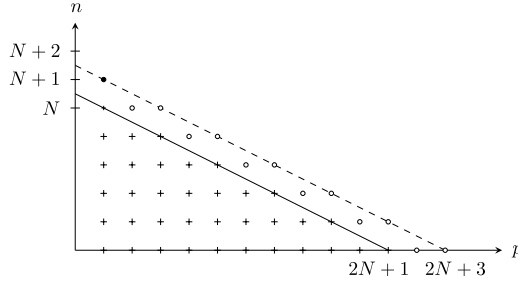


Fig. 3 Points marked with + represent Γ_{2N+1} while points marked with \circ and \bullet extend Γ_{2N+1} to Γ_{2N+3} . On each iteration, we use (II*), (III*) and (IV) to compute $\alpha_{p,n}$, $\beta_{p,n}$ and $\gamma_{p,n}$ at the points marked by \circ in two batches, first those in L_{2N+2}° , followed by those in L_{2N+3}° . The latter points lie on the dashed line. Next we compute μ_{N+1} using (I) and (ii). Finally, we reach \bullet , where we compute σ_{N+1} using the orthogonality condition (3.16), followed by $\alpha_{1,N+1}$, $\beta_{1,N+1}$, and $\gamma_{1,N+1}$ via (II*) and (i), (III*), and (IV), respectively.

\mathcal{P}_v (induction hypothesis): with $N = \lfloor (v-1)/2 \rfloor$, there exist unique Stokes expansion coefficients Γ_v , \mathcal{M}_N , and Σ_N satisfying (II*), (III*) and (IV) for $(p, n) \in L_v$; satisfying (I) and (i) for $0 \leq n \leq N$; satisfying (ii) for $1 \leq n \leq N$; and satisfying

$$\int_0^{2\pi} \cos(t) S_{1,n}(t) dt = 0, \quad (0 \leq n \leq N). \quad (3.16)$$

$S_{p,n}$ is the forcing term in (II*), so the orthogonality condition (3.16) ensures solvability of (II*) at $p = 1$ by eliminating secular terms in the solution that destroy time-periodicity. It is also the constraint needed to uniquely determine the σ_n values. We will prove \mathcal{P}_v inductively and exhibit the algorithm through the proof. The computational scheme is illustrated in figure 3.

Theorem 3.2 \mathcal{P}_v holds for all $v \in \mathbb{N}$.

Proof We have already established in (3.9) that \mathcal{P}_1 holds. Thus, it follows from Lemma 3.2 below that \mathcal{P}_v holds for all $v \geq 1$.

Lemma 3.2 If $N \geq 0$ and \mathcal{P}_{2N+1} holds, then \mathcal{P}_{2N+2} and \mathcal{P}_{2N+3} also hold, and the extensions (in the set-theoretic sense) of Γ_{2N+1} , \mathcal{M}_N , and Σ_N to Γ_{2N+3} , \mathcal{M}_{N+1} , and Σ_{N+1} , respectively, are unique.

Proof We assume \mathcal{P}_{2N+1} holds and Γ_{2N+1} , \mathcal{M}_N , and Σ_N are known. We begin by extending Γ_{2N+1} to Γ_{2N+2} , i.e., to the open circles of figure 3 that do not lie on the dashed line. We denote these lattice points by L_{2N+2}° , where

$$L_v^\circ = \{ (p, n) \mid n \geq 0, p \geq 2, p + 2n = v \}. \quad (3.17)$$

For each $(p, n) \in L_{2N+2}^\circ$, $\Omega_{p,n}$ is a subset of L_{2N+1} , so by the induction hypothesis, each $\alpha_{q,m}$, $\beta_{q,m}$ and $\gamma_{q,m}$ with $(q, m) \in \Omega_{p,n}$ is known and has the form (3.2), (3.4) or (3.5) with p replaced by q and n replaced by m . Since $\mu_n(t)$ has the form (3.1) for $1 \leq n \leq N$, it follows from the recurrence (2.26) that $B_{q,m}(t)$ in (2.24) has the form

$$B_{q,m}(t) = \sum_{j=0}^{2m} B_{q,m,j} H_j \left(e^{ijt} + e^{-ijt} \right), \quad (0 \leq m \leq N, q \in \mathbb{Z}), \quad (3.18)$$

where the $B_{q,m,j}$ are real coefficients and, as before, a prime on a sum indicates that indices of opposite parity to the upper limit should be excluded. The case $q = 0$ is trivial since $\exp(0h) = 1$ in (2.24). As a result, $B_{0,m}(t)$ still has the form (3.18), but all the coefficients $B_{0,m,j}$ are zero except for $B_{0,0,0} = 1$. From (2.25), we then also have

$$c_{q,m}(t) = \sum_{j=0}^{2m} c_{q,m,j} H_j \left(e^{ijt} + e^{-ijt} \right), \quad s_{q,m}(t) = \sum_{j=0}^{2m} s_{q,m,j} H_j \left(e^{ijt} + e^{-ijt} \right) \quad (3.19)$$

for $0 \leq m \leq N$ and $q \in \mathbb{Z}$, where $c_{q,m,j}$ and $s_{q,m,j}$ are real. The coefficients $c_{q,m,j}$ and $s_{q,m,j}$ that arise in the forcing terms $T_{p,n}^r$ with $(p,n) \in L_{2N+3} \setminus L_{2N+1}$ satisfy $|q| \leq 2N+3$.

From the definitions (S4.2), (S4.6) and (S4.8) of the forces, still assuming $(p,n) \in L_{2N+2}^\circ$, we see that $T_{p,n}^2$ and $T_{p,n}^3$ are odd trigonometric polynomials of the form (3.4) while $T_{p,n}^4$ and $S_{p,n}$ are even trigonometric polynomials of the form (3.2). For example, one of the terms that appears in $T_{p,n}^3$ is a multiple of $\alpha_{p-j,k} \alpha_{j,l} \dot{\mu}_m c_{p-2j,n-k-l-m}$, which is a trigonometric polynomial of degree

$$[(p-j) + 2k] + (j + 2l) + (2m) + (2n - 2k - 2l - 2m) = p + 2n. \quad (3.20)$$

It is an odd function as $\dot{\mu}_m(t)$ is odd while the other factors are even. And it includes only terms e^{ijt} with j of the same parity as $p + 2n$. Indeed, each factor (indexed by q) has the form $e^{iv_q t} P_q(e^{-2it})$ where P_q is a polynomial of degree v_q , so the product is also of this form. Since μ_0 is not a resonant depth, we may solve (II*) uniquely to obtain $\alpha_{p,n}$ of the form (3.2), then (III*) uniquely to obtain $\beta_{p,n}$ of the form (3.4), and finally (IV) uniquely to obtain $\gamma_{p,n}$ of the form (3.5). This establishes \mathcal{P}_{2N+2} . Given \mathcal{P}_{2N+2} , identical arguments show that (II*), (III*) and (IV) uniquely determine $\alpha_{p,n}(t)$, $\beta_{p,n}(t)$ and $\gamma_{p,n}(t)$ of the form (3.2), (3.4) and (3.5), respectively, at the lattice points in L_{2N+3}° , which are the \circ markers on the dashed line in figure 3.

The next step is to compute $T_{0,N+1}^1$, which, by (S4.3) and the above reasoning, is an odd trigonometric polynomial of degree $2(N+1)$ that omits terms e^{ijt} with j odd. We then solve (I) and (ii) uniquely for μ_{N+1} of the form (3.1). We also learn that (3.18) and (3.19) hold for $m = N+1$ in addition to the cases $m \leq N$ established above. This fact is needed for the last lattice point $(p,n) = (1, N+1)$ to conclude that $T_{1,N+1}^3(t)$ and $T_{1,N+1}^4(t)$ are, respectively, odd and even trigonometric polynomials of degree $2N+3$ that omit terms e^{ijt} with j even. The analogous conclusion for $T_{1,N+1}^2(t)$ follows directly from \mathcal{P}_{2N+2} since μ_m , $c_{q,m}$ and $s_{q,m}$ do not appear in (S4.1). At this point, all terms in $S_{1,N+1}$ in (II*) are known except σ_{N+1} , which is determined using the orthogonality condition

$$\int_0^{2\pi} \cos(t) S_{1,N+1}(t) dt = 0. \quad (3.21)$$

The term in $S_{1,N+1}$ that contains σ_{N+1} is $\frac{1}{c_{1,0}} \alpha_{1,0} \sigma_{N+1} s_{1,0} = \sigma_{N+1} \cos(t)$, so (3.21) is a linear equation in σ_{N+1} whose coefficient is not zero. This eliminates secular growth in the solution of (II*) for the lattice point $(1, N+1)$ and uniquely determines $\alpha_{1,N+1}$ of the form (3.2), up to an arbitrary real multiple of $\cos(t)$. To determine this unknown coefficient, we compute $\alpha_{1,N+1}(0)$ from (i), where all other quantities are known. Finally, we use (III*) and (IV) to compute $\beta_{1,N+1}$ and $\gamma_{1,N+1}$ of the forms (3.4) and (3.5), respectively.

We have shown that the necessary extensions exist, are unique, and preserve the trigonometric polynomial structure of the induction hypothesis, thus proving the lemma.

4 Numerical results

We computed the expansion coefficients $\alpha_{p,n,j}$, $\beta_{p,n,j}$, $\gamma_{p,n,j}$, $\mu_{n,j}$ and σ_n for dimensionless fluid depths

$$\mu_0 \in \left\{ \frac{1}{16}, \frac{1}{4}, \frac{3}{5}, 1, 4, 10, 16, \infty \right\} \quad (4.1)$$

up to order $\nu = p + 2n = 109$, and then again to $\nu = 149$ for $\mu_0 \in \{3/5, 1, \infty\}$ to further explore the convergence of the Padé approximants studied in section 4.3 below. In infinite depth, we implemented a variant of the Schwartz and Whitney algorithm [15] that will be explained in detail elsewhere [18] as a special case of standing gravity-capillary waves in infinite depth. Our code employs the MPFR multiple precision library [48] with a fixed mantissa size. We implemented it on a supercomputer using a hybrid MPI/OpenMP parallel framework [49]. We ran each calculation at least twice, with different precisions, to observe how floating-point errors accumulate, estimate these errors, and repeat with more precision if necessary. The precisions used were 212 bits (64 digits), 300 bits (90 digits), 480 bits (144 digits), 638 bits (192 digits), and 850 bits (256 digits). Computational aspects and implementation details of the algorithm are given in the electronic supplementary material along with a discussion of the generation, propagation and estimation of floating-point errors.

4.1 Growth of the coefficients in the asymptotic expansion

It is useful to consolidate the ϵ -expansions of $a_p(t)$ and $h(t)$ in the formula (2.13a) for $Z(w, t)$. This gives a single ϵ -expansion of the non-dimensionalized wave profile, which we denote by

$$\tilde{\eta}(\alpha, t) = \frac{2\pi}{L} \eta\left(\alpha, \frac{T}{2\pi} t\right) = \text{Im} \{Z(\alpha, t)\} = \sum_{\nu=1}^{\infty} \tilde{\eta}^{(\nu)}(\alpha, t) \epsilon^{\nu}. \quad (4.2)$$

As in (2.10), the dimensionless variables (α, t) range over the torus \mathbb{T}^2 rather than over a domain that depends on ϵ . We denote the Fourier representation of $\tilde{\eta}^{(\nu)}(\alpha, t)$ by

$$\tilde{\eta}^{(\nu)}(\alpha, t) = \sum_{p,j \in E_{\nu}} \tilde{\alpha}_{p,j}^{(\nu)} e^{ip\alpha} e^{ijt}, \quad (4.3)$$

where E_{ν} was defined in (3.3). We also introduce the area-weighted L^2 -norm

$$A_{\nu} = \left(\frac{1}{(2\pi)^2} \int_0^{2\pi} \int_0^{2\pi} [\tilde{\eta}^{(\nu)}(\alpha, t)]^2 d\alpha dt \right)^{1/2} = \sqrt{\sum_{j,p \in E_{\nu}} |\tilde{\alpha}_{p,j}^{(\nu)}|^2} \quad (4.4)$$

to measure the growth of successive terms in (4.2). Using (2.15), (3.1) and (3.2), it follows from

$$\text{Im} \{Z(\alpha, t)\} = h(t) - \mu_0 + \sum_{p=1}^{\infty} a_p(t) \frac{\sinh(ph(t))}{\cosh(p\mu_0)} \cos(p\alpha) \quad (4.5)$$

that $\tilde{\alpha}_{0,j}^{(2n)} = \mu_{n,|j|}$ for $n \geq 1, j \in E_{2n}$; that $\tilde{\alpha}_{p,j}^{(\nu)} = \tilde{\alpha}_{|p|,|j|}^{(\nu)}$ for $p, j \in E_{\nu}$; and that

$$\sum_{j \in E_{p+2n}} \tilde{\alpha}_{p,j}^{(p+2n)} e^{ijt} = \sum_{m=0}^n \frac{\alpha_{p,m}(t) s_{p,n-m}(t)}{2 \cosh(p\mu_0)}, \quad p \geq 1, n \geq 0. \quad (4.6)$$

We compute the right-hand side in real space on a uniform grid in the t variable with enough gridpoints to avoid aliasing errors. The coefficients $\tilde{\alpha}_{p,j}^{(p+2n)}$ are then easily obtained using the Fast Fourier Transform (FFT) [50, 51]. In the infinite-depth case, the formula is simpler: $\tilde{\alpha}_{p,j}^{(|p|+2n)} = \frac{1}{2H_{|p|}} \alpha_{|p|,n,j}$, where $\alpha_{p,n,j}$ is still related to $a_p(t)$ via (2.15a) and (3.2) but the ansatz (2.13) is replaced by (2.12a) from [15], i.e., $Z(w, t) = w + i \sum_{p=0}^{\infty} a_p(t) e^{-ipw}$.

Panels (a) and (b) of figure 4 show the growth rate factors $\sqrt{A_\nu/A_{\nu-2}}$ of the norms A_ν for different fluid depths. Plotting $\sqrt{A_\nu/A_{\nu-2}}$ instead of $A_\nu/A_{\nu-1}$ decouples the even and odd orders, which eliminates oscillations that obscure the plots. In the cases we studied, the growth rates approach limiting values separated by occasional “stairstep jumps” from one plateau height to another over a narrow transition region. Notable jumps occur for $\mu_0 \in \{1/4, 3/5, 1\}$ near $\nu \in \{70, 102, 66\}$, respectively. We show a connection between these jumps in growth rate and new small divisors entering the recurrence in the electronic supplementary material. We define the inverse growth rate factor

$$\rho_\nu = \sqrt{A_{\nu-2}/A_\nu}, \quad (\nu \geq 3) \quad (4.7)$$

which serves as an effective radius of convergence for the series up to that point due to the geometric growth of A_ν in the plateau regions. Panel (c) shows the norms $A_\nu \epsilon^\nu$ of successive terms of the series (4.2) for $\mu_0 = 1$ and $\mu_0 = 3/5$ for various choices of the amplitude ϵ . Jumps in the growth rate in panel (b) lead to kinks in the plots of panel (c). Once ρ_ν has dropped below ϵ , successive terms of the series begin to grow (rather than decay) geometrically. This is illustrated with $\epsilon = 0.03$ for $\mu_0 = 3/5$ in panel (c). When $\epsilon = \rho_\nu$ in a plateau region, as in the other two plots in panel (c), successive terms remain nearly constant aside from small oscillations between even and odd orders. If one has computed the Stokes coefficients to order ν_{\max} and ϵ is larger than $\rho_{\nu_{\max}}$, the series should be truncated at or before the last ν for which $\rho_\nu > \epsilon$. Using Padé approximants in section 4.3 below, the additional terms are found to continue to improve the accuracy of the rational approximation without requiring $\rho_\nu > \epsilon$.

Panels (d) and (e) of figure 4 show Domb-Sykes plots [52] of $(x_\nu, y_\nu) = (1/\nu, \rho_\nu^{-1})$ for the two cases where a jump is not observed, $\mu_0 = 1/16$ and $\mu_0 = \infty$. Extrapolating this data to $x = 0$ gives an estimate for ρ^{-1} , where ρ is the radius of convergence of the series. The black curves show low-degree polynomials $q(x)$ that were fit to the data points (x_ν, y_ν) as described in the electronic supplementary material. The dashed lines show $q(0) + q'(0)x$, which is the extrapolated estimate of the leading-order asymptotic behavior as $\nu \rightarrow \infty$ and $x_\nu \rightarrow 0^+$. This predicts a radius of convergence of $\rho = 0.000267885$ for $\mu_0 = 1/16$ and $\rho = 0.301262103$ for $\mu_0 = \infty$. (We report the number of digits that appear justified from the polynomial fit.)

Panel (f) shows what can go wrong in these Domb-Sykes calculations. If the series for $\mu_0 = 1$ had only been computed to $\nu_{\max} = 55$, extrapolation to $x = 0$ would suggest an inverse radius of convergence of $\rho^{-1} = q(0) = 4.71$. But there is a transition region where y_ν stops following the curve $q(x_\nu)$ predicted from $10 \leq \nu \leq 55$ and instead jumps rapidly from $y_{59} = 4.562$ to $y_{73} = 7.172$. It then stabilizes at 7.179299 for $85 \leq \nu \leq 149$. Once a jump occurs, it is more useful to plot ν on the x -axis, as in panels (a,b,c), since the plateau regions after a jump are extremely flat. It is not helpful to fit the data after a jump with anything but a constant function. For example, all 17 digits we recorded for ρ_ν^{-1} remain unchanged for $10 \leq \nu \leq 109$ in the case of $\mu_0 = 16$.

We expect that at every non-resonant finite depth, there will eventually be infinitely many stairstep jumps that cause $\rho = \lim_{\nu \rightarrow \infty} \rho_\nu = 0$. This is consistent with previous

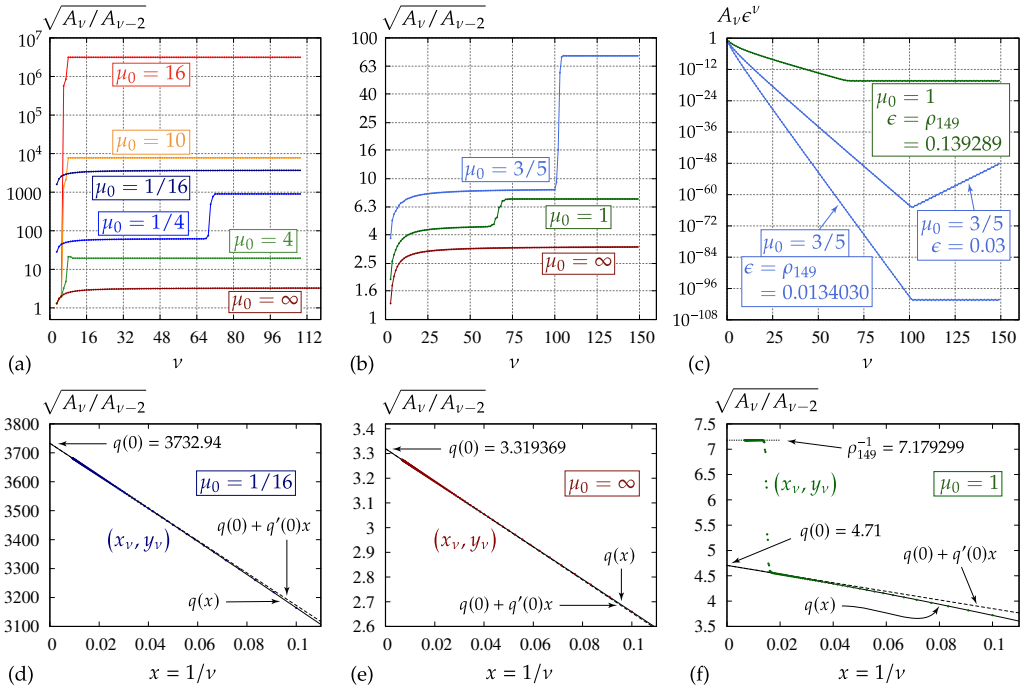


Fig. 4 Growth rate factors $\rho_v^{-1} = \sqrt{A_v/A_{v-2}}$ and norms $A_v \epsilon^v$ of successive terms in the asymptotic expansion. (a,b) Jumps in the growth rate occur for $\mu_0 \in \{1/4, 3/5, 1, 4, 10, 16\}$ when small divisors enter the recurrence and lead to new growth patterns among the coefficients $\tilde{a}_{p,j}^{(v)}$ in (4.4). (c) Optimal truncations of the asymptotic series occur at kinks in the curves where successive terms stop decreasing due the jump in ρ_v^{-1} from panel (b). (d,e) Domb-Sykes plots to estimate the radius of convergence of the series. (f) Such estimates break down after a jump in the growth rate.

studies [24, 13, 14] that concluded that asymptotic expansions of standing waves and short-crested waves have a zero radius of convergence for all depths. However, Theorem 3.1 shows that for almost every fluid depth, the small divisors that lead to the jumps in ρ_v^{-1} arise infrequently as p increases, which limits how fast ρ_v approaches zero. In the case $\mu_0 = 1/16$, which we did not optimize in advance, we find that $\lambda_p \geq \lambda_2 \approx 0.0155$ for $2 \leq p \leq 24773$. So one will not encounter a divisor that is smaller than the first one in practice. There are no bifurcations associated with $|\lambda_{2,2}|$ being small since $(p, j) = (5, 3)$ is the first harmonic resonance in finite depth. As a result, the closest Padé poles to the origin lie on the imaginary axis in this case up to the order we computed ($v = 109$). These results on imaginary Padé poles and a discussion of the importance of ρ_v approaching zero slowly as $v \rightarrow \infty$ for the convergence of the Padé approximants at larger amplitudes are included in the supplementary material and will be investigated further in future work [18, 53].

4.2 Imperfect bifurcations computed using a shooting method

To verify the correctness of the asymptotic expansions and benchmark their accuracy, we compare them quantitatively to standing waves computed via numerical continuation using the overdetermined shooting method of Wilkening and Yu [29]. We focus on the cases $\mu_0 = 3/5$ and $\mu_0 = 1$ as they both possess interesting bifurcation structures associated

with nearby harmonic resonances [26,27]. The depth $\mu_0 = 1/16$ is studied in the electronic supplementary material. Following [31,29], we exploit a symmetry to cut the simulation time down to a quarter period. In the current paper, $t = 0$ corresponds to a maximum-amplitude “rest” state. With this convention, the initial conditions of the shooting method are imposed at $t_0 = -\pi/2$ and the objective function of the shooting method drives the velocity potential to zero at the final time, $t_N = 0$. Here we discretize time into $N \geq 1$ segments $[t_{n-1}, t_n]$ with $-\pi/2 = t_0 < t_1 < \dots < t_N = 0$ and use a uniform grid with I_n timesteps and M_n gridpoints on each segment,

$$\begin{aligned} t_{ni} &= t_{n-1} + i\Delta t_n, & \left(\Delta t_n = \frac{t_n - t_{n-1}}{I_n}, 1 \leq n \leq N, 0 \leq i \leq I_n, 0 \leq m < M_n \right). \end{aligned} \quad (4.8)$$

We use the 8th-order Dormand/Prince Runge-Kutta method [54] for double-precision calculations and a 15th-order spectral deferred correction method [55] for quadruple-precision calculations. The shooting method employs a graph-based formulation of the water wave equations expressed in terms of wave height $\eta^{\text{graph}}(x, t)$ and velocity potential $\phi^{\text{graph}}(x, t)$. In the code, the time variable is $\check{t} = (\frac{1}{4} + \frac{t}{2\pi})T$, which evolves from $\check{t}_0 = 0$ to $\check{t}_N = T/4$, but we will use dimensionless time t here for simplicity. To compute standing waves, we minimize the objective function

$$f(\theta) = \frac{1}{2}r(\theta)^T r(\theta), \quad r_m(\theta) = \frac{1}{\sqrt{M_N}}\phi^{\text{graph}}(x_{Nm}, t_N), \quad \left(\begin{array}{l} 0 \leq m < M_N \\ t_N = 0 \end{array} \right), \quad (4.9)$$

where θ contains the period and initial Fourier modes of the solution up to a given order d ,

$$\theta = \left(T, \{ \hat{\eta}_{2l}^{\text{graph}}(t_0) \}_{l=1}^{\lfloor d/2 \rfloor}, \{ \hat{\phi}_{2l-1}^{\text{graph}}(t_0) \}_{l=1}^{\lfloor d/2 \rfloor} \right), \quad (t_0 = -\pi/2). \quad (4.10)$$

Here $\hat{\eta}_k^{\text{graph}}(t) = \frac{1}{M_n} \sum_{m=0}^{M_n-1} \eta^{\text{graph}}(x_{nm}, t) e^{-ikx_{nm}}$ and $\hat{\phi}_k^{\text{graph}}(t)$ are computed via the FFT from the grid values of the wave profile and surface velocity potential (assuming $t_{n-1} \leq t \leq t_n$). The floor and ceiling functions satisfy $\lfloor d/2 \rfloor + \lceil d/2 \rceil = d$ for all integers $d \geq 1$.

The components of θ in (4.10) are real and all other Fourier modes of the initial condition are set to zero. This imposes the desired symmetry [31,29] that $\eta^{\text{graph}}(x, t_0)$ is an even function of x that remains unchanged if x is shifted by π while $\phi^{\text{graph}}(x, t_0)$ is an even function that changes sign when x is shifted by π . One of the degrees of freedom in (4.10) is specified as an amplitude parameter in the numerical continuation algorithm and is removed from the list of unknowns when minimizing the objective function, so $\theta \in \mathbb{R}^d$. We use $\hat{\phi}_1^{\text{graph}}(t_0)$ as a default; T to line up the periods of labeled solutions such as *ABC* in figure 5; and the most resonant component of θ to navigate turning points in $\hat{\phi}_1^{\text{graph}}(t_0)$, e.g., on bifurcation branches. Alternative amplitude parameters include crest acceleration [31, 26,27,56] and energy [8]. Further details on the boundary integral method used to evolve the water wave equations, our nonlinear least-squares solver, and the variational equations used to compute $J = \nabla_{\theta} r$ are given in [29].

The shooting method results need to be converted to conformal variables in order to compare them to the asymptotic expansions of section 3.2. Focusing on the initial conditions, we use Newton’s method to solve $F[\eta] = 0$, where $\eta(\alpha)$ is shorthand for $\eta(\alpha, t_0)$ and

$$F[\eta](\alpha) = \eta(\alpha) - \eta^{\text{graph}}(\zeta(\alpha), t_0), \quad \zeta(\alpha) = \alpha + H^{h, \text{coth}}[\eta](\alpha). \quad (4.11)$$

Here $H^{h, \text{coth}}$ is the variant of the Hilbert transform with symbol $\hat{H}_k^{h, \text{coth}} = -i \coth(kh)$, and $h = \mu_0 + \frac{1}{2\pi} \int_0^{2\pi} \eta(\alpha) d\alpha$ is the fluid depth in conformal space, which is calculated from

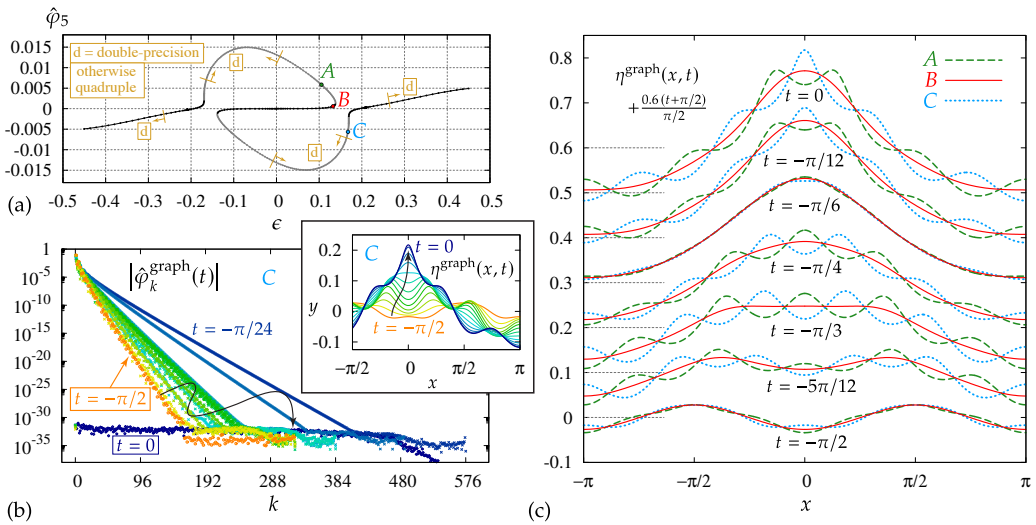


Fig. 5 Standing waves of depth $\mu_0 = 3/5$. (a) The nearby (5,3) harmonic resonance at $\mu_0 = 0.6232354$ leads to an imperfect bifurcation with a large gap separating solution B from solution C. (b) Snapshots of the surface velocity potential (in Fourier space) and the wave profile (inset figure) for $t \in \mathcal{T}_{12}$ for solution C. (c) The wave profile for solutions A, B and C at times $t \in \mathcal{T}_6$. The dashed gray horizontal lines near $x = -\pi$ are vertical offsets added for clarity.

η as a preliminary step in the evaluation of $F[\eta]$. The shooting method places the bottom boundary at $y = -\mu_0$ and ensures that $\int_0^{2\pi} \eta^{\text{graph}}(x, t_0) dx = 0$. Equation (4.11) is imposed at the collocation points $\alpha_j = 2\pi j/M_1$, $0 \leq j < M_1$, with M_1 as in (4.8), and h is computed via the trapezoidal rule at these same points, which preserves the spectral accuracy of the solution. We also compute $\varphi(\alpha, t_0) = \varphi^{\text{graph}}(\zeta(\alpha), t_0)$ to convert the surface velocity potential to conformal variables.

Figure 5 shows the results of the shooting method for $\mu_0 = 3/5$, which is close to the resonant depth $\mu_0 = 0.6232354$ where $\lambda_{53} = 0$. Standing waves near this resonance have been studied before [26, 28, 27], but we have new results to report. After converting the initial conditions from the shooting method to conformal variables, we compute the Fourier expansions

$$\eta(\alpha, t_0) = \sum_{p \in 2\mathbb{Z}} \hat{\eta}_p e^{ip\alpha}, \quad \varphi(\alpha, t_0) = \sum_{p \in 1+2\mathbb{Z}} \hat{\varphi}_p e^{ip\alpha}, \quad (t_0 = -\pi/2) \quad (4.12)$$

numerically via the FFT, up to $|p| \leq M_1/2$. Panel (a) shows a bifurcation plot of $\hat{\phi}_5$ versus the amplitude, $\epsilon = \frac{1}{2}[\eta(0, 0) - \eta(\pi, 0)]$. A spatial shift by π leads to another standing wave with ϵ replaced by $-\epsilon$. At $t = t_0$, this gives $\varphi(\alpha, t_0; -\epsilon) = \varphi(\alpha - \pi, t_0; \epsilon) = -\varphi(\alpha, t_0; \epsilon)$, which explains the odd symmetry of the plot in panel (a). There is an imperfect bifurcation near $\epsilon = 0.15$ that leads to a bubble structure in the bifurcation plot. Okamura observed a similar structure within weakly nonlinear theory near this same resonant depth [28]. Solutions A, B and C demonstrate typical behavior [27] of standing waves near a resonant depth. Panel (c) shows snapshots of these 3 solutions plotted on top of each other at the dimensionless times

$$\mathcal{T}_n = \left\{ \left(\frac{j-n}{n} \right) \left(\frac{\pi}{2} \right) \mid 0 \leq j \leq n \right\}, \quad (4.13)$$

where $n = 6$ in this plot. They were selected to have identical periods, $T = 8.45592$. The non-uniqueness is due to 3 possible amplitudes of a secondary standing wave that evolves on top of the primary wave and has features similar to the nearby harmonic resonance ($p = 5$ spatial cycles and $j = 3$ temporal cycles). For solution C , the secondary wave is in phase with the primary wave, which sharpens the crest at $t = 0$. For solution A , it is out of phase, causing a dimple to form at the wave crest at $t = 0$. Since the secondary wave is not active for solution B , we define the primary wave to be solution B . Solutions A and C appear to oscillate around solution B , though each is its own standing-wave solution of the fully nonlinear water wave equations.

Panel (b) of figure 5 shows the time-evolution of the Fourier modes of the surface velocity potential of solution C in the graph-based formulation of the shooting method. Except in the regions indicated in panel (a), all solutions were computed in quadruple-precision (including solution C). As the solution evolves from $t = -\pi/2$ to $t = 0$, the modes decay exponentially, but the decay rate fluctuates in time following the wavy black arrow in the figure. The modes are also color coded, evolving from orange to yellow to green to blue to navy, matching the inset plot of $\eta^{\text{graph}}(x, t)$. At the final time, $t = 0$, the velocity potential is driven nearly to zero by minimizing $f(\theta)$ in (4.9) to 4.8×10^{-62} so that all the Fourier modes $\hat{\phi}_k^{\text{graph}}(t_N)$ are below 10^{-31} .

Figure 6 shows the shooting method results for the $\mu_0 = 1$ case. There are 3 nearby resonant depths $\mu_0 \in \{1.0397, 0.9730, 0.9962\}$ that lead to a cluster of small divisors $\lambda_{p,j}$ with $(p, j) \in \{(7, 3), (12, 4), (19, 5)\}$; see figure 10 of the electronic supplementary material. Panels (a)–(c) of figure 6 show how the nearly resonant Fourier modes of the initial condition ($\hat{\phi}_7$, $\hat{\eta}_{12}$ and $\hat{\phi}_{19}$) depend on the amplitude ϵ . These plots show different projections of the same set of standing wave solutions and reveal a rich bifurcation structure that has not been reported on before. As with the $\mu_0 = 3/5$ case, when three branches meet at an imperfect pitchfork bifurcation, solutions on the two side branches exhibit higher-frequency, secondary standing waves oscillating with one of two temporal phases on top of the primary wave. Solutions on the center branch remain calm, without exciting this secondary wave. Similar solutions with secondary standing waves have been reported previously in [26, 27, 28, 29, 19, 30]. These secondary waves can deviate visibly from their form in the linear water wave regime. This is demonstrated in figures 14–18 in the electronic supplementary material, which show solutions DEF , HIJ and KLM in figure 6 as well as the secondary wave associated with another bifurcation at $\epsilon = 0.27380806$. Solution G in panels (a,b,c) of figure 6 is the highest wave for $\mu_0 = 1$, which will be discussed further in section 4.3 below. Solution O is the zero-amplitude flat rest state.

The $(7, 3)$ resonance leads to the imperfect bifurcation separating solution F from solution E in panel (a) of figure 6. It became too expensive to maintain double-precision accuracy beyond solution D , but if μ_0 is increased to 1.03, this branch can be continued farther and meets up with the odd reflection (under $\epsilon \rightarrow -\epsilon$) of the branch passing through solution F ; see [29]. Solutions E and F were chosen to match the period, $T = 7.26730$, of solution D . Panels (d)–(f) show solutions DEF at dimensionless times $t \in \mathcal{T}_{12}$ from (4.13). At $t = 0$, the secondary standing wave causes a dimple to form at the crest of solution D and sharpens the crest of solution F . The $(12, 4)$ resonance leads to two imperfect bifurcations on either side of solution I in panel (b) while the $(19, 5)$ resonance leads to the side branches passing through solutions K and M in panel (c). The value of ρ_ν for $81 \leq \nu \leq 149$ in figure 4 is 0.139289, and coincides with the amplitude ϵ where the imperfect bifurcation to the K and M side branches occurs. These side branches (gray markers) show no sign of reconnecting with the main branch (black markers), so we stopped when the calculations became expensive. We will refer to the connected components of the main branch as the

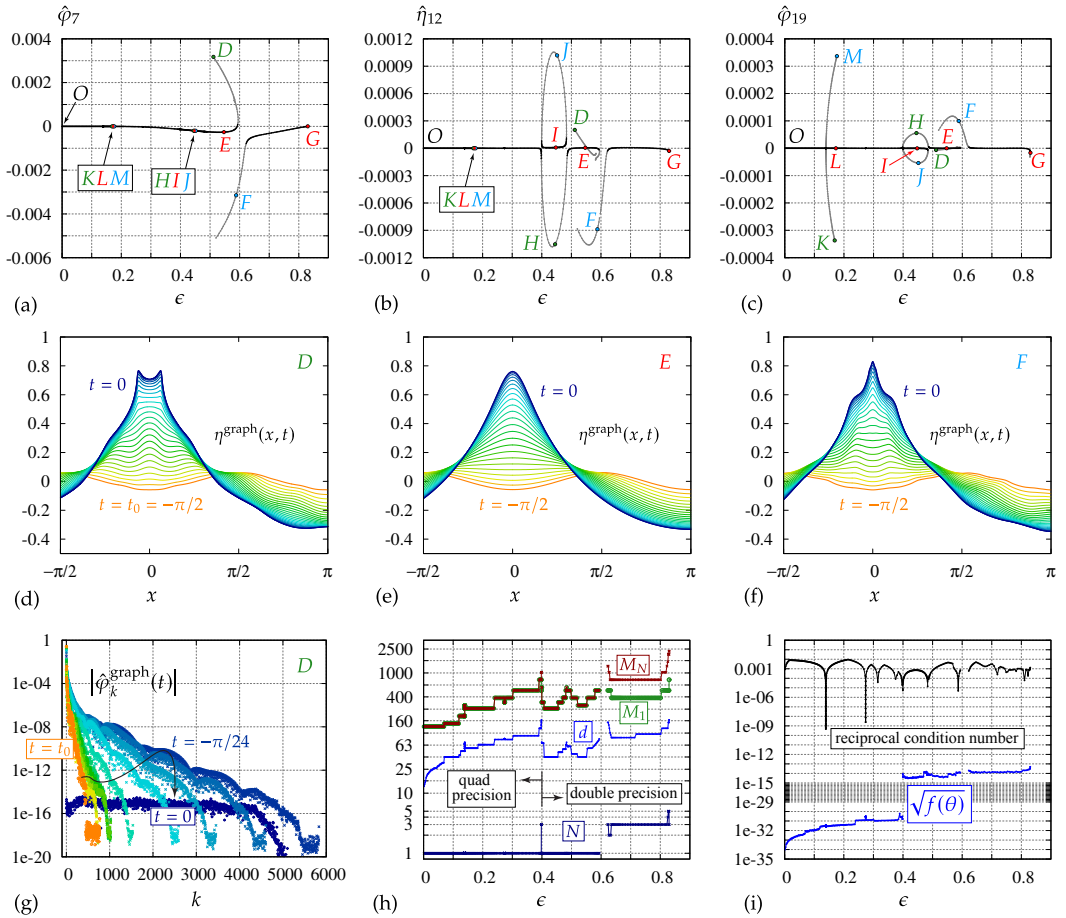


Fig. 6 Standing waves of depth $\mu_0 = 1$. (a,b,c) Bifurcation plots of $\hat{\phi}_7$, $\hat{\eta}_{12}$ and $\hat{\phi}_{19}$ versus ϵ reveal numerous imperfect bifurcations. (d,e,f) Wave profile evolution for solutions DEF at dimensionless times $t \in \mathcal{T}_{24}$. (g) Fourier mode evolution of $\hat{\phi}_k^{\text{graph}}(t)$ for solution D at times $t \in \mathcal{T}_{24}$. (h) Parameters d , N , M_1 and M_N of the shooting method for the solutions corresponding to the black markers in panels (a,b,c). (i) Condition number and minimized value of $\sqrt{f(\theta)}$.

center branches. To stay on the main branch at an imperfect bifurcation, one has to jump from one center branch to the next.

The shooting method parameters of these main branch solutions are plotted in panel (h) of figure 6. The side branch solutions are omitted to make the plot single-valued. We switched from quadruple-precision to double-precision at $\epsilon = 0.4$ due to the high cost of carrying out the shooting method with larger grid sizes. We also used adaptive grids with $N \geq 2$ in (4.8) for the larger problem sizes in double and quadruple-precision. The Fourier mode evolution of solution D , which has the most “active” Fourier modes among the solutions we computed, is shown in panel (g). There are only 450 modes of magnitude larger than 10^{-14} at $t = t_0 = -\pi/2$, whereas there are close to 5000 at $t = 0$. By evolving from $t = -\pi/2$ to 0 instead of 0 to $\pi/2$, as was previously done for standing waves [26], we reduced the dimension d of θ in (4.10) by a factor of 11. By increasing the grid size adaptively from $M_1 = 1536$ to $M_7 = 11664$ in this case, 60% of the cost goes into evolving the solution

and its first variation with respect to θ (a matrix with $d = 450$ columns) through the last 17% of the simulation time. Panel (i) shows the square root of the minimized value of $f(\theta)$ for each solution on the main branch. We minimize $f(\theta)$ until floating-point error prevents further reduction. In all cases, $\sqrt{f(\theta)}$ was reduced below 10^{-30} in quadruple-precision and below 7×10^{-14} in double-precision.

Also plotted in panel (i) of figure 6 is the reciprocal of the condition number of the Jacobian in the shooting method on the final iteration of each Levenberg-Marquardt minimization. Each downward spike corresponds to an approximate resonance of the nonlinear problem, where there are solutions of the linearization about the standing wave that behave like secondary standing waves. At a perfect bifurcation, the Jacobian is singular [57], and near an imperfect bifurcation, the Jacobian is nearly singular. In the electronic supplementary material, we show how to use the right singular vector corresponding to the smallest singular value of the Jacobian to identify which harmonic resonance will be activated by following an imperfect bifurcation, and to observe how strongly the wave profile of the associated secondary wave is distorted away from being a multiple of $\cos(px) \cos(jt)$ due to nonlinear interactions with the primary wave and itself.

4.3 Padé approximation

Next we compare the unit-depth shooting method results for T and $\hat{\phi}_{19}$ to Padé approximants of their Stokes expansions. Setting $g = 1$ and $L = 2\pi$ in (2.10) gives

$$T = 2\pi\sqrt{S} = \sum_{n=0}^{\infty} \tau_n \epsilon^{2n} = \frac{1}{\epsilon^2} \mathcal{K} \frac{d_n \epsilon^2}{1} = \frac{d_0}{1} + \frac{d_1 \epsilon^2}{1} + \frac{d_2 \epsilon^2}{1} + \dots, \quad (4.14)$$

where for any $N \geq 0$, τ_0, \dots, τ_N are uniquely determined from $\sigma_0, \dots, \sigma_N$ in (2.15b) by matching terms in $(\sqrt{S})(\sqrt{S}) = S$, and d_0, \dots, d_N are uniquely determined from τ_0, \dots, τ_N by the quotient-difference (qd) algorithm for continued fractions [58, 46]. The equal signs are intended in the sense of formal power series [58]. Let $\tilde{\tau}_{p,n}$ and $\tilde{d}_{p,n}$ denote the coefficients of the expansions

$$\begin{cases} \hat{\eta}_p, & p \text{ even} \\ \hat{\phi}_p, & p \text{ odd} \end{cases} = \sum_{n=0}^{\infty} \tilde{\tau}_{p,n} \epsilon^{p+2n} = \frac{\epsilon^p}{\epsilon^2} \mathcal{K} \frac{\tilde{d}_{p,n} \epsilon^2}{1}, \quad (p \geq 0). \quad (4.15)$$

We compute the $\tilde{\tau}_{p,n}$ from $\eta(\alpha, t_0) = \text{Im}\{Z(\alpha, t_0)\}$ and $\varphi(\alpha, t_0) = \sqrt{\frac{L^3 g}{8\pi^3 S}} \text{Re}\{F(\alpha, t_0)\}$ as follows. Setting $g = 1$ and $L = 2\pi$ to match the parameters used in the shooting method, we use (4.5) and the analogous equation for $\text{Re}\{F(\alpha, t_0)\}$ to obtain $\hat{\eta}_0 = [h(t_0) - \mu_0]$ and

$$\hat{\eta}_p = a_p(t_0) \frac{\sinh(ph(t_0))}{2 \cosh(p\mu_0)}, \quad \left(\begin{array}{l} p \geq 2 \\ p \text{ even} \end{array} \right), \quad \sqrt{S} \hat{\phi}_p = c_p(t_0) \frac{\cosh(ph(t_0))}{2 \cosh(p\mu_0)}, \quad \left(\begin{array}{l} p \geq 1 \\ p \text{ odd} \end{array} \right). \quad (4.16)$$

The ϵ^{p+2n} term of $a_p(t_0) \sinh(ph(t_0))$ is $\sum_{m=0}^n \alpha_{p,m}(t_0) s_{p,n-m}(t_0)$, with a similar formula for $c_p(t_0) \cosh(ph(t_0))$. Since the expansion of \sqrt{S} is known from (4.14), solving $\sqrt{S} \hat{\phi}_p = \dots$ for $\hat{\phi}_p$ is also a simple matter of matching terms order by order.

In our 638-bit calculation for $\mu_0 = 1$, we reached order $\nu = 149$ in (3.15). This allows us to compute τ_n and d_n for $0 \leq n \leq 74$ and $\tilde{\tau}_{19,n}$ and $\tilde{d}_{19,n}$ for $0 \leq n \leq (\nu - 19)/2 = 65$ via the qd-algorithm [58]. Truncating the continued fraction at d_{74} or $\tilde{d}_{19,65}$ gives the $[37/37]_{\tau}(\epsilon^2)$ or $\epsilon^{19}[32/33]_{\tilde{\tau}_{19}}(\epsilon^2)$ Padé approximant of T or $\hat{\phi}_{19}$, respectively [46, 58, 59].

Here, with $x = \epsilon^2$, we define $[m/d]_{\tilde{\tau}_{19}}(x) = P(x)/Q(x)$ with P of degree m , Q of degree d , $Q(0) = 1$, and $P(x) - Q(x) \sum_{n=0}^{m+d} \tilde{\tau}_{19,n} x^n = O(x^{m+d+1})$, with a similar definition for $[m/d]_{\tau}(x)$. We monitored the floating-point arithmetic errors as explained in the electronic supplementary material.

Panel (a) of figure 7 shows the period T of the unit-depth standing wave solutions of figure 5. The blue curve shows $[37/37]_{\tau}(\epsilon^2) = P(\epsilon^2)/Q(\epsilon^2)$, which is a 149th-order approximation of T since the first incorrect term of its Taylor series is $O(\epsilon^{150})$. This Padé approximation has pole singularities at values of ϵ where $Q(\epsilon^2) = 0$. This causes the blue curve to approach $\pm\infty$ as ϵ approaches each pole. In panel (b), we quantify the agreement between the shooting method solutions and the Stokes and Padé expansions of various orders. As in figure 6, the shooting method solutions have been grouped into main and side branches, plotted with black and gray markers, respectively. For each solution on the main branch, we compute its crest to trough height ϵ and use that for the amplitude of the Stokes and Padé expansions. We use the shooting method solution for the “exact” solution T when computing the relative error $|\Delta T|/T$ in the plot, where

$$\Delta T = T^{\text{expansion}} - T^{\text{shooting}}, \quad \Delta \hat{\phi}_p = \hat{\phi}_p^{\text{expansion}} - \hat{\phi}_p^{\text{shooting}}. \quad (4.17)$$

In many cases, ΔT and $\Delta \hat{\phi}_p$ are dominated by the error in the shooting method since more precision was used in the Padé and Stokes expansions. The dashed lines in panel (b) are the Stokes expansions $\sum_{n=0}^{(v-1)/2} \tau_n \epsilon^{2n}$ of orders $v \in \{69, 109, 149\}$ while the solid lines are the Padé expansions $[m/d]_{\tau}(\epsilon^2)$ with $m = \lfloor (v-1)/4 \rfloor$ and $d = \lceil (v-1)/4 \rceil$ for $v \in \{35, 49, 69, 109, 149\}$. In each case, the order of the approximation is $2(m+d)+1 = v$.

The error curves in panel (b) of figure 7 reach a floor of 10^{-32} as that is the accuracy limit of the shooting method in quadruple-precision. The Stokes expansions are extremely accurate up to $\epsilon = 0.1$, but then rapidly lose accuracy as ϵ crosses ρ_v in (4.7), which is 0.139289367 for $v \in \{109, 149\}$ and coincides with the amplitude where the *KLM* bifurcation occurs in figures 6 and 7. For each shooting-method solution on the main branch, ϵ has a fixed value and the Padé approximants continue to improve in accuracy as v increases, even if multiple bifurcations have occurred at smaller values of ϵ . For a given v , the errors in the Padé approximation are largest for large ϵ , and in regions where the main branch transitions into the side branches. In these transition regions, the output values T and ϵ from the shooting method carry the most error due to the large condition numbers observed there in figure 6. This output value of ϵ (the wave height) is then used to compute $T^{\text{expansion}}$ in (4.17) to obtain $|\Delta T|/T$. Even if the Padé approximation gave the exact solution $T(\epsilon)$, errors in ϵ from the shooting method would be amplified most in the transition regions, where $|T'(\epsilon)|$ is large. Since the Padé approximation is not exact, its poles introduce a second source of sensitivity on ϵ . These poles make it possible to more accurately follow the main branch toward the side branches and jump across disconnections in the bifurcation curves, but $T(\epsilon)$ could have branch cuts or other singularities that cannot be perfectly represented by a rational function. Once ϵ approaches a pole too closely, accuracy will be lost.

Panel (a) of figure 8 shows $\hat{\phi}_{19}$ versus ϵ for unit-depth standing waves. The shooting method data is the same as in panel (c) of figure 6, but the y -axis has been scaled by a factor of 20 to better view the imperfect bifurcations connecting the main-branch to the side-branches. The blue and dashed orange curves are the 149th and 139th-order Padé approximants, $\epsilon^{19}[32/33]_{\tilde{\tau}_{19}}(\epsilon^2)$ and $\epsilon^{19}[30/30]_{\tilde{\tau}_{19}}(\epsilon^2)$, respectively. In addition to correctly navigating (in a topological sense) the *KLM* bifurcation and both sides of the *HII* bubble structure, both Padé approximants predict a bifurcation at $\epsilon = 0.273808$. We computed

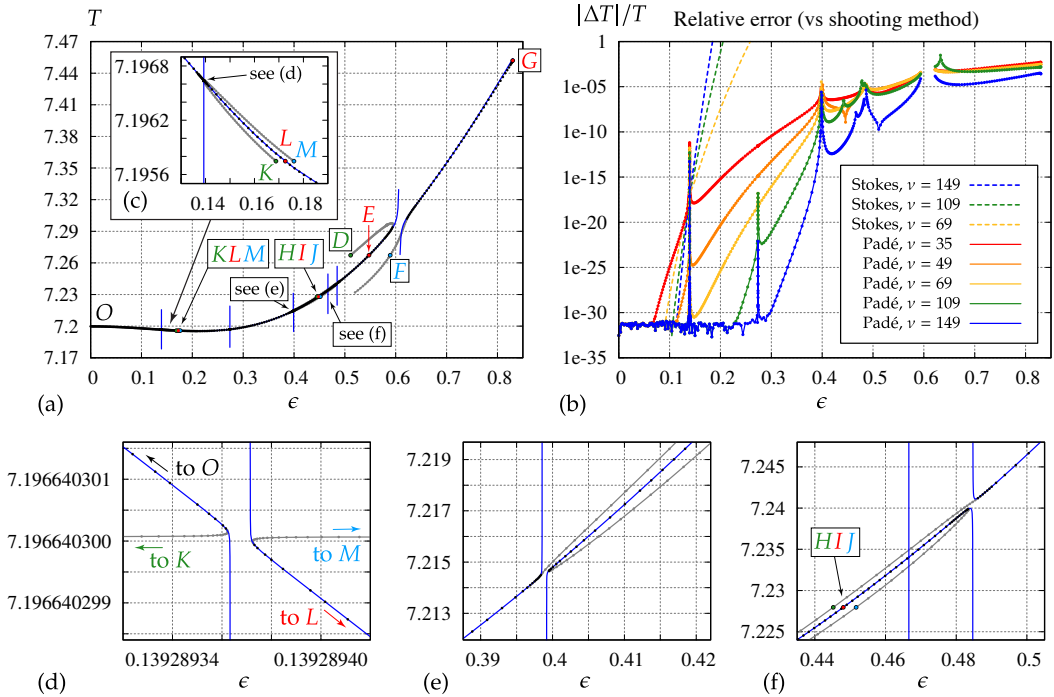


Fig. 7 Dependence of the period T on the amplitude ϵ for standing waves of unit depth. (a) The black and gray markers are the shooting method results for solutions on the main and side branches, respectively. Blue curves are the 149th-order Padé approximation, which has poles where the curves diverge from the main branch. (b) Difference between the shooting method results and the Stokes or Padé expansion solutions at various orders, expressed as a relative error. (c,d,e,f) a closer look at the alignment of Padé poles and imperfect bifurcations. (d) four Padé poles suggest a branch cut.

additional shooting method solutions with ϵ in this neighborhood and find that there is indeed a bifurcation here corresponding to the $(p, j) = (37, 7)$ harmonic resonance. Details on how the resonance was identified are given in the electronic supplementary material. We would not have known to look for a bifurcation here without computing the Padé poles. These additional shooting method results were incorporated into the main branch of solutions before making the plots in figures 6 and 7, which is why there is a spike at $\epsilon = 0.273808$ in the error plot of panel (b) of figure 7.

For $\epsilon > 0.5$ in panel (a) of figure 8, the two Padé approximants we plotted deviate from each other, and have not yet converged on the shooting method results. The 139th-order approximant (orange dashed line) has a pole at $\epsilon = 0.6093$ that helps navigate the start of the DEF bifurcation, but breaks down after that. The shooting method reveals another disconnection in the bifurcation curve on the side branch from E to D , located to the right of the E label in panel (a). Such side-branch bifurcations cannot be seen by the Padé approximants, which are single-valued functions of ϵ that appear to converge to solutions on the main branch. The 149th-order approximant (blue line) has a spurious pole at 0.5040 and doesn't "see" the DEF bifurcation, but does a better job of tracking the final turning point to the highest wave, G . A pole is considered spurious if it doesn't persist across multiple consecutive orders ν of the Padé approximation, or if there is no evidence of an actual bifurcation at this location using the shooting method. The pole in $[37/37]_{\tau}(\epsilon^2)$ at $\epsilon = 0.4666$ in panel (f) of figure 7 also appears to be spurious, and agrees with a zero of

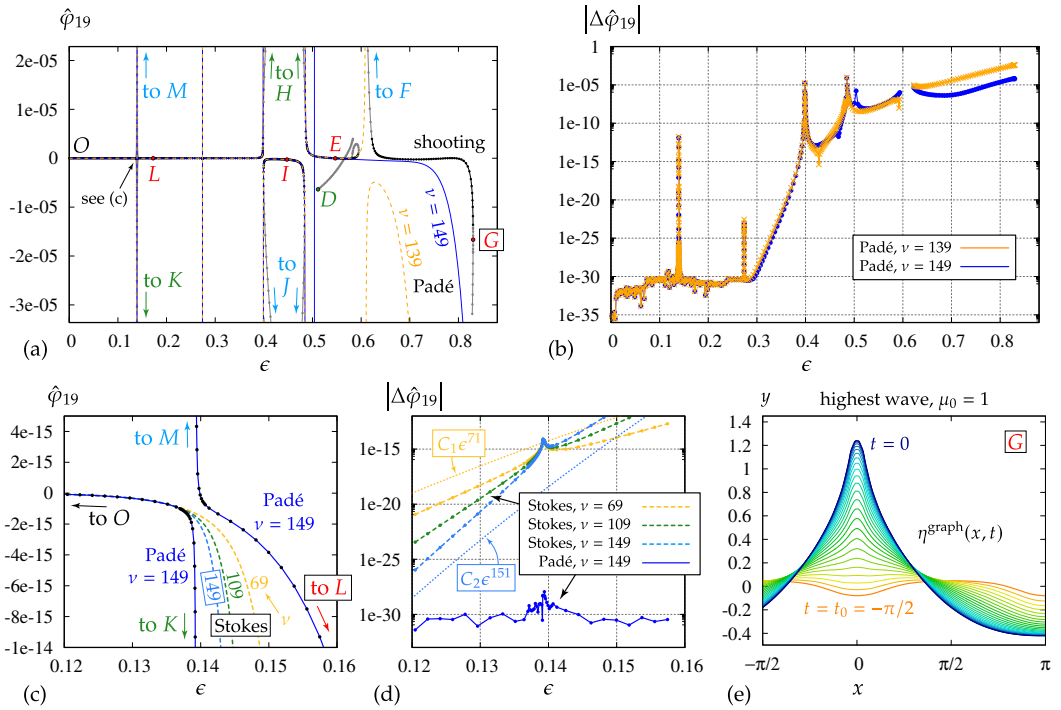


Fig. 8 Unit-depth standing waves exhibit numerous imperfect bifurcations that are visible in plots of $\hat{\phi}_{19}$ versus ϵ . (a) The black and gray markers are the shooting method results. The solid blue curves and dashed orange curves show the 149th and 139th-order Padé approximants. (c) A closer look at the first imperfect bifurcation. The Padé approximant cleanly jumps to the new branch while the Stokes expansions cannot. (b,d) Difference between the shooting method and the Stokes or Padé results in panels (a,c). (e) The highest wave, solution G in figure (a), is not singular.

the numerator to 11 digits. Such pole-zero pairs are called Froissart doublets [59]. Panel (b) of figure 8 shows that both Padé approximants plotted in panel (a) agree with the shooting method to an absolute error of $|\Delta \hat{\phi}_{19}| < 10^{-29}$ for $0 \leq \epsilon \leq 0.3$, except in the transition regions to the side branches near $\epsilon = 0.139289$ and $\epsilon = 0.273808$. We plotted the absolute error since the shooting method involves computing $O(1)$ quantities such as T whereas $\hat{\phi}_{19}$ is $O(\epsilon^{19})$. This causes the shooting method to lose relative accuracy at small amplitude in higher-frequency modes such as $\hat{\phi}_{19}$.

Panels (c) and (d) of figure 8 show that the 149th-order Padé approximant maintains absolute errors below 10^{-28} as it navigates the jump across the disconnection in the bifurcation curve at $\epsilon = 0.139289$. Here we only plot errors at the points shown in panel (c). The errors become larger farther out on these center branches, where they transition to the side branches to K and M. The Stokes expansions cannot change course fast enough to follow the side branch to solution K in panel (c), and cannot jump branches since they are polynomials. Prior to this first imperfect bifurcation, the error in the Stokes expansions converge at the expected order, $O(\epsilon^{\nu+2})$. This is demonstrated in panel (d) for $\nu \in \{69, 149\}$ by comparing the dashed error curves with the dotted lines showing $C_1 \epsilon^{71}$ and $C_2 \epsilon^{151}$. The constants C_i were chosen to position the dotted lines near the corresponding error curves without obscuring the plot.

The existence of a smooth highest wave, solution G , is a new result. Snapshots of its time evolution are given in panel (e) at times $t \in \mathcal{T}_{24}$. We located it using 8th degree polynomial interpolation to represent ϵ as a function of $\hat{\phi}_{19}$. The 9 interpolation points are the 4 gray markers above and below the red marker labeled G in panel (a), plus a gray marker hidden below the red marker. Maximizing the polynomial gave $\hat{\phi}_{19} = -1.665013 \times 10^{-5}$. We used this value in the shooting method to compute solution G , which has the maximum wave height of $\epsilon = 0.83016190$. Marchant and Roberts [14] conjectured that the highest wave would have a curvature singularity that would appear as a pole in its Padé approximation, which they computed to 35th-order to estimate the maximum wave height. Our result shows that this conjecture is incorrect, at least for $\mu_0 = 1$. It has also been shown in the infinite-depth case [56, 29] that standing waves do not form sharp corners at limiting amplitudes and crest acceleration does not monotonically parameterize the solutions. See [29] for details on what happens instead of forming a corner.

4.4 Branch cuts between turning points in the bifurcation curves

Next we investigate how the Padé approximants are able to navigate the disconnections in the bifurcation curves so accurately. The 149th-order Padé approximants of T and $\hat{\phi}_{19}$ both contain 4 closely spaced poles and zeros that lie in the gap between the turning points in ϵ shown in panel (d) of figure 7. From the shooting method, we find that these turning points are located at $\epsilon_L = 0.139289362345$ and $\epsilon_R = 0.139289372366$. The emergence of multiple Padé poles and zeros in the gap between ϵ_L and ϵ_R suggests that each function being approximated, $T(\epsilon)$ and $\hat{\phi}_{19}(\epsilon)$, has a branch cut from ϵ_L to ϵ_R on the real ϵ -axis [33]. Generalizing, it suggests that $a_p(t; \epsilon)$, $b_p(t; \epsilon)$, $c_p(t; \epsilon)$, $S(\epsilon)$ and $h(t; \epsilon)$ in (2.15) each have a branch cut from ϵ_L to ϵ_R . These functions are real-valued for $\epsilon < \epsilon_L$ on the branches to O and to K in panel (d) of figure 7, and for $\epsilon > \epsilon_R$ on the branches to M and to L , which suggests that the branch points at ϵ_L and ϵ_R have square root singularity structures. There are no solutions in the gap between ϵ_L and ϵ_R . Analytic continuation around the branch points into the gap (if it is possible) would lead to water waves with a complex period, a complex fluid depth, etc., which would be difficult to interpret physically. The 149th-order Padé approximants of T and $\hat{\phi}_{19}$ also have two poles in the gap between branches near $\epsilon = 0.399$. Turning points have been observed before [27, 29], but we are not aware of branch cuts being discussed previously in the context of standing water waves.

Further evidence that standing wave families contain branch cuts is given for the $\mu_0 = 3/5$ case in figure 9. The blue curve in panel (a) is the 147th-order Padé approximant $\epsilon^5 [35/36]_{\tilde{\tau}_5}(\epsilon^2)$ of $\hat{\phi}_5$ while the black and gray markers are the shooting method results of figure 5. In panel (b), we see that the error in the Padé approximant of order ν generally decreases as ν increases, but not monotonically. The most accurate approximant with $\nu \leq 149$ over the range $0.25 \leq \epsilon \leq 0.45$ turns out to be of order $\nu = 147$. Panel (c) shows the zeros and poles of $[35/36]_{\tilde{\tau}_5}(\epsilon^2)$ in the complex plane, without the factor of ϵ^5 . These zeros and poles are the square roots of the zeros of $P(x)$ and $Q(x)$ in $[35/36]_{\tilde{\tau}_5}(x) = P(x)/Q(x)$. We compute P and Q by finding the nullspace of a Toeplitz matrix [59] and then use Mathematica to find their zeros. Both of these steps are done in high-precision arithmetic to match the 638-bit precision of the Stokes expansion of $\hat{\phi}_5$ that we computed. The number of zeros and poles that appear in the gap between the turning points $\epsilon_L = 0.13854288$ and $\epsilon_R = 0.16926877$ generally increases with the order ν . We interpret this to mean that $\hat{\phi}_5(\epsilon)$ has a branch cut on the real ϵ -axis from ϵ_L to ϵ_R . Panel (d) shows that for $\nu = 147$, the Padé approximant has 11 poles and 10 zeros on this branch cut. This is consistent with the

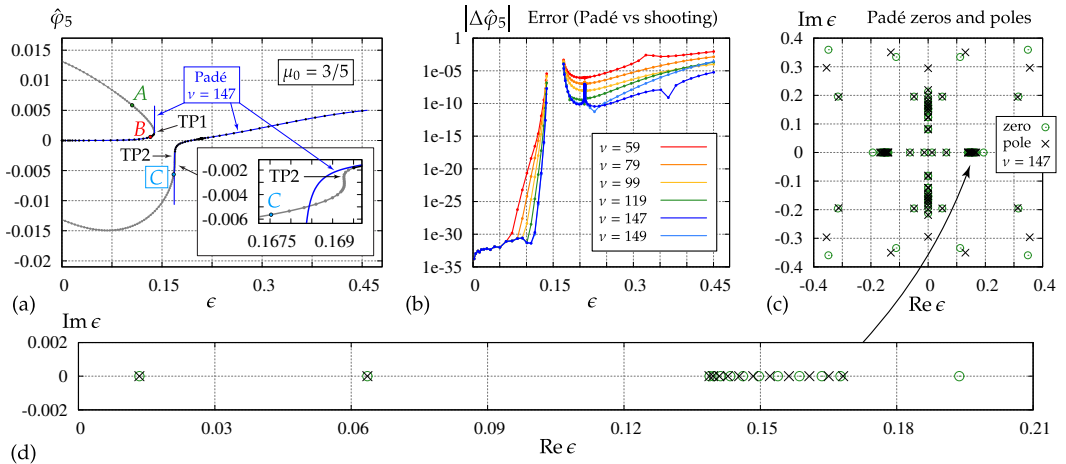


Fig. 9 Evidence of a branch cut between the turning points labeled TP1 and TP2 in panel (a) for $\mu_0 = 3/5$, and accuracy of several Padé approximants of $\hat{\phi}_5$ relative to the shooting method results on both sides of the branch cut.

behavior one expects from Padé approximants of a Cauchy-Stieltjes integral [32] or a more general analytic function with branch point singularities [33,34].

5 Conclusion

We have derived a recursive algorithm to compute successive terms of the Stokes expansion for finite-depth standing water waves and implemented it in arbitrary-precision arithmetic on a supercomputer. One advantage of the conformal mapping framework over previous graph-based approaches [13,14] is that the arguments of the hyperbolic functions in (2.18) depend only on time, which reduces the cost of re-expanding the composite power series that arise.

We carried out extensive numerical experiments to verify the correctness of the Stokes expansions by comparing them to standing waves computed by a shooting method [29] that we implemented in double and quadruple-precision using adaptive meshes and numerical continuation. While previous studies [26,27,28,29] have established a connection between nearby harmonic resonances and the branching structure of families of standing water waves, we look specifically at how small divisors in the recurrence activate new growth patterns among the Stokes coefficients. We find that the Stokes coefficients rapidly settle into geometric growth patterns as the expansion order ν increases, but the growth rate sometimes jumps in response to new small divisors entering the recurrence. This led us to define an inverse growth rate factor ρ_ν that serves as an effective radius of convergence for the truncated Stokes expansion of order ν . A clear connection between the large jumps in ρ_ν^{-1} in figure 4 and the corresponding small divisors is demonstrated for $\mu_0 \in \{1/4, 3/5\}$ in the electronic supplementary material.

In the examples we presented in detail, ρ_ν aligns with the amplitude where an imperfect bifurcation is observed using the shooting method. In these cases, we observe, for the first time, clusters of poles and zeros in the Padé approximants of the Stokes expansion near $\epsilon = \rho_\nu$ that suggest that previously observed [27] turning points in the bifurcation curves are branch point singularities of an analytic function. These poles and ze-

ros allow the Padé approximants to jump across disconnections in the bifurcation curves with remarkable accuracy on both sides of the branch cut. For unit-depth standing waves, the 149th-order Padé approximant of the period maintains 30 digits of accuracy for amplitudes up to $\epsilon = 0.3$, which is beyond the first two disconnections we identified, at $\epsilon = \rho_{149} = 0.139289$ and $\epsilon = 0.273808$. Neither of these disconnections are “observable” in double-precision using the shooting method alone. Mercer and Roberts [26] noted that high-frequency resonances are likely to be extremely weak (made quantitative by estimates from [24]), so only the dominant, low-frequency resonances will be observable in a finite truncation of the problem carried out numerically. Our high-precision numerics coupled with Padé techniques make it possible to locate and compute them.

For $\mu_0 = 1/16$, the smallest divisor for $2 \leq p \leq 24773$ is $\lambda_{2,2}$, which is not associated with a harmonic resonance. As a result, there is no imperfect bifurcation associated with this small divisor. Instead, as shown in the electronic supplementary material, the closest poles to the origin in the 109th order Padé approximant of the period lie on the imaginary ϵ -axis rather than the real axis. The same thing happens for $\mu_0 \in \{4, 10, 16\}$. Figure 10 of the electronic supplementary material shows that $|\lambda_{4,2}|$ is small in these cases, which becomes a zero-divisor in infinite depth but does not lead to an imperfect bifurcation in finite depth. Imaginary Padé poles close to the origin render the direct Stokes expansion almost useless for $\mu_0 \in \{10, 16\}$ since ρ_ν is so small (see Figure 4), but Padé approximation has the potential to extend the validity of the series to much larger amplitudes. Okamura [28] found that different weakly nonlinear results are obtained for the resonant (4, 2) coefficient of the Stokes expansion if the problem is formulated in infinite depth versus taking the infinite-depth limit of a finite-depth formulation. In future work, it would be interesting to compare the almost infinite-depth Padé expansions of the present paper to the infinite-depth expansions of Schwartz and Whitney [15] and to Okamura’s weakly nonlinear results.

Consistent with previous studies [26, 27, 29, 30, 19], we find that following the side branches of an imperfect bifurcation using the shooting method activates secondary standing waves that oscillate on top of the primary wave with different amplitudes and phases on different bifurcation branches. This leads to non-uniqueness for fixed values of wave amplitude or period. For example, solutions ABC in figure 5 have the same period $T = 8.45592$ but different wave heights ϵ . Since solutions A and C appear to oscillate around solution B , we regard B as the primary wave and the perturbation from B to A or from B to C as a finite-amplitude secondary wave. Nonlinearity can distort these secondary waves to deviate visibly from oscillating as scalar multiples of $\cos(px) \cos(jt)$. This is demonstrated in the electronic supplementary material, where we also consider small-amplitude secondary waves that have nearly the same period as the primary wave under the linearized equations of motion about the primary wave.

Finite-amplitude secondary waves are specific perturbations that maintain time-periodicity of the composite wave under the nonlinear evolution equations. The linear stability of standing waves and short-crested waves to arbitrary perturbations is an interesting problem that has been studied in [31, 60, 61, 62, 63]. Mercer and Roberts [31] reported that the onset of superharmonic instability for standing waves in infinite depth occurs at a crest acceleration of $A_c = 0.88928$ (or wave height of $\epsilon = 0.61683$). A conjugate pair of Floquet multipliers on the unit circle collide at $\lambda = 1$ when $A_c = 0.88928$ and split into two real Floquet multipliers $\{\lambda, \lambda^{-1}\}$ with $\lambda > 1$ when $A_c > 0.88928$. When the multipliers collide, there is a resonant solution of the linearized equations about the standing wave with the same period as the standing wave itself. The superharmonic instabilities discussed in [60, 61] also involve resonant linearized solutions. Wilkening [63] confirmed this mechanism

at $A_c = 0.88928$ and found several bubbles of instability at smaller values of A_c in which two pairs of Floquet multipliers collide elsewhere on the unit circle and split into a cluster of Floquet multipliers of the form $\{\lambda, \lambda^{-1}, \bar{\lambda}, \bar{\lambda}^{-1}\}$ with $|\lambda| > 1$. Further exploration of the stability of standing waves, e.g., near the bifurcations studied in the present paper, as well as the long-time dynamics of unstable perturbations, are interesting avenues for future research.

As one increases the order of the truncated Stokes expansion, new small divisors occasionally enter the recurrence that lead to new Padé poles close to the origin. We find that the Padé approximants continue to improve in accuracy at a given amplitude ϵ as new features of the bifurcation curve emerge at lower amplitude. This was shown in panel (b) of figure 7 for $\mu_0 = 1$ and in panels (b) and (d) of figure 9 for $\mu_0 = 3/5$. In the latter case, the poles at $\epsilon = 0.013403$ and $\epsilon = 0.063553$ do not appear until $\nu = 93$ and $\nu = 117$, respectively. The former pole appears shortly before the large jump in ρ_ν^{-1} for $\mu_0 = 3/5$ in figure 4. Rigorous existence proofs of standing waves [64,65,66] and temporally quasi-periodic water waves [67] employ a Nash-Moser iteration to rapidly converge to a solution through a sequence of less regular spaces. However, this only establishes existence for values of the amplitude parameter in a Cantor set. An interesting question is whether the branch cuts we observe in the Padé approximants will continue to emerge on smaller and smaller scales as $\nu \rightarrow \infty$, leaving behind similar Cantor sets.

Theorem 3.1 shows that for almost every fluid depth, and every rational depth, the divisors $\lambda_{p,j}$ are bounded below by a slowly decaying function of the wave number p . Our numerical results show that ρ_ν tends to stabilize at fixed values over many orders ν , but occasionally drops to a smaller value when the geometric growth patterns of the Stokes coefficients re-organize in response to a new smallest divisor entering the recurrence. We do not believe the lower bounds of Theorem 3.1 will prevent ρ_ν from approaching zero, but they might ensure that it approaches zero slowly enough that the Padé approximants are convergent at amplitudes where a solution exists. This is discussed further in the electronic supplementary material.

In the present work, we focused on continued fraction expansions of single components of the Stokes expansion, namely T , $\hat{\phi}_p$ and $\hat{\eta}_p$ in (4.14) and (4.15). Roberts [13] and Marchant and Roberts [14] also considered Padé approximants of scalar quantities associated with Stokes expansions of short-crested waves. It would be natural in future work to study rational approximations of the Stokes expansions for which all the components of the solution at a given order share a common denominator. Simultaneous Padé approximation (see, e.g., [68], chapter 8) is one possible approach, though the linear algebra could become highly ill-conditioned. Another idea is to study rational approximations with respect to additional variables (beyond ϵ). If the continued fraction coefficients d_n and $\tilde{d}_{p,n}$ in (4.14) and (4.15) are well-approximated by rational functions of the depth parameter and have simple pole singularities at a resonant depth, the truncated Padé approximants at a given order ν would become bivariate rational functions of depth and amplitude. This would use Robert's idea [24] to extend the validity of a Stokes expansion past discontinuities in the bifurcation curve (to larger values of ϵ) for many depths simultaneously. It would also provide a satisfactory answer to a concern raised by Concus [11] that a small perturbation of the depth would cause discontinuous changes in the Stokes expansion coefficients. Although these coefficients change discontinuously, the solution itself (the Padé approximant) depends continuously on depth in a neighborhood of the resonant depth on the large-amplitude side of the discontinuity. There will only be finitely many resonant depths for a given truncation order of the Stokes expansion, and this approach could be used to represent solutions in a neighborhood of any of them. One could also use Padé

techniques for Fourier series [69] to obtain a rational function of e^{-iw} to approximate the Fourier series one obtains by truncating the sums in (2.13) to a finite range $1 \leq p \leq p_{\max}$. This would generalize (from traveling waves to standing waves) the results of Dyachenko et al [70] and Lushnikov [71] on branch point singularities in the upper half-plane obtained by analytic continuation of the conformal map. Standing waves would have the new feature that these singularities evolve in time.

Acknowledgments. The authors thank the anonymous reviewers for many valuable comments and suggestions that strengthened the results of the paper. AA was supported in part by the ARCS Foundation through the ARCS Scholar program. JW was supported in part by the National Science Foundation under award number DMS-1716560 and by the Department of Energy, Office of Science, Applied Scientific Computing Research, under award number DE-AC02-05CH11231. This research used the Lawrence Livermore computational cluster resource provided by the IT Division at the Lawrence Berkeley National Laboratory and the Savio computational cluster provided by the Berkeley Research Computing program at the University of California, Berkeley (supported by the UC Berkeley Chancellor, Vice Chancellor for Research, and Chief Information Officer).

References

1. Longuet-Higgins MS. 1950 A theory of the origin of microseisms. *Phil. Trans. Royal Soc. London A* **243**, 1–35.
2. Arduin F, Herbers THC. 2013 Noise generation in the solid Earth, oceans, and atmosphere, from non-linear interacting surface gravity waves in finite depth. *J. Fluid Mech.* **716**, 316–348.
3. McAllister M, Draycott S, Calvert R, Davey T, Dias F, van den Bremer T. 2024 Three-dimensional wave breaking. *Nature* **633**, 601–607.
4. Renzi E, Dias F. 2012 Resonant behaviour of an oscillating wave energy converter in a channel. *J. Fluid Mech.* **701**, 482–510.
5. Peregrine D. 2003 Water-wave impact on walls. *Annu. Rev. Fluid Mech.* **35**, 23–43.
6. Penney WG, Price AT. 1952 Finite periodic stationary gravity waves in a perfect liquid, Part II. *Phil. Trans. R. Soc. London A* **244**, 254–284.
7. Bridges T, Laine-Pearson F. 2004 Nonlinear counterpropagating waves, multisymplectic geometry, and the instability of standing waves. *SIAM J. Appl. Math.* **64**, 2096–2120.
8. Wilkening J. 2021 Traveling-standing water waves. *Fluids* **6**, 187:1–35.
9. Tadjbakhsh I, Keller JB. 1960 Standing surface waves of finite amplitude. *J. Fluid Mech.* **8**, 442–451.
10. Concus P. 1962 Standing capillary-gravity waves of finite amplitude. *J. Fluid Mech.* **14**, 568–576.
11. Concus P. 1964 Standing capillary-gravity waves of finite amplitude: Corrigendum. *J. Fluid Mech.* **19**, 264–266.
12. Verma GR, Keller JB. 1962 Three-Dimensional Standing Surface Waves of Finite Amplitude. *Physics of Fluids* **5**, 52–56.
13. Roberts AJ. 1983 Highly nonlinear short-crested waves. *J. Fluid Mech.* **135**, 301–321.
14. Marchant TR, Roberts AJ. 1987 Properties of short-crested waves in water of finite depth. *J. Austral. Math. Soc. Ser. B* **29**, 103–125.
15. Schwartz LW, Whitney AK. 1981 A semi-analytic solution for nonlinear standing waves in deep water. *J. Fluid Mech.* **107**, 147–171.
16. Amick CJ, Toland JF. 1987 The semi-analytic theory of standing waves. *Proc. Roy. Soc. Lond. A* **411**, 123–137.
17. Iooss G. 1999 Semi-analytic theory of standing waves in deep water, for several dominant modes. *Proc. R. Soc. Lond. A* **455**, 3513–3526.
18. Abassi A, Wilkening J. 2024 The semi-analytic theory and computation of standing gravity-capillary waves. (in preparation).
19. Shelton J, Milewski P, Trinh PH. 2023 On the structure of parasitic gravity-capillary standing waves in the small surface tension limit. *J. Fluid Mech.* **972**, R6:1–12.
20. Silverman JH, Tate JT. 2015 *Rational Points on Elliptic Curves*. Switzerland: Springer International Publishing 2nd edition.
21. Chen B, Saffman P. 1979 Steady Gravity-Capillary Waves on Deep Water I. Weakly Nonlinear Waves. *Stud. Appl. Math.* **60**, 183–210.
22. Schwartz L, Vanden-Broeck JM. 1979 Numerical solution of the exact equations for capillary-gravity waves. *J. Fluid Mech.* **95**, 119–139.

23. Chen B, Saffman P. 1980 Steady Gravity-Capillary Waves on Deep Water II. Numerical Results for Finite Amplitude. *Stud. Appl. Math.* **62**, 95–111.
24. Roberts AJ. 1981 The behaviour of harmonic resonant steady solutions to a model differential equation. *Quarterly J. Mech. Appl. Math.* **34**, 287–310.
25. Vanden-Broeck JM. 1984 Nonlinear gravity-capillary standing waves in water of arbitrary uniform depth. *J. Fluid Mech.* **139**, 97–104.
26. Mercer GN, Roberts AJ. 1994 The form of standing waves on finite depth water. *Wave Motion* **19**, 233–244.
27. Smith DH, Roberts AJ. 1999 Branching behavior of standing waves — the signatures of resonance. *Phys. Fluids* **11**, 1051–1064.
28. Okamura M. 1997 Resonant standing waves on water of uniform depth. *J. Phys. Soc. Jpn.* **66**, 3801–3808.
29. Wilkening J, Yu J. 2012 Overdetermined shooting methods for computing standing water waves with spectral accuracy. *Comput. Sci. Discovery* **5**, 014017.
30. Rycroft CH, Wilkening J. 2013 Computation of three-dimensional standing water waves. *J. Comput. Phys.* **255**, 612–638.
31. Mercer GN, Roberts AJ. 1992 Standing waves in deep water: Their stability and extreme form. *Phys. Fluids A* **4**, 259–269.
32. Allen GD, Chui CK, Madych WR, Narcowich FJ, Smith PW. 1976 Padé approximation of Stieltjes series. *J. Approx. Theory* **14**, 302–316.
33. Stahl H. 1997 The convergence of Padé approximants to functions with branch points. *J. Approx. Theory* **91**, 139–204.
34. Yamada HS, Ikeda KS. 2014 A numerical test of Padé approximation for some functions with singularity. *Int. J. Computational Math.* **2014**, 587430:1–17.
35. Craig W, Sulem C. 1993 Numerical simulation of gravity waves. *J. Comput. Phys.* **108**, 73–83.
36. Dyachenko AI, Zakharov VE, Kuznetsov EA. 1996 Nonlinear dynamics of the free surface of an ideal fluid. *Plasma Phys. Reports* **22**, 829–840.
37. Ruban VP. 2005 Water waves over a time-dependent bottom: exact description for 2D potential flows. *Phys. Letters A* **340**, 194–200.
38. Turner MR, Bridges TJ. 2016 Time-dependent conformal mapping of doubly-connected regions. *Adv. Comput. Math.* **42**, 947–972.
39. Wilkening J, Zhao X. 2023 Spatially quasi-periodic water waves of finite depth. *Proc. R. Soc. A* **479**, 20230019:1–28.
40. Bell ET. 1934 Exponential polynomials. *Ann. Math.* pp. 258–277.
41. Baker A. 1975 *Transcendental Number Theory*. London–New York: Cambridge University Press.
42. Borosh I, Fraenkel AS. 1972 A generalization of Jarník’s theorem on Diophantine approximations. *Indagationes Mathematicae* **75**, 193–201.
43. Rudin W. 1987 *Real and Complex Analysis*. New York: McGraw Hill third edition.
44. Schmidt WM. 1964 Metrical theorems on fractional parts of sequences. *Trans. Amer. Math. Soc.* **110**, 493–518.
45. Stein EM, Shakarchi R. 2003 *Fourier Analysis, an Introduction*. Princeton: Princeton University Press.
46. Lorentzen L, Waadeland H. 2008 *Continued Fractions, Volume 1: Convergence Theory*. Amsterdam: Atlantis Press second edition.
47. Hančl J, Leppälä K, Matala-aho T, Törmä T. 2015 On irrationality exponents of generalized continued fractions. *J. Number Theory* **151**, 18–35.
48. Fousse L, Hanrot G, Lefèvre V, Pélissier P, Zimmermann P. 2007 MPFR: A multiple-precision binary floating-point library with correct rounding. *ACM Trans. Math. Software* **33**, 13:1–15.
49. Chopp DL. 2019 *Introduction to High Performance Scientific Computing*. Philadelphia: SIAM.
50. Press WH, Teukolsky SA, Vetterling WT, Flannery BP. 2007 *Numerical Recipes, The Art of Scientific Computing*. Cambridge: Cambridge University Press 3rd edition.
51. Goedecker S. 1997 Fast radix 2, 3, 4, and 5 kernels for fast Fourier transformations on computers with overlapping multiply-add instructions. *SIAM J. Sci. Comput.* **18**, 1605–1611.
52. Domb C, Sykes M. 1957 On the susceptibility of a ferromagnetic above the Curie point. *Proc. Royal Soc. Lond. A* **240**, 214–228.
53. Abassi A, Wilkening J. 2025 Convergence of the Padé approximants of a function with a sequence of branch cuts that accumulate at the origin. (in preparation).
54. Hairer E, Norsett SP, Wanner G. 2000 *Solving Ordinary Differential Equations I: Nonstiff Problems, 2nd Edition*. Berlin: Springer.
55. Dutt A, Greengard L, Rokhlin V. 2000 Spectral deferred correction methods for ordinary differential equations. *BIT Numer. Math.* **40**, 241–266.
56. Wilkening J. 2011 Breakdown of self-similarity at the crests of large amplitude standing water waves. *Phys. Rev. Lett* **107**, 184501.
57. Wilkening J, Zhao X. 2023 Spatially quasi-periodic bifurcations from periodic traveling water waves and a method for detecting bifurcations using signed singular values. *J. Comput. Phys.* **478**, 111954:1–34.
58. Cuyt A, Petersen VB, Verdonk B, Waadeland H, Jones W. 2008 *Handbook of Continued Fractions for Special Functions*. Dordrecht: Springer.

59. Gonnet P, Güttel S, Trefethen LN. 2013 Robust Padé Approximation via SVD. *SIAM Review* **55**, 101–117.
60. Ioualalen M, Kharif C. 1993 Stability of three-dimensional progressive gravity waves on deep water to superharmonic disturbances. *European J. Mech B, Fluids* **12**, 401–414.
61. Ioualalen M, Roberts A, Kharif C. 1996 On the observability of finite-depth short-crested water waves. *J. Fluid Mech.* **322**, 1–19.
62. Ioualalen M, Kharif C, Roberts A. 1999 Stability regimes of finite depth short-crested water waves. *J Physical Oceanography* **29**, 2318–2331.
63. Wilkening J. 2020 Harmonic stability of standing water waves. *Q. Appl. Math.* **78**, 219–260.
64. Plotnikov PI, Toland JF. 2001 Nash-Moser theory for standing water waves. *Arch. Ration. Mech. An.* **159**, 1–83.
65. Iooss G, Plotnikov PI, Toland JF. 2005 Standing waves on an infinitely deep perfect fluid under gravity. *Arch. Rat. Mech. Anal.* **177**, 367–478.
66. Alazard T, Baldi P. 2015 Gravity capillary standing water waves. *Arch. Rat. Mech. Anal.* **217**, 741–830.
67. Berti M, Montalto R. 2016 *Quasi-periodic standing wave solutions of gravity-capillary water waves* vol. 263, *Memoirs of the American Mathematical Society*. American Mathematical Society.
68. Baker, Jr GA, Graves-Morris P. 2009 *Padé approximants* vol. 59, *Encyclopedia of Mathematics and its Applications*. Cambridge: Cambridge University Press second edition.
69. Daras NJ. 2000 Padé and Padé-type approximation for 2π -periodic L^p functions. *Acta Appl. Math.* **62**, 245–343.
70. Dyachenko SA, Lushnikov PM, Korotkevich AO. 2016 Branch cuts of Stokes wave on deep water. Part I: Numerical solution and Padé approximation. *Stud. Appl. Math.* **137**, 419–472.
71. Lushnikov PM. 2016 Structure and location of branch point singularities for Stokes waves on deep water. *J. Fluid Mech.* **800**, 557–594.

Electronic supplementary material

In section [S1](#) we plot the smallest divisor that arises at each wave number for the depths considered in section [4.1](#) and examine how the growth patterns in the Stokes coefficients change when unusually small divisors enters the recurrence. We also fill in details on the Domb-Sykes plot analysis in panels (d) and (e) of figure [4](#) and give an example where the rapid growth of the Stokes expansion coefficients corresponds to Padé poles on the imaginary ϵ -axis near the origin. In section [S2](#), we show that there is no fluid depth for which $\lambda_{p,j}$ in [\(1.1\)](#) can be uniformly bounded away from 0 for $p \geq 2$. We also show by example that this does not automatically follow from the density of resonant depths, and that Padé approximants of an analytic function with a sequence of branch cuts that accumulate at the origin may or may not converge to the function at larger amplitudes, depending on how rapidly the analog of ρ_ν from [\(4.7\)](#) converges to zero as $\nu \rightarrow \infty$. In section [S3](#), we prove Theorem [3.1](#), which shows that for almost every fluid depth, the small divisors are bounded below by a slowly-decaying function of the wave number. We demonstrate for the case $\mu_0 = 1/16$ that Theorem [3.1](#) gives a good prediction of how fast the small divisors decay in practice. We also state and prove a theorem on the presence of many large divisors in the proximity of any small divisor. In section [S4](#), we present a brief derivation of the forcing terms that appear in the ODEs of section [3](#). In section [S5](#), we discuss computational aspects of the algorithm and provide implementation details for our arbitrary-precision parallel algorithm. In section [S6](#), we discuss the effects of finite-precision arithmetic and how to estimate floating-point errors. In section [S7](#), we investigate the secondary standing waves that are activated with different phases and amplitudes by following the side branches of the bifurcation curves of section [4.2](#), focusing on how nonlinearity affects the shapes of the secondary waves. Finally, in section [S8](#), we show how to identify which harmonic resonance is responsible for a bifurcation branch by studying the singular vector corresponding to the smallest singular value of the Jacobian of a solution near the imperfect bifurcation.

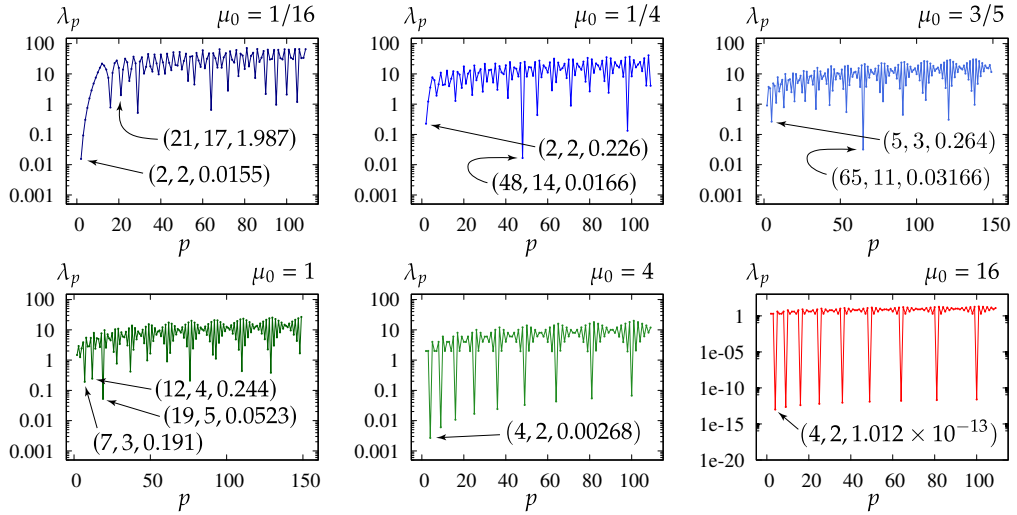


Fig. 10 Smallest divisor that will arise in the calculation for each spatial Fourier mode $p \geq 2$. The labels (p, j, λ_p) give the parameters of the smallest λ_p 's encountered, where j is the argmin in (3.11).

S1. Small divisors, growth rates, and imaginary Padé poles

The jumps in growth rate in panels (a,b) of Figure 4 appear to be caused by new small divisors entering the recurrence at certain orders when solving (3.10) for $\alpha_{p,n,j}$. This alters the growth patterns of the Stokes expansion coefficients $\alpha_{p,n,j}$, $\beta_{p,n,j}$, $\gamma_{p,n,j}$, $\mu_{n,j}$ and σ_n on subsequent iterations. This observation is implicitly made in [13, 14], though the authors focus on zero divisors of nearby resonant depths rather than small divisors of the actual recurrence. Figure 10 shows the smallest divisor λ_p associated with each spatial mode, defined in (3.11) above. Notable small divisors at each depth are labeled with triples (p, j, λ_p) , where j is the argmin in (3.11).

These small divisors have a strong effect on the Stokes expansion coefficients. In the case $\mu_0 = 1/4$, the smallest divisor seen for $2 \leq p \leq 47$ is $\lambda_2 = 0.226$. It then drops by a factor of 13.6 at $p = 48$ to $\lambda_{48} = 0.0166$. The $(p, j) = (48, 14)$ mode becomes active at order $\nu = 48$, but it starts out much smaller in magnitude than the largest mode of that order. Specifically, $\alpha_{48,0,14} = 6.62 \times 10^{66}$ while $\alpha_{2,23,2} = -1.735 \times 10^{82}$. From that point, as ν increases through even integers, $\alpha_{48,(\nu-48)/2,14}$ grows faster than any other mode of order ν . By the time $\nu = 70$, $\alpha_{48,11,14} = 1.463 \times 10^{123}$ overtakes $\alpha_{2,34,2} = 4.22 \times 10^{121}$ as the largest (in magnitude) coefficient $\alpha_{p,n,j}$ with $p + 2n = \nu$ and $j \in E_\nu$. This is precisely where the jump in the growth rate $\rho_\nu^{-1} = \sqrt{A_\nu/A_{\nu-2}}$ of the norms A_ν defined in (4.4) appears in panel (a) of figure 4 for the case $\mu_0 = 1/4$. Similar observations hold for the case $\mu_0 = 3/5$, where the small divisor $\lambda_{65,11} = 0.03166$ leads to the jump in ρ_ν^{-1} at $\nu = 103$. The case $\mu_0 = 1$ is interesting as there is a cluster of 3 moderately small divisors $\lambda_{p,j}$ with $(p, j) \in \{(7, 3), (12, 4), (19, 5)\}$. We find that $\alpha_{19,n,5}$ is among the largest modes for $n \geq 23$, which is the transition region where ρ_ν^{-1} moves up to the next plateau for $\nu = 19 + 2n \geq 65$ in panel (b) of figure 4 for $\mu_0 = 1$. Small divisors are not the only consideration in determining which mode will be largest: the right-hand side $-S_{p,n,j}$ in (3.10) depends on the previously computed $\alpha_{q,m,l}$ in a complicated way. This causes other modes $\alpha_{p,n,j}$ with (p, j) near $(19, 5)$ to also be large for $n \geq 23$ and $\mu_0 = 1$.

Before discussing the case of imaginary Padé poles, we fill in some details omitted in section 4.1 on how we estimate the radius of convergence of the Stokes expansion from the Domb-Sykes plots in panels (d,e,f) of figure 4. We fit the data $(x_\nu, y_\nu) = (1/\nu, \rho_\nu^{-1})$ with the polynomial $q(x)$ of degree d that minimizes $f = \sum_{\nu \in \mathcal{I}} |y_\nu - q(x_\nu)|^2 w_\nu$ with $w_\nu = C/(D - \nu)^2$, $D = 4 + \max_{\nu \in \mathcal{I}} \nu$, and C chosen so that $\sum_{\nu \in \mathcal{I}} w_\nu = 1$. We used the parameters

d	$\mu_0 = 1$ 2	$\mu_0 = 1/16$ 4	$\mu_0 = \infty$ 8
\mathcal{I}	$\{\nu : 10 \leq \nu \leq 54\} \cap 2\mathbb{Z}$	$\{\nu : 20 \leq \nu \leq 109\} \cap 2\mathbb{Z}$	$\{\nu : 20 \leq \nu \leq 149\}$

After finding $q(x)$, we estimate $\lim_{\nu \rightarrow \infty} \rho_\nu^{-1} = q(0)$ to obtain the extrapolated radius of convergence $q(0)^{-1}$. Omitting the odd integers eliminates oscillations in the residual $[y_\nu - q(x_\nu)]$ that arise for $\mu_0 = 1/16$ and $\mu_0 = 1$. The results for $q(0)$ agree to all the digits reported in figure 4 if we instead omit the even integers. When $\mu_0 = \infty$, these oscillations are not present, so we include both odd and even integers in \mathcal{I} . More details on choosing the polynomial order d to maximize accuracy without over-fitting will be given elsewhere [18]. This choice of weight w_ν favors accuracy for larger values of ν , where x_ν is closer to 0. As discussed in section 4.1 and shown in panel (c) of figure 4, this extrapolation could be wrong if there are jumps in ρ_ν^{-1} at higher orders, beyond the range \mathcal{I} used to fit the data. It will be shown in [18] that no such jumps are encountered up to order $\nu = 641$ for $\mu_0 = \infty$, and the polynomial $q(x)$ computed here from $20 \leq \nu \leq 149$ satisfies $\max_{150 \leq \nu \leq 641} (|y_\nu - q(x_\nu)|/y_\nu) \leq 8.0 \times 10^{-11}$. This suggests that the radius of convergence for the infinite depth case (the Schwartz and Whitney expansion) is $q(0)^{-1} = 0.301262103 > 0$. However, we have some doubts about this conclusion as Padé approximants of individual components of the solution (T , $\hat{\phi}_p$ and $\hat{\eta}_p$) possess extremely closely spaced Froissart doublets inside this radius, similar to what happens in the $\mu_0 = 1/16$ case reported below. We will explore this in more detail in [18]. We are not able to reach such high orders in finite depth.

For $\mu_0 \in \{1/4, 3/5, 1\}$, the small divisors $\{\{\lambda_{48,14}\}, \{\lambda_{5,3}, \lambda_{65,11}\}, \{\lambda_{7,3}, \lambda_{12,4}, \lambda_{19,5}\}\}$ lead to imperfect bifurcations in the family of solutions. But for $\mu_0 = 1/16$, the small divisor $\lambda_{2,2}$ is not associated with a harmonic resonance since the first resonance in finite depth occurs at $(p, j) = (5, 3)$. Panels (a) and (b) of figure 11 show the poles and zeros of the 109th-order Padé approximant of the period, T . As ν increases, poles and zeros become more densely distributed on the imaginary axis with an accumulation point emerging at the blue circle of radius $q(0)^{-1} = 0.000267885$, which is the extrapolated radius of convergence of the Stokes expansion computed from the Domb-Sykes plot, as described above. The dotted red circle in panel (b) has radius $\rho_{109} = 0.000271628$, which is slightly larger than $q(0)^{-1}$ since $q(x)$ in panel (d) of figure 4 increases as $x \rightarrow 0^+$. All but one pole on the positive imaginary axis in panels (a) and (b) of figure 11 lie outside of the blue circle. (The conjugate of any pole or zero is also a pole or zero, so we focus on those in the upper half-plane.) The one exception is the Froissart doublet labeled FD in panel (b). This doublet consists of a pole z_p and a zero z_0 on the imaginary axis near $0.00022524i$ that are separated by a relative distance of only $|z_p - z_0|/|z_p| = 4.4 \times 10^{-21}$. Details confirming that 212-bit (64-digit) floating-point arithmetic is sufficient to compute this relative distance are given in section S6 below.

Because the pole and zero of the Froissart doublet are so close together, the Padé approximant $[27/27]_\tau(\epsilon^2) = P(\epsilon^2)/Q(\epsilon^2)$ agrees to more than 20 digits on the real axis with the rational function $[P(\epsilon^2)/(\epsilon^2 - z_0^2)]/[Q(\epsilon^2)/(\epsilon^2 - z_p^2)]$, which has all its poles outside of the blue circle in figure 11. The leading terms of their Taylor expansions will also be

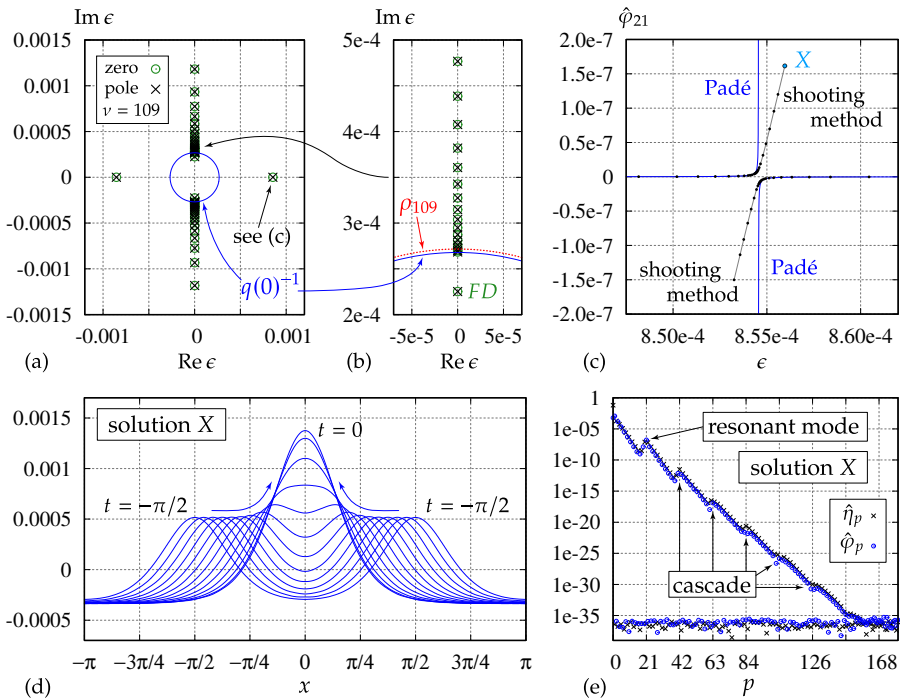


Fig. 11 Standing waves of dimensionless depth $\mu_0 = 1/16$. (a,b) Poles and zeros of the 109th-order Padé approximant of the period T . (c) A bifurcation plot of solutions near the real pole at $\epsilon = 0.000854552$. (d) Snapshots of solution X at times $t \in \mathcal{T}_{12}$ from (4.13). (e) The Fourier spectrum of the initial conditions of solution X .

close to each other, which helps explain why ρ_{109} and $q(0)^{-1}$ are close to the second-smallest pole rather than the pole of the Froissart doublet. This doublet persists over many consecutive orders, appearing first at order $\nu = 67$, and remains close to $0.00022524i$ for $75 \leq \nu \leq 109$. This suggests that there is an actual singularity near this location that should eventually cause ρ_ν to drop below 0.00022524 . If the underlying singularity is not a simple pole, additional poles may appear near this one in higher-order Padé approximants. The other poles on the imaginary axis in panel (a) are evidence that branch cuts may exist along the imaginary axis above and below the blue circle. We will see in section S3 that $\lambda_p \geq \max(0.0155, p^{-0.57})$ for $2 \leq p \leq 2.5 \times 10^{22}$, which is a slowly decaying lower bound. The rate at which ρ_ν approaches zero as $\nu \rightarrow \infty$ (assuming it does so) depends on how these small divisors interact with the terms in the right-hand side $-S_{p,n,j}$ in (3.10), and on whether the abundance of large divisors discussed in section S3 below are helpful in preventing rapid decay. (A slower decay rate in ρ_ν appears to improve the convergence of the Padé approximants, as discussed in section S2 below.)

In panel (a) of figure 11, we see that the 109th-order Padé approximant of T has a pole-zero pair on the real ϵ -axis at $\epsilon = 0.000854552$. (There is another such pair at $\epsilon = -0.000854552$). The relative distance between the pole and zero is 6.0×10^{-11} . This pole-zero pair persists over many consecutive orders, appearing first at order $\nu = 69$ and remaining close to $\epsilon = 0.00085$ for $81 \leq \nu \leq 109$. We used the Padé approximants of T and of the Fourier modes $\hat{\phi}_p$ and $\hat{\eta}_p$ in (4.12) as an initial guess in the shooting method to construct a bifurcation plot via numerical continuation near this amplitude, shown in panel (c) of figure 11. The most resonant mode, $\hat{\phi}_{21}$, is plotted versus ϵ . The black markers show

shooting-method solutions while the blue curve shows the 109th-order Padé approximant $\epsilon^{21}[22/22]_{\tilde{\tau}_{21}}(\epsilon^2)$ of $\hat{\varphi}_{21}$ obtained by truncating the continued fraction (4.15) at $n = 44$. Instead of turning points that leave a gap with no solutions, there are two solutions at each value of ϵ in a neighborhood of $\epsilon = 0.000854552$, one on each bifurcation branch.

Panel (d) of figure 11 shows snapshots of the time-evolution of solution X over a quarter period, where X is the labeled solution on the upper bifurcation branch in panel (c). Since the depth $\mu_0 = 1/16$ is small in comparison to the wavelength 2π , standing waves take the form of counter-propagating solitary waves that repeatedly collide at dimensionless times $t \in 2\pi\mathbb{Z}$ and $t \in \pi(1 + 2\mathbb{Z})$ to form rest states with localized peaks centered at $x = 0$ and $x = \pm\pi$, respectively. While secondary standing waves are not visibly active in this solution, the Fourier spectrum of the initial condition, shown in panel (e), suggests that a resonance in the 21st spatial Fourier mode leads to a cascade of peaks at wave numbers p that are multiples of 21. The smallest divisor associated with $p = 21$ is the $(p, j) = (21, 17)$ mode labeled in figure 10. Using the method described below in section S8, we confirm that there is a solution of the linearized water wave equations about solution X that contains 21 spatial oscillations and 17 temporal oscillations and is nearly time-periodic with the same period as X , namely $T = 25.0633$. This small-amplitude, secondary standing wave solution corresponds to the smallest singular value of the Jacobian of solution X , which is $\sigma_{\min} = 1.179 \times 10^{-6}$. The second-smallest and largest singular values are 0.00144 and 1.407, respectively. We omit a contour plot of the linearized solution in the interest of space and defer a discussion of the method to section S8 below. Solution X was computed in quadruple-precision using $M = 432$ spatial gridpoints; 288 timesteps of a 15th-order spectral deferred correction method [55] over a quarter period; and $d = 140$ unknown initial conditions in (4.10), where $\hat{\varphi}_{21}$ is omitted from the list of unknowns and specified as an amplitude parameter. It is interesting that the $(21, 17)$ mode becomes much more resonant evolving over solution X than over flat water. The divisor for this mode is not particularly small: $|\lambda_{21,17}| = 1.987$.

S2. Divergence of the Stokes expansion and convergence of its Padé approximants

Roberts [24, 13] concludes from the density of resonant depths that the asymptotic expansions of standing and short-crested water waves have a zero radius of convergence for all values of the depth parameter. This conclusion is re-iterated in [14, 26, 61, 27, 62]. We agree that this is likely to be true but disagree that it automatically follows from the density of resonant depths. For a given non-resonant depth, the recursion of section 3.2 is a specific procedure and nearby resonances enter into it only through division by $\lambda_{p,j}$ in (3.10). Resonant depths lead to zero-divisors while non-resonant depths could potentially lead to small divisors.

A distinction should be made between nearby resonant parameters and small divisors. This is best illustrated for the gravity-capillary wave problem in infinite depth [18], where the Stokes expansion recursion involves division by $\lambda_{p,j}^{\text{cap}}$ from (1.1) instead of $\lambda_{p,j}$. We have discovered that there are many values of B in (1.1) for which $\lambda_p^{\text{cap}} = \min_{j \in p+2\mathbb{Z}} |\lambda_{p,j}^{\text{cap}}|$ is bounded away from 0 for all $p \geq 2$, even though B is an accumulation point of resonant Bond numbers. We will explore this in more detail elsewhere [18], but give the example $B = 1$ here. The equation $y^2 = x^3 + 4x$ is an elliptic curve whose integral points are enumerated in [20] by constructing a generating set for the Mordell-Weil group of rational points on the curve. The only integer solutions (with $y \geq 0$) turn out to be $(x, y) = (0, 0)$ and $(x, y) = (2, \pm 4)$; see Example 3.11 of [20]. Setting $x = 2p$ and $y = 4j$, we obtain

$16j^2 = 8p^3 + 8p$, i.e., $\lambda_{p,j}^{\text{cap}} = 0$. If p and j are integers, so are x and y , so the only solutions of $\lambda_{p,j}^{\text{cap}} = 0$ are $(p, j) = (0, 0)$ and $(p, j) = (1, \pm 1)$. It follows that $\lambda_p^{\text{cap}} = \min_{j \in p+2\mathbb{Z}} |\frac{1}{2}(p + p^3) - j^2| \geq 1$ for $p \geq 2$. However, setting $B^{(m)} = (1 - \frac{1}{2m^4})$ for $m \in \mathbb{N}$, one finds that $\lambda_{p,j}^{\text{cap}}(B^{(m)}) = 0$ for $j = 2m^3$ and $p = 2m^2$, so $B^{(m)}$ is a sequence of resonant Bond numbers converging to $B = 1$. It is an open question whether the Stokes expansion has a positive radius of convergence in such cases.

For the finite-depth problem with zero surface tension, there is no depth μ_0 for which λ_p is uniformly bounded away from 0 for all $p \geq 2$. This is equivalent to the assertion in Theorem 3.1 that $\mathcal{E}_{-1/2}$ is the empty set; see section S3 below. Thus, for every depth, there will be arbitrarily small divisors eventually, but for almost every depth, $|\lambda_{p,j}|$ can only become small when p is large, as quantified by Theorem 3.1. Determining whether the algorithm of section 3.2 leads to a series with a positive radius of convergence is difficult since the formulas for the forcing terms $T_{p,n}^r$ given in (S4.2)–(S4.8) below, are nonlinear and contain factors such as $q\alpha_{q,k}$ or $\dot{\alpha}_{q,l}(t) = \sum_{j \in E_{q+2l}} ij\alpha_{q,l,j}e^{ijt}$ in which a spatial or temporal derivative amplifies higher-frequency modes in proportion to the mode index q or j . We agree with previous authors [24, 13, 14, 26, 61, 27, 62] that it is likely that the Stokes expansion diverges for every fluid depth. We believe that the bound $\lambda_p \geq \min(a, p^{-\frac{1}{2}-\delta})$ in Theorem 3.1, together with the presence of many large divisors (see section S3 below), will limit the growth rate of the Stokes coefficients so that ρ_ν in (4.7) approaches zero slowly. A reasonable conjecture is that if $\mu_0 \in \mathcal{E}_\delta$, there exist $C > 0$ and $\nu_0 \geq 3$, both depending on μ_0 , such that $\rho_\nu \geq C\nu^\theta$ for $\nu \geq \nu_0$. The dependence of θ on δ would have to be determined in the course of proving the conjecture. One can hope for $\theta = -\frac{1}{2} - \delta$, but accounting for factors in the recurrence associated with differentiation such as q and j discussed above might require a larger shift, e.g., $\theta = -1 - \delta$ or $\theta = -\frac{3}{2} - \delta$.

Limiting the rate at which ρ_ν approaches zero via $\rho_\nu \geq C\nu^\theta$ with $C > 0$, $\theta < 0$ and $|\theta|$ small appears to be critical for the convergence of the Padé approximants of the Stokes expansion. To gain intuition, let $\beta \in \{1, 2, \dots, 20\}$ and consider the function

$$f(z) = \sum_{k=0}^{\infty} \frac{z^{50k}}{\pi} \int_{-r_k}^{r_k} \frac{\sqrt{r_k^2 - s^2}}{a_k + s - z} ds, \quad a_k = \frac{1}{1 + (k+1)^\beta}, \quad r_k = 10^{-2-5k}, \quad (\text{S2.1})$$

which contains an infinite sequence of branch cuts $[a_k - r_k, a_k + r_k] \subset \mathbb{R}$ that shrink in size as they approach the origin. While $f(z)$ is infinitely differentiable at $z = 0$, its Maclaurin series has a radius of convergence of zero. The truncated continued fraction $z^{-1} \mathcal{K}_{n=0}^{v-1} \frac{d_n z}{1}$ of the formal power series $\sum_{\nu=0}^{\infty} c_\nu z^\nu$ with $c_\nu = \frac{1}{\nu!} f^{(\nu)}(0)$ gives the $[n/d]$ Padé approximant of $f(z)$ of order ν , where $n = \lfloor \nu/2 \rfloor$ and $d = \lceil \nu/2 \rceil$. The d_n are obtained from the c_ν using the quotient-difference (qd) algorithm [58, 46]. This example will be explored in detail in [53], where it is shown that $\rho_\nu^{-1} := c_\nu / c_{\nu-1}$ climbs through an infinite staircase with flat plateau regions separated by localized jumps, similar to what we imagine will happen in panels (a) and (b) in figure 4 as $\nu \rightarrow \infty$. The height of the plateau regions and the location of the jumps are accurately estimated in [53], where it is shown that $\rho_\nu \geq (\frac{\nu}{116})^{-\beta}$ for $1 \leq \beta \leq 20$. The question is whether these Padé approximants converge to $f(x)$ beyond all the branch cuts, e.g., at $x = 3/4$. Through numerical tests up to order $\nu = 1600$ using 6000 digits of precision and $\beta \in \{1, 2, 4, 8, 12, 16\}$, the error is found to decrease geometrically as ν increases, but the decay rate gets worse as β increases. Repeating this for $\beta = 20$, the error decreases initially but reaches a barrier that prevents the Padé approximants from converging to $f(3/4)$.

The reason for the breakdown in convergence has to do with whether poles of the Padé approximant continue to be distributed to low-index branch cuts to improve the quadrature approximation [32] of the Cauchy-Stieltjes integrals in (S2.1) as new branch cuts are encountered. The factor z^{50k} shifts the Maclaurin series of the k^{th} integral in (S2.1) to higher orders of the expansion, so a new branch cut is encountered when ν is a multiple of 50. The newly encountered branch cuts draw some of the Padé poles away from lower-index branch cuts, but the overall trend when β is small is that increasing ν increases the number of poles in each branch cut of index $k \leq \lfloor \nu/50 \rfloor$, often favoring lower-index branch cuts and leaving the most recently encountered branch cuts devoid of poles. By contrast, when $\beta = 20$, the high-index branch cuts rapidly acquire poles at the expense of low-index branch cuts. The number of poles in the $k = 0$ branch cut $[a_0 - r_0, a_0 + r_0] = [\frac{49}{100}, \frac{51}{100}]$ decreases from 25 at $\nu = 49$ to 9 at $\nu = 386$. It then alternates between 9 and 10 for $386 \leq \nu \leq 419$ and remains equal to 9 for $420 \leq \nu \leq 1600$, with no sign of rebounding. The error in the ν^{th} order Padé approximant at $x = 3/4$ does not improve after $\nu = 12$ in this case. See [53] for details and further discussion of these results.

S3. Lower bounds on small and large divisors

In this section we prove Theorem 3.1 and perform a numerical test to show that the bounds in the theorem are indicative of what happens in practice. We also state and prove a theorem that as the wave number p increases, the spacing between potentially small divisors increases, as do the size and number of large divisors near every potentially small divisor, defined as a divisor bounded by $\coth(\mu_0)$ in magnitude. Most of these will not be a new “smallest divisor seen so far,” but even satisfying $|\lambda_{p,j}| \leq \coth(\mu_0)$ becomes increasingly unlikely. Recall from section 3.1 that

$$\lambda_{p,j} = p \frac{\tanh(p\mu_0)}{\tanh \mu_0} - j^2, \quad \lambda_p = \min_{j \in p+2\mathbb{Z}} |\lambda_{p,j}|, \quad (\text{S3.1})$$

and that we write $\lambda_{p,j}(\mu_0)$ and $\lambda_p(\mu_0)$ in contexts where multiple depths μ_0 are being discussed.

Theorem 3.1 *For each $\delta > 0$, the set*

$$\mathcal{E}_\delta = \left\{ \mu_0 > 0 \mid \exists a > 0 \text{ such that } \forall p \geq 2, \lambda_p(\mu_0) \geq \min(a, p^{-\frac{1}{2}-\delta}) \right\} \quad (\text{S3.2})$$

has full Lebesgue measure. For $\delta \leq 0$, \mathcal{E}_δ has Lebesgue measure 0. For $\delta \leq -\frac{1}{2}$, \mathcal{E}_δ is the empty set. If $\delta > \frac{1}{2}$ and $\mu_0 > 0$ is rational, then $\mu_0 \in \mathcal{E}_\delta$.

Proof To prove the first assertion, we will show that the complement $\mathcal{E}_\delta^c = (0, \infty) \setminus \mathcal{E}_\delta$ has measure zero. Fix $\delta > 0$ and $\mu_0 \in \mathcal{E}_\delta^c$. Then either μ_0 is a resonant depth or we can construct a sequence $\{(p_i, a_i)\}_{i=1}^\infty$ with the properties that $a_1 = 1$ and, for $i \geq 1$, $a_{i+1} = \lambda_{p_i}$ with p_i the smallest integer $p \geq 2$ satisfying $\lambda_p < \min(a_i, p^{-\frac{1}{2}-\delta})$. An induction argument shows that for $i \geq 1$, the last element of the finite sequence $\{\lambda_2, \lambda_3, \dots, \lambda_{p_i}\}$ is the unique smallest element, and $p_{i+1} > p_i$. For each $i \geq 1$, we can choose $j_i \geq 1$ to have the same parity as p_i and to satisfy $|\lambda_{p_i, j_i}| = \lambda_{p_i}$. (The argmin of the formula for λ_p with $p \geq 2$ is never $j = 0$.) This procedure yields a sequence $\{(p_i, j_i)\}_{i=1}^\infty$ satisfying

$$p_{i+1} > p_i \geq 2, \quad 0 < \lambda_{p_i} < p_i^{-\frac{1}{2}-\delta}, \quad \lambda_{p_{i+1}} < \lambda_{p_i}, \quad |\lambda_{p_i, j_i}| = \lambda_{p_i}, \quad (i \geq 1). \quad (\text{S3.3})$$

From $|\lambda_{p_i, j_i}| < p_i^{-\frac{1}{2}-\delta}$ and the triangle inequality, we have

$$\begin{aligned} |p_i - j_i^2 \tanh \mu_0| &= \left| \tanh(\mu_0) \lambda_{p_i, j_i} + p_i [1 - \tanh(p_i \mu_0)] \right| \\ &< \tanh(\mu_0) p_i^{-\frac{1}{2}-\delta} + p_i [1 - \tanh(p_i \mu_0)]. \end{aligned} \quad (\text{S3.4})$$

Since $\mu_0 > 0$ and $0 < (1 - \tanh x) \leq 2e^{-2x}$ for $x > 0$, there exists p_* large enough that

$$p^{\frac{3}{2}+\delta} [1 - \tanh(p\mu_0)] < (1 - \tanh \mu_0), \quad (p \geq p_*). \quad (\text{S3.5})$$

Choose i_* large enough that $p_i \geq p_*$ for $i \geq i_*$. Then

$$|p_i - j_i^2 \tanh \mu_0| < p_i^{-\frac{1}{2}-\delta}, \quad (i \geq i_*) \quad (\text{S3.6})$$

and, since $p_i \geq 2$,

$$j_i^2 \tanh \mu_0 - p_i < p_i^{-\frac{1}{2}-\delta} < \frac{1}{2} p_i \Rightarrow \frac{3}{2} p_i > j_i^2 \tanh \mu_0, \quad (i \geq i_*). \quad (\text{S3.7})$$

Equation (S3.6) now gives

$$|j_i^2 \tanh \mu_0 - p_i| < p_i^{-\frac{1}{2}\delta} \left(\frac{2}{3} j_i^2 \tanh \mu_0 \right)^{-\frac{1}{2}-\frac{1}{2}\delta} < j_i^{-1-\delta}, \quad (i \geq i_*), \quad (\text{S3.8})$$

where we increased i_* if necessary to achieve $p_i^{-\frac{1}{2}\delta} < \left(\frac{2}{3} \tanh \mu_0\right)^{\frac{1}{2}+\frac{1}{2}\delta}$ for $i \geq i_*$. We conclude that $\tanh \mu_0$ belongs to the set

$$\mathcal{F}_\delta = \left\{ x \in \mathbb{R} \mid \exists \text{ infinitely many pairs } (p, j) \in \mathbb{Z} \times \mathbb{N} \text{ s.t. } \left| x - \frac{p}{j^2} \right| < \frac{1}{j^{3+\delta}} \right\}. \quad (\text{S3.9})$$

Borosh and Fraenkel [42] proved that the Hausdorff dimension of \mathcal{F}_δ is $\frac{3}{3+\delta}$. Since this is less than 1, its Lebesgue measure is zero. We have established that

$$\mu_0 \in \tilde{\mathcal{F}}_\delta = \tanh^{-1}(\mathcal{F}_\delta \cap (0, 1)). \quad (\text{S3.10})$$

The inverse hyperbolic tangent function is absolutely continuous and increasing on any compact interval $[x_1, x_2] \subset (0, 1)$, so $\tanh^{-1}(\mathcal{F}_\delta \cap [x_1, x_2])$ has measure zero by Theorem 7.18 of [43]. It follows that $\tilde{\mathcal{F}}_\delta$ has measure zero. We conclude that \mathcal{E}_δ^c is a subset of the union of $\tilde{\mathcal{F}}_\delta$ with the countable set of resonant depths, and hence has measure zero.

Next fix $\delta \leq -\frac{1}{2}$. Then \mathcal{E}_δ coincides with the set

$$\mathcal{E} = \left\{ \mu_0 > 0 \mid \exists a > 0 \text{ such that } \forall p \geq 2, \lambda_p(\mu_0) \geq a \right\}. \quad (\text{S3.11})$$

Both inclusions $\mathcal{E}_\delta \subset \mathcal{E}$ and $\mathcal{E} \subset \mathcal{E}_\delta$ follow from reducing a to 1 if necessary and noting that $\min(a, p^{-\frac{1}{2}-\delta}) = a$ for $p \geq 2$. We claim that \mathcal{E} is the empty set. Suppose \mathcal{E} is not empty and $\mu_0 \in \mathcal{E}$. Then there is an $a > 0$ such that

$$|p - j^2 \tanh \mu_0| \geq a \tanh \mu_0 - p [1 - \tanh(p\mu_0)], \quad (p \geq 2, j \in p + 2\mathbb{Z}). \quad (\text{S3.12})$$

Since $0 < (1 - \tanh x) \leq 2e^{-2x}$ for $x > 0$, there is a $p_* \geq 2$ such that

$$|p - j^2 \tanh \mu_0| \geq \frac{a}{2} \tanh \mu_0, \quad (p \geq p_*, j \in p + 2\mathbb{Z}). \quad (\text{S3.13})$$

If $\tanh \mu_0 = m/d$ is rational, then setting $j = 2p_*d$ and $p = 4p_*^2md$ causes the left-hand side to be zero, a contradiction. (The factors of 2 and 4 ensure that $j \in p + 2\mathbb{Z}$.) Now suppose $\tanh \mu_0$ is irrational. We first observe that if j is large enough that $j^2 \tanh \mu_0 \geq p_*$, then we can round $j^2 \tanh \mu_0$ down or up to obtain an integer $p \geq p_*$ with the same parity as j and such that the left-hand side of (S3.13) is less than or equal to 1. This implies that $\frac{a}{2} \tanh \mu_0 \leq 1$. We know from Weyl's equidistribution theorem [45] that $m^2 \tanh \mu_0$ is equidistributed on the unit interval modulo 1, so there exists an m large enough that $4m^2 \tanh \mu_0 \geq (p_* + 1)$ holds, and such that $m^2 \tanh \mu_0$ modulo 1 lies in the interval $(0, \frac{a}{8} \tanh \mu_0)$. This implies there is an integer l such that $|l - m^2 \tanh \mu_0| < \frac{a}{8} \tanh \mu_0$. Multiplying by 4 and setting $(p, j) = (4l, 2m)$, we obtain p and j of the same parity such that $|p - j^2 \tanh \mu_0| < \frac{a}{2} \tanh \mu_0$, which contradicts (S3.13) once we confirm that $p \geq p_*$. For this, we use $p - j^2 \tanh \mu_0 > -\frac{a}{2} \tanh \mu_0 \geq -1$, which gives $p > 4m^2 \tanh \mu_0 - 1 \geq p_*$, as required.

Now suppose $\delta \leq 0$. We claim that \mathcal{E}_δ has measure zero. We already proved that \mathcal{E}_δ is empty for $\delta \leq -\frac{1}{2}$, so suppose $-\frac{1}{2} < \delta \leq 0$. Let $\theta = -[\delta - (-\frac{1}{2})] = -\frac{1}{2} - \delta$, which satisfies $-\frac{1}{2} \leq \theta < 0$. Let x_1 and x_2 satisfy $0 < x_1 < x_2 < 1$ and suppose $\mu_0 \in \mathcal{E}_\delta \cap \tanh^{-1}([x_1, x_2])$. Then there is an $a > 0$ such that

$$|p - j^2 \tanh \mu_0| \geq \min(a, p^\theta) \tanh \mu_0 - p[1 - \tanh(p\mu_0)], \quad (p \geq 2, j \in p + 2\mathbb{Z}). \quad (\text{S3.14})$$

Since $\theta < 0$, there is a p_* such that $\min(a, p^\theta) = p^\theta$ for $p \geq p_*$. We can increase p_* if necessary so that $p^{1-\theta}[1 - \tanh(p\mu_0)] < \frac{1}{2} \tanh \mu_0$ for $p \geq p_*$. Thus,

$$|p - j^2 \tanh \mu_0| > \frac{1}{2} p^\theta \tanh \mu_0 \geq \frac{x_1}{2} p^\theta, \quad (p \geq p_*, j \in p + 2\mathbb{Z}). \quad (\text{S3.15})$$

We will use this inequality to show that $\tanh \mu_0$ belongs to a set of measure zero. Let $C = (2x_2)^\theta x_1$ and $C_1 = \frac{1}{4} 2^{2\theta} C$. Since $-\frac{1}{2} \leq \theta < 0$ and $0 < x_1 < x_2 < 1$, we have $0 < C_1 < C < 2^\theta x_1^{1+\theta} < 1$. Schmidt [44] proved that for almost every $x \in \mathbb{R}$, the number $N(M, x)$ of integers m in the range $1 \leq m \leq M$ for which there exists an integer l satisfying $|m^2 x - l| \leq \frac{1}{2} C_1 m^{2\theta}$ satisfies $N(M, x) = \Psi(M) + O(\Psi(M)^{2/3})$ as $M \rightarrow \infty$, where $\Psi(M) = \sum_{m=1}^M C_1 m^{2\theta}$. The intervals $I_m = [-\frac{1}{2} C_1 m^{2\theta}, \frac{1}{2} C_1 m^{2\theta}]$ are required to be nested ($I_m \supset I_{m+1}$) as m increases, which is true here since $\theta < 0$. We see that $\lim_{M \rightarrow \infty} \Psi(M) = \infty$ since $C_1 > 0$ and $-1 \leq 2\theta < 0$. We conclude from Schmidt's theorem that the following set has full Lebesgue measure

$$\mathcal{G}_{\theta, C_1} = \left\{ x \in \mathbb{R} \mid \exists \text{ infinitely many pairs } (l, m) \in \mathbb{Z} \times \mathbb{N} \text{ s.t. } |m^2 x - l| \leq \frac{1}{2} C_1 m^{2\theta} \right\}. \quad (\text{S3.16})$$

Freezing x_1, x_2 and the corresponding C and C_1 , the set $\mathcal{G} = \mathcal{G}_{\theta, C_1} \cap [x_1, x_2]$ has full measure $x_2 - x_1$. If $x \in \mathcal{G}$, there is a sequence $\{(l_i, m_i)\}_{i=1}^\infty$ such that $|m_i^2 x - l_i| \leq \frac{1}{2} C_1 m_i^{2\theta}$ and $m_{i+1} > m_i$ for $i \geq 1$. Multiplying by 4 and setting $(p_i, j_i) = (4l_i, 2m_i)$, we find that p_i and j_i have the same parity and $|j_i^2 x - p_i| \leq 2C_1 m_i^{2\theta} = \frac{1}{2} C j_i^{2\theta}$. Since $C < 1$, $\theta < 0$ and $j_i \geq 1$,

$$-\frac{1}{2} \leq p_i - j_i^2 x \leq \frac{1}{2}, \quad (i \geq 1). \quad (\text{S3.17})$$

Choose i_* large enough that $j_i^2 x_1 > \frac{1}{2}$ for $i > i_*$. Then

$$0 < j_i^2 x_1 - \frac{1}{2} \leq p_i \leq j_i^2 x_2 + \frac{1}{2} < 2j_i^2 x_2, \quad (i \geq i_*). \quad (\text{S3.18})$$

For $i > i_*$, we have $j_i^2 > p_i / (2x_2) > 0$, so

$$|p_i - j_i^2 x| \leq \frac{1}{2} C (j_i^2)^\theta < \frac{1}{2} C \left(\frac{p_i}{2x_2} \right)^\theta = \frac{x_1}{2} p_i^\theta, \quad (i > i_*). \quad (\text{S3.19})$$

Since there are infinitely many pairs (p_i, j_i) with the same parity satisfying (S3.19), $\tanh \mu_0$ satisfying (S3.15) does not belong to \mathcal{G} . This shows that

$$\mathcal{E}_\delta \cap \tanh^{-1}([x_1, x_2]) \subset \tanh^{-1}([x_1, x_2] \setminus \mathcal{G}). \quad (\text{S3.20})$$

Since $[x_1, x_2] \setminus \mathcal{G}$ has measure zero and $\tanh^{-1}(x)$ is monotonic and absolutely continuous on the compact interval $[x_1, x_2]$, Theorem 7.18 of [43] ensures that the right-hand side of (S3.20) has measure zero. Since $[x_1, x_2]$ was an arbitrary subinterval of $(0, 1)$, we conclude that \mathcal{E}_δ has measure zero.

Finally, we claim that if $\delta > \frac{1}{2}$ and $\mu_0 > 0$ is rational, say $\mu_0 = m/d$ with $m, d \in \mathbb{N}$, then $\mu_0 \in \mathcal{E}_\delta$. Lambert's continued fraction [46] is $\tanh(\mu_0) = \frac{m}{d} + \frac{m^2}{3d} + \frac{m^2}{5d} + \frac{m^2}{7d} + \dots$. Theorem 4.1 of [47] implies that $\tanh \mu_0$ has irrationality exponent 2. This means that for any $\beta > 2$, there exists a constant $C > 0$ such that $|\tanh \mu_0 - \frac{p}{q}| \geq Cq^{-\beta}$ for all $(p, q) \in \mathbb{N}^2$. Let $\delta' = \frac{1}{2}(\frac{1}{2} + \delta)$, which satisfies $\frac{1}{2} < \delta' < \delta$. We set $\beta = \frac{3}{2} + \delta' > 2$ to obtain C . Specializing to $q = j^2$ then gives

$$|j^2 \tanh \mu_0 - p| \geq \frac{C}{j^{1+2\delta'}}, \quad (p, j \in \mathbb{N}). \quad (\text{S3.21})$$

If μ_0 were not in \mathcal{E}_δ , then since it is also non-resonant by Lemma 3.1, we could construct a sequence $\{(p_i, j_i)\}_{i=1}^\infty$ satisfying (S3.3)–(S3.7). From (S3.6) and (S3.7), we have

$$|j_i^2 \tanh \mu_0 - p_i| < \left(\frac{2}{3} j_i^2 \tanh \mu_0 \right)^{-\frac{1}{2}-\delta} \leq \frac{C}{j_i^{1+2\delta'}}, \quad (i \geq i_*), \quad (\text{S3.22})$$

where we increased i_* if necessary so that $(\frac{2}{3} \tanh \mu_0)^{-\frac{1}{2}-\delta} j_i^{2(\delta'-\delta)} \leq C$ for $i \geq i_*$. This contradicts (S3.21), so $\mu_0 \in \mathcal{E}_\delta$ as claimed.

We performed a numerical experiment to see how slowly finite-depth small divisors approach zero in practice. We set $\mu_0 = 1/16$ since there were no jumps in ρ_v^{-1} in figure 4 for that case. Panel (a) of Figure 12 shows the first 24 pairs (p, λ_p) for which $\lambda_p < (\min_{2 \leq q \leq p-1} \lambda_q)$. We find that $\lambda_p \geq \lambda_2$ for $2 \leq p \leq 24773$. It is difficult to imagine a code ever being implemented that could reach $p = 24774$. While Theorem 3.1 only guarantees that $\mu_0 = 1/16$ belongs to \mathcal{E}_δ for $\delta > 1/2$ (by virtue of being rational), it appears to belong to $\mathcal{E}_{0.07}$, using $a = 0.0155$ in the definition (3.12) to capture the first point λ_2 . Decreasing δ much further would require reducing a . The first divisor $\lambda_{p,j}$ smaller than 10^{-5} in magnitude is $p = 714638949293$ and $j = 3383653$, and the first below 10^{-11} is $p \approx 2.504 \times 10^{22}$ and $j \approx 6.333 \times 10^{11}$, with precise values given as subscripts in the figure. We checked all possibilities with $1 \leq j \leq 10^{12}$, which covers $2 \leq p \leq 6.24 \times 10^{22}$. This confirms that the sets \mathcal{E}_δ in Theorem 3.1 are well-suited to describe what actually happens in practice.

Next we discuss large divisors and the spacing between potentially small divisors. Panel (b) of Figure 12 shows that λ_p is obtained by sampling two sawtooth-shaped curves with progressively larger “teeth.” The blue curve is $g_e(x) = \min_{j \in 2\mathbb{Z}} |f(x) - j^2|$ and the

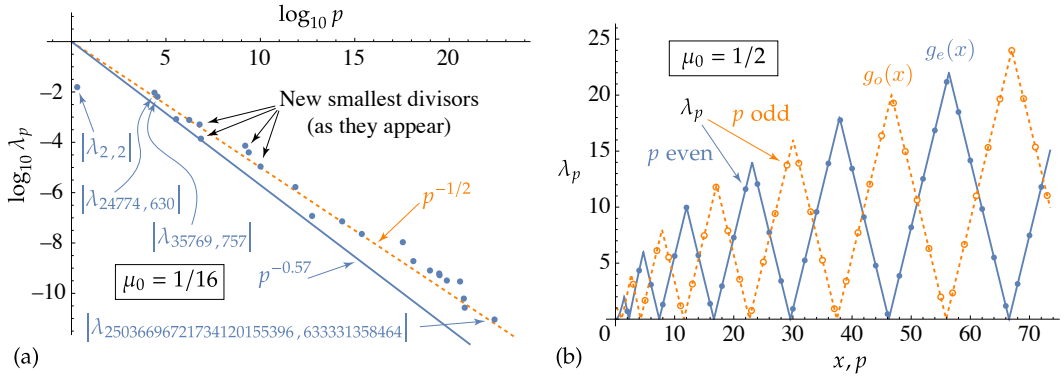


Fig. 12 Behavior of $\lambda_p = |\lambda_{p,j}|$ for $\mu_0 = 1/16$ and $\mu_0 = 1/2$. (a) On the rare occasion that a new smallest divisor enters the recurrence, it does so near the line $p^{-1/2}$ (orange dashed line). It appears that $\mu_0 = 1/16$ belongs to \mathcal{E}_δ with $a = \lambda_2 = 0.0155$ and $\delta = 0.07$ in Theorem 3.1, which corresponds to the blue line $p^{-0.57}$ on this log-log plot. (b) Each λ_p lies on a sawtooth-shaped curve, one for p even (blue lines) and the other for p odd (orange dashed lines).

dashed orange curve is $g_o(x) = \min_{j \in 2\mathbb{Z}+1} |f(x) - j^2|$, where $f(x) = x \frac{\tanh(x\mu_0)}{\tanh(\mu_0)}$. Here $x \geq 0$ is a continuous variable and

$$\lambda_p = g_e(p), \quad p \in \{2, 4, 6, \dots\}, \quad \lambda_p = g_o(p), \quad p \in \{3, 5, 7, \dots\}. \quad (\text{S3.23})$$

We plotted the case of $\mu_0 = 1/2$ (instead of $1/16$) to reduce the oscillation frequency of $g_e(x)$ and $g_o(x)$ and show more sampled values of (p, λ_p) on each monotonic segment of these functions. Theorem S3.3 below confirms the idea that λ_p can only be small for p near the zeros of $g_e(x)$ or $g_o(x)$, which are close to the centers of the intervals I_j that parameterize the V-shaped troughs of these curves. If p is close enough to a zero of one of the curves that $\lambda_p \leq \coth(\mu_0)$, we will show that the next opportunity for this to happen again is near a zero of the other curve. The spacing between these zeros grows linearly with the index j , as does the height of the j^{th} peak of $g_e(x)$ or $g_o(x)$. Since a zero of one curve is close to the peak of the other, there will be many large values of λ_q for q near p of the opposite parity. We will show that if a small divisor excites growth in the Stokes coefficients of mode (p, j) , there will be large divisors suppressing growth in modes (q, k) with $k \neq j$ or $q \neq p$ of the form $q = p \pm l$ for $l = \{1, 3, 5, \dots, l_{\max}\}$, where $l_{\max} \approx j \tanh(\mu_0)$. As an extreme example, when $\mu_0 = 1/16$, the smallest value of λ_p that occurs in the range $2 \leq p \leq 6.24 \times 10^{22}$ is 9.13×10^{-12} , where $p \in I_j$ with $j = 633\,331\,358\,464$. The two nearest neighbors have $\lambda_{p \pm 1} \geq 1.267 \times 10^{12}$ and each odd q satisfying $|q - p| \leq 3.95 \times 10^{10}$ yields $\lambda_q \geq 6.33 \times 10^{11}$. We note that $\lambda_q \lambda_p \geq 5.78$ for each of these q 's, so the large divisors suppress modes (q, k) more strongly than the small divisor amplifies mode (p, j) .

Before stating the theorem, we need to establish notation. Let $\{x_j^e\}_{j=0}^\infty$ and $\{x_j^o\}_{j=0}^\infty$ denote the location of successive peaks and zeros of $g_e(x)$ and $g_o(x)$, respectively. At $x_0^e = x_0^o = 0$, $g_o(x)$ has a peak while $g_e(x)$ has a zero. Since $f(1) = 1$, $g_o(x)$ has a zero at $x_1^o = 1$. Let $\mathbb{N}_o = \{1, 3, 5, \dots\}$, $\mathbb{N}_e = \{2, 4, 6, \dots\}$, $I_j = (x_{j-1}^o, x_{j+1}^o]$ for $j \in \mathbb{N}_o$ and $I_j = (x_{j-1}^e, x_{j+1}^e]$ for $j \in \mathbb{N}_e$. Let $*$ denote the symbol e or o and let $j \in \mathbb{N}_*$. Then $g_*(x) = |f(x) - j^2|$ for $x \in I_j$. In our enumeration of peaks and zeros, x_j^* is the zero of $g_*(x)$ in I_j and x_{j+1}^* is the peak at the right endpoint of I_j . So $x = x_j^*$ is the solution of $f(x) = j^2$ while $x = x_{j+1}^*$ is the solution of $f(x) - j^2 = (j+2)^2 - f(x)$, i.e., $f(x) = [(j+1)^2 + 1]$. The

value of $g_*(x)$ at $x = x_{j+1}^*$ is $2j + 2$. Between a zero and peak of one curve is a peak and zero of the other, $\{f(x_j^*), f(x_j^\dagger), f(x_{j+1}^\dagger), f(x_{j+1}^*)\} = \{j^2, j^2 + 1, (j+1)^2, (j+1)^2 + 1\}$, where $\dagger \in \{e, o\}$ and $\dagger \neq *$. The order of the points is then $\{x_1^o, x_1^e, x_2^o, x_2^e, x_3^o, x_3^e, x_4^o, x_4^e, \dots\} = f^{-1}(\{1, 2, 4, 5, 9, 10, 16, 17, \dots\})$. Since $f(x)$ is an increasing bijection of $[0, \infty)$ to $[0, \infty)$, so is $f^{-1}(y)$. For $* \in \{e, o\}$ and $j \in \mathbb{N}_*$, we define $\mathcal{P}_j = \{p \in \mathbb{N}_* : p \geq 2, p \in I_j\}$ so that $\lambda_p = |\lambda_{p,j}|$ for $p \in \mathcal{P}_j$. For each $p \geq 2$ there is precisely one j such that $p \in \mathcal{P}_j$. This is because $\cup_{j \in \mathbb{N}_o} I_j = (0, \infty)$ and $\cup_{j \in \mathbb{N}_e} I_j = (x_1^e, \infty)$. The only question is whether $x_1^e < 2$, which follows from $2 < f(2)$. (We showed that $p < f(p) < p^2$ for $p \geq 2$ in section 3.1.) Since $x_1^e > x_1^o = 1$, $\mathcal{P}_j = \mathbb{N}_* \cap I_j$ when $j \geq 2$.

Lemma S3.1 *If $x\mu_0 > 1$ then $f'(x) > \coth(\mu_0)$.*

Proof Use $\tanh(x\mu_0) > [1 - \operatorname{sech}^2(x\mu_0)]$ in $f'(x) = \frac{\tanh(x\mu_0) + x\mu_0 \operatorname{sech}^2(x\mu_0)}{\tanh(\mu_0)}$.

Lemma S3.2 *Suppose $M > 0$ is large enough that $0 < u(1 - \tanh u) < \frac{1}{3}\mu_0$ for all real $u \geq M$. Then if $y \geq \frac{M}{\mu_0 \tanh \mu_0}$ and $x = f^{-1}(y)$, there exists $\theta \in (0, \frac{1}{3})$ such that $x = y \tanh(\mu_0) + \theta$.*

Proof We know $x = f^{-1}(y)$ exists and $x > 0$. Since $\tanh(x\mu_0) < 1$ and $x \frac{\tanh(x\mu_0)}{\tanh \mu_0} = y$, we have $x > y \tanh(\mu_0) \geq M/\mu_0$. So $u = x\mu_0 \geq M$ and $\theta = \frac{u(1 - \tanh u)}{\mu_0} \in (0, \frac{1}{3})$. Finally, $y = f(x) = x \frac{1 - (1 - \tanh(x\mu_0))}{\tanh \mu_0} = \frac{x - \theta}{\tanh \mu_0}$.

Theorem S3.1 *Let $M = \max(6, \log(\frac{36}{\mu_0}) - 6)$ and suppose $j \in \mathbb{N}$ with $j \geq (\sqrt{M} \coth(\mu_0) + 1)$. Then there is at most one $p \in \mathcal{P}_j$ with $\lambda_p \leq \coth(\mu_0)$. If $p \in \mathcal{P}_j$ with $\lambda_p \leq \coth(\mu_0)$ and $q \neq p$ is an integer satisfying $|q - p| \leq [(j - 1) \tanh(\mu_0) - \frac{4}{3}]$, then $q \geq 2$ and $\lambda_q > \coth(\mu_0)$. If, additionally, $q - p$ is odd, then $\lambda_q > j$. If k has the same parity as p and $k \neq j$, then $|\lambda_{p,k}| > \frac{8}{3}j$.*

Proof First we check that M satisfies the hypotheses of lemma S3.2. Since $0 < u(1 - \tanh u) = \frac{2u}{e^{2u} + 1} < 2ue^{-2u}$, it suffices to show that $2ue^{-2u} \leq \frac{1}{3}\mu_0$ for $u \geq M$. Since $u \geq M \geq 6$, we have $u \leq 6e^{u-6}$ and $2ue^{-2u} \leq 12e^{-(u+6)} \leq 12e^{-(M+6)} \leq \frac{1}{3}\mu_0$.

We observe here that if $\mu_0 \geq 36e^{-12} = 2.21 \times 10^{-4}$ then $M = 6$, which covers typical fluid depths. Since $\tanh(\mu_0) < \mu_0$, the condition on j ensures that $(j - 1)^2 \geq M \coth^2(\mu_0) > \frac{M}{\mu_0 \tanh \mu_0}$. Since j is an integer and $j \geq (\sqrt{6} \coth(\mu_0) + 1) > (\sqrt{6} + 1) \approx 3.45$, we also have $j \geq 4$.

Let $*$ in $\{e, o\}$ denote the parity of j . Since $j \geq 4 \geq 2$, $\mathcal{P}_j = \mathbb{N}_* \cap I_j$ and the endpoints of I_j satisfy $x_{j\pm 1}^* = [(j \pm 1)^2 + 1]$. For each $x \in I_j$, $y = f(x) \geq f(x_{j-1}^*) = [(j - 1)^2 + 1] > \frac{M}{\mu_0 \tanh \mu_0}$. By lemmas S3.2 and S3.1, $x\mu_0 = \mu_0(y \tanh \mu_0 + \theta) > M > 1$ and $f'(x) > \coth \mu_0$. By the mean value theorem, for any $p, q \in \mathcal{P}_j$ we have $\lambda_p + \lambda_q = |f(p) - j^2| + |f(q) - j^2| \geq |f(p) - f(q)| = |f'(r)(p - q)| > |p - q| \coth(\mu_0)$, where r is a real number between p and q . Since $p, q \in \mathbb{N}_*$, $|p - q| \geq 2$. Choosing $p \in \mathcal{P}_j$ to minimize λ_p and assuming $\lambda_q \leq \coth(\mu_0)$ with $q \neq p$ forces $\lambda_p + \lambda_q \leq 2 \coth(\mu_0)$, a contradiction.

Suppose $p \in \mathcal{P}_j$ with $\lambda_p \leq \coth(\mu_0)$. Let $\dagger \in \{e, o\}$ with $\dagger \neq *$. Recall that x_j^* is the zero of $g_*(x)$ on I_j and $x_{j\pm 1}^\dagger$ are the adjacent zeros of $g_\dagger(x)$, so $f(\{x_j^*, x_{j\pm 1}^\dagger\}) = \{j^2, (j \pm 1)^2\}$. Since $\lambda_p = |f(p) - j^2| \leq \coth(\mu_0)$, we know $f(p) \geq y_1 := (j^2 - \coth \mu_0) > (j - 1)^2$,

where we used $\coth(\mu_0) < (2j-1)$ in the last inequality, which follows from $(j-1) \geq \sqrt{M} \coth(\mu_0)$. Since $(j-1)^2 \geq \frac{M}{\mu_0 \tanh \mu_0}$, there exist $\theta_1, \theta_{j-1}^+ \in (0, \frac{1}{3})$ such that

$$x_1 = f^{-1}(y_1) = j^2 \tanh(\mu_0) - 1 + \theta_1, \quad x_{j-1}^+ = (j-1)^2 \tanh(\mu_0) + \theta_{j-1}^+. \quad (\text{S3.24})$$

Since $f^{-1}(y)$ is monotonic, $p \geq x_1$. Thus, $p - x_{j-1}^+ \geq x_1 - x_{j-1}^+ > [(2j-1) \tanh(\mu_0) - \frac{4}{3}]$. Since $|q-p| \leq [(j-1) \tanh(\mu_0) - \frac{4}{3}]$, we conclude that $q - x_{j-1}^+ > j \tanh(\mu_0)$. The mean value theorem then gives $f(q) - (j-1)^2 = f'(r)(q - x_{j-1}^+) > j$, where r is between x_{j-1}^+ and q . Similarly, $\lambda_p \leq \coth(\mu_0)$ gives $f(p) \leq y_2 := (j^2 + \coth \mu_0)$, so $p \leq x_2 = f^{-1}(y_2)$ and

$$x_{j+1}^+ - p \geq x_{j+1}^+ - x_2 = [(j+1)^2 - j^2] \tanh(\mu_0) + \theta_{j+1}^+ - 1 - \theta_2 > (2j+1) \tanh(\mu_0) - \frac{4}{3}.$$

The bound on $|q-p|$ gives $x_{j+1}^+ - q > (j+2) \tanh(\mu_0)$. Applying the mean value theorem again gives $(j+1)^2 - f(q) > (j+2)$. We have shown that $(j-1)^2 + j < f(q) < (j+1)^2 - (j+2)$. Since $j \geq 4$, $f(1) = 1 < 13 < f(q)$, so $q \geq 2$. If $q \in \mathbb{N}_+$, $\lambda_q = g_+(q) = \min(f(q) - (j-1)^2, (j+1)^2 - f(q)) > \min(j, j+2) = j$. Otherwise, we use $(j-1)^2 + 1 < f(q) < (j+1)^2 + 1$ to conclude that $q \in \mathcal{P}_j = \mathbb{N}_* \cap I_j$, and therefore $\lambda_q > \coth(\mu_0)$.

Finally, if $k \in \mathbb{N}_*$ and $k \neq j$, then $\lambda_{p,k} = |f(p) - k^2| \geq |j^2 - k^2| - |f(p) - j^2|$. The first term is minimized by $k = j-2$, and $|f(p) - j^2| \leq \coth(\mu_0) \leq M^{-1/2}(j-1) \leq 6^{-1/2}(j-1)$. Using $j \geq 4$ and $M \geq 6$, we have $\lambda_{p,k} \geq (4j-4) - 6^{-1/2}(j-1) \geq (4 - 6^{-1/2})\frac{3}{4}j > \frac{8}{3}j$.

54. Derivation of the ODEs governing the Stokes coefficients

In this section we briefly derive the equations of motion for the Stokes expansion coefficients (2.15) from the governing equations (2.19)–(2.21) of the spatial Fourier modes. Using (2.15) to expand the algebraic equation (2.19) in powers of ϵ , we obtain

$$\beta_{p,n} + p\gamma_{p,n} + T_{p,n}^2 = 0, \quad (p \in \mathbb{N}, n \in \mathbb{N} \cup \{0\}), \quad (\text{S4.1})$$

$$\begin{aligned} T_{p,n}^2 = \cosh(p\mu_0) & \left(\sum_{q=1}^{p-1} \sum_{k=0}^n \frac{q}{2 \cosh(q\mu_0) \cosh[(p-q)\mu_0]} \alpha_{q,k} \beta_{p-q,n-k} \right. \\ & + \sum_{q=1}^n \sum_{k=0}^{n-q} \frac{q}{2 \cosh(q\mu_0) \cosh[(p+q)\mu_0]} \alpha_{q,k} \beta_{p+q,n-q-k} \\ & \left. - \sum_{q=1}^n \sum_{k=0}^{n-q} \frac{p+q}{2 \cosh(q\mu_0) \cosh[(p+q)\mu_0]} \alpha_{p+q,k} \beta_{q,n-q-k} \right). \end{aligned} \quad (\text{S4.2})$$

We match the notation $T_{p,n}^2$ introduced by Amick and Toland [16] for the analogous forcing term in the infinite-depth case. To avoid listing special cases, empty sums are always taken

to mean zero. Equation (2.20a) gives differential equations for the $\dot{\mu}_n$, namely

$$\begin{aligned} \dot{\mu}_n + T_{0,n}^1 &= 0, & (n \in \mathbb{N} \cup \{0\}), \\ T_{0,n}^1 &= \sum_{q=1}^n \sum_{k=0}^{n-q} \sum_{l=0}^{n-q-k} \frac{q}{2 \cosh^2(q\mu_0)} \alpha_{q,k} \dot{\alpha}_{q,l} S_{2q,n-q-k-l} \\ &+ \sum_{q=1}^n \sum_{k=0}^{n-q} \sum_{l=0}^{n-q-k} \sum_{m=0}^{n-q-k-l} \frac{q^2}{2 \cosh^2(q\mu_0)} \alpha_{q,k} \alpha_{q,l} \dot{\mu}_m C_{2q,n-q-k-l-m}. \end{aligned} \quad (\text{S4.3})$$

There is no analogous forcing term $T_{0,n}^1$ in the infinite-depth case, but Amick and Toland only defined $T_{p,n}^r$ for $r \in \{2, 3, 4\}$, so we make use of the omitted $r = 1$ index. We note that

$$T_{0,0}^1 = 0 \quad \Rightarrow \quad \dot{\mu}_0 = 0, \quad (\text{S4.4})$$

consistent with $\mu_0 L / 2\pi$ being the depth of the bottom boundary in physical space, which remains stationary as the standing wave evolves in time. Finally, (2.20b) gives the differential equation

$$\dot{\alpha}_{p,n} - p\gamma_{p,n} + T_{p,n}^3 = 0, \quad (p \in \mathbb{N}, n \in \mathbb{N} \cup \{0\}), \quad (\text{S4.5})$$

$$\begin{aligned} T_{p,n}^3 &= \frac{1}{s_{p,0}} \left[\sum_{q=0}^{n-1} (\dot{\alpha}_{p,q} - p\gamma_{p,q}) s_{p,n-q} + 2p \sum_{q=0}^{n-1} \sum_{k=1}^{n-q} \alpha_{p,q} \dot{\mu}_k c_{p,n-q-k} \right. \\ &+ \cosh(p\mu_0) \left(- \sum_{q=1}^{p-1} \sum_{k=0}^n \sum_{l=0}^{n-k} \frac{(p-q) \alpha_{p-q,k} \dot{\alpha}_{q,l} S_{p-2q,n-k-l}}{2 \cosh[(p-q)\mu_0] \cosh(q\mu_0)} \right. \\ &+ \sum_{q=1}^n \sum_{k=0}^{n-q} \sum_{l=0}^{n-q-k} \frac{[(p+q) \alpha_{p+q,k} \dot{\alpha}_{q,l} + q \alpha_{q,k} \dot{\alpha}_{p+q,l}] S_{p+2q,n-q-k-l}}{2 \cosh(q\mu_0) \cosh((p+q)\mu_0)} \\ &+ \sum_{q=1}^{p-1} \sum_{k=0}^{n-1} \sum_{l=0}^{n-k-1} \sum_{m=1}^{n-k-l} \frac{(p-q) q \alpha_{p-q,k} \alpha_{q,l} \dot{\mu}_m C_{p-2q,n-k-l-m}}{2 \cosh[(p-q)\mu_0] \cosh(q\mu_0)} \\ &\left. \left. + \sum_{q=1}^{n-1} \sum_{k=0}^{n-q-1} \sum_{l=0}^{n-q-k-1} \sum_{m=1}^{n-q-k-l} \frac{q(p+q) \alpha_{q,k} \alpha_{p+q,l} \dot{\mu}_m C_{p+2q,n-q-k-l-m}}{\cosh(q\mu_0) \cosh[(p+q)\mu_0]} \right) \right], \end{aligned} \quad (\text{S4.6})$$

while (2.21) gives

$$\dot{\gamma}_{p,n} + \sigma_0 \tanh(p\mu_0) \alpha_{p,n} + T_{p,n}^4 = 0, \quad \left(p \in \mathbb{N}, n \in \mathbb{N} \cup \{0\} \right), \quad (\text{S4.7})$$

$$\begin{aligned} T_{p,n}^4 = & \frac{1}{c_{p,0}} \left[\sum_{q=0}^{n-1} \dot{\gamma}_{p,q} c_{p,n-q} + \sum_{q=0}^{n-1} \sum_{k=0}^{n-q} \alpha_{p,q} \sigma_k s_{p,n-q-k} \right. \\ & + \cosh(p\mu_0) \left(\sum_{q=1}^n \sum_{k=0}^{n-q} \sum_{l=0}^{n-q-k} \frac{\beta_{q,k} \beta_{p+q,l} c_{p+2q,n-q-k-l}}{2 \cosh(q\mu_0) \cosh[(p+q)\mu_0]} \right. \\ & - \sum_{q=1}^{p-1} \sum_{k=0}^n \sum_{l=0}^{n-k} \frac{\beta_{p-q,k} \beta_{q,l} c_{p-2q,n-k-l}}{4 \cosh[(p-q)\mu_0] \cosh(q\mu_0)} \\ & - \sum_{q=1}^n \sum_{k=0}^{n-q} \sum_{l=0}^{n-q-k} \frac{(\beta_{p+q,k} \dot{\alpha}_{q,l} + \beta_{q,k} \dot{\alpha}_{p+q,l}) c_{p,n-q-k-l}}{2 \cosh(q\mu_0) \cosh[(p+q)\mu_0]} \\ & \left. \left. + \sum_{q=1}^{p-1} \sum_{k=0}^n \sum_{l=0}^{n-k} \frac{\beta_{p-q,k} \dot{\alpha}_{q,l} c_{p,n-k-l}}{2 \cosh[(p-q)\mu_0] \cosh(q\mu_0)} \right) \right]. \end{aligned} \quad (\text{S4.8})$$

S5. Computational aspects

In this section we examine the practical aspects of computing the Stokes coefficients in Fourier space efficiently on a parallel computer. We represent the functions $\mu_n(t)$, $\alpha_{p,n}(t)$, $\beta_{p,n}(t)$, $\gamma_{p,n}(t)$ and $B_{p,n}(t)$ through the real coefficients $(\mu_{n,j}, \alpha_{p,n,j}, \text{etc.})$ that appear in the trigonometric polynomial representations (3.1), (3.2), (3.4), (3.5) and (3.18). We reduce memory costs by only storing the Fourier modes that are present in the primed sums in those equations. We also do not store $c_{q,n,j}$ or $s_{q,n,j}$ in (3.19) since they equal $\frac{1}{2}(B_{q,m,j} \pm B_{-q,m,j})$, due to (2.25).

In the algorithm of section 3.2, summarized in figure 3, from the point that $\mu_N(t)$ has just been computed in the previous iteration to the point that $T_{0,N+1}^1(t)$ is evaluated in order to compute $\mu_{N+1}(t)$, the coefficients $B_{q,m,j}$ that will be needed by any of the $c_{q,m}(t)$ and $s_{q,m}(t)$ that appear in the formulas for the $T_{p,n}^r$ satisfy $0 \leq m \leq N$ and $|q| + 2m \leq 2N + 3$. Thus, immediately after $\mu_N(t)$ becomes known, we compute the new Bell polynomials $B_{q,m}(t)$ and $B_{-q,m}(t)$ with $(q, m) \in \{(1, N)\} \cup L_{2N+2}^\circ \cup L_{2N+3}^\circ$.

It is clear that the time complexity of the recursive algorithm is dominated by the computation of the forces $T_{p,n}^2$, $T_{p,n}^3$ and $T_{p,n}^4$ for $(p, n) \in L_\nu^\circ$ with $\nu \in \{2N+2, 2N+3\}$. Unlike the infinite-depth case in [16], our forces $T_{p,n}^3$ and $T_{p,n}^4$ are no longer quadratic functions of previously computed quantities $(\alpha_{j,k}, \dot{\alpha}_{j,k}, \beta_{j,k}, \text{etc.})$, but are now quartic and cubic, respectively. This is because of the conformal depth function $h(t)$ and the hyperbolic trigonometric functions it introduces. It may be possible to introduce additional auxiliary variables to accumulate intermediate pairwise products to reduce this complexity. We did not pursue this idea for the finite-depth case but succeeded with this strategy for the infinite-depth case with or without surface tension. These results will be reported elsewhere [18].

Although the triple and quadruple sums reduce the maximum order ν_{\max} that is feasible with available computational resources relative to the infinite-depth problem, we were able to compute the solution to very high order ($\nu_{\max} = 149$) by designing our code to run

on a supercomputer using a hybrid MPI/OpenMP framework [49] using MPFR [48] for multiple-precision arithmetic. Every sum appearing in the forces, regardless of the number of indices, is computed in parallel using MPI and OpenMP reductions. Each thread of each MPI task accumulates a partial sum of the terms it is responsible for. For example, the sum

$$\sum_{q=1}^{p-1} \sum_{k=0}^{n-1} \sum_{l=0}^{n-k-1} \sum_{m=1}^{n-k-l} \frac{(p-q)q\alpha_{p-q,k}\alpha_{q,l}\dot{\mu}_m c_{p-2q,n-k-l-m}}{2 \cosh[(p-q)\mu_0] \cosh(q\mu_0)} \quad (\text{S5.1})$$

appears in the formula (S4.6) for $T_{p,n}^3$. When a thread processes one of the terms of this sum, it computes the inverse FFTs of the temporal Fourier coefficients of each factor, namely

$$\alpha_{p-q,k,j}, \quad \alpha_{q,l,j}, \quad ij\mu_{m,j}, \quad B_{p-2q,n-k-l-m,j}, \quad B_{2q-p,n-k-l-m,j}, \quad (\text{S5.2})$$

to obtain values for $\alpha_{p-q,k}(t)$, $\alpha_{q,l}(t)$, $\dot{\mu}_m(t)$ and $B_{\pm(p-2q),n-k-l-m}(t)$ for $t \in [0, 2\pi]$ on a uniform grid $\mathcal{G}_M = \{2\pi j/M\}_{j=0}^{M-1}$, with enough grid points M to resolve $T_{p,n}^3(t)$ with no aliasing errors. Since $T_{p,n}^3(t)$ is a trigonometric polynomial of degree $p+2n$, the minimum grid size is $M_{\min} = 2(p+2n+1)$. We choose the smallest integer $M \geq M_{\min}$ of the form $M = 2^{m_2}3^{m_3}5^{m_5}$ with $m_2 \geq 1$, $m_3 \in \{0, 1\}$ and $m_5 \in \{0, 1\}$, which are grids for which the FFT and inverse FFT are particularly fast. The value of M increases as the computation progresses to higher orders $\nu = p+2n$. Examples include $M = 240$ for $\nu = 109$ and $M = 320$ for $\nu = 149$. We wrote a custom FFT library to work efficiently with the MPFR data type to avoid allocation of temporary variables as much as possible; otherwise it is a standard radix-2, 3 and 5 FFT algorithm, optimized as in [51]. We also wrote specialized MPI communication routines to send sequences of MPFR numbers using character strings for the mantissas (exported in base 32) and integers for the exponents.

Continuing with the example in (S5.1), the Fourier modes in (S5.2) are written into complex arrays of size $M/2+1$, indexed by $0 \leq j \leq M/2$. Each set of modes in (S5.2) fits in this array size without truncation, and is zero-padded to fill up the space. Multiplying $\mu_{m,j}$ by ij gives the Fourier coefficients of $\dot{\mu}_m(t)$. We use the c2r version [50] of the inverse FFT, which assumes negative-index Fourier modes are the complex conjugate of positive-index modes (without storing them) and returns real function values on the uniform grid \mathcal{G}_M . We then evaluate $c_{p-2q,n-k-l-m}$ from $B_{\pm(p-2q),n-k-l-m}$ on \mathcal{G}_M . All the factors in (S5.1) are now known on the uniform grid, and are multiplied together pointwise. Each thread of each MPI task is assigned a subset of the indices q, k, l and m in the sum (S5.1) and accumulates the partial sum over these indices. This is repeated for the other sums in the formula (S4.6) for $T_{p,n}^3(t)$. These results are combined with those of the other threads and nodes at the end via parallel reduction. Finally, a forward FFT is taken to convert from physical space back to Fourier space, where the solution of the ODEs for $\alpha_{p,n}(t)$, etc., is "read off" from the Fourier representations of the forces. Computing the time derivative $\dot{T}_{p,n}^3$ in (II*) is also easily performed in Fourier space. We compute the Bell polynomials through a similar procedure in which $B_{q,n}(t)$ is accumulated on a uniform grid in time via the recursion (2.26). Taking the FFT of the sum gives the Fourier coefficients $B_{q,n,j}$, which are the representation stored in memory.

Although it would be possible to process all the lattice points within L_{2N+2}° independently in parallel, followed by all the points in L_{2N+3}° , we elected to process the lattice points sequentially and parallelize the computation at the level of individual sums in the forces. This is simpler and leads to near-perfect load balancing without having to worry about how the number of terms in the sums in the forcing terms $T_{p,n}^r$ varies with p and n at a given level $p+2n = \nu$.

that nearly identical growth and plateau regions will occur. However, all errors reported in this paper are from a lower-precision calculation checked against an auxiliary higher-precision calculation.

To compute the continued fraction expansion coefficients in (4.14) and (4.15) for $\mu_0 = 1$, we use both the standard and progressive forms of the qd-algorithm [58] in 638-bit (192-digit) floating-point arithmetic and compare the results to each other to estimate the accuracy of d_n and $\tilde{d}_{19,n}$. The relative error between the two calculations is zero for d_0 and $\tilde{d}_{19,0}$ and grows from 10^{-192} for d_1 to 10^{-137} for d_{74} , and from 10^{-192} for $\tilde{d}_{19,1}$ to 10^{-135} for $\tilde{d}_{19,65}$. This observed loss of precision in the continued fraction coefficients is consistent with the condition numbers one encounters (namely 1.6×10^{54} for T and 7.7×10^{55} for $\hat{\phi}_{19}$) if one solves for the polynomial coefficients of $P(x)$ and $Q(x)$ directly from τ_0, \dots, τ_{74} or $\tilde{\tau}_{19,0}, \dots, \tilde{\tau}_{19,65}$ by computing the nullspace of a Toeplitz matrix [59]. The errors in τ_n and $\tilde{\tau}_{19,n}$ from computing the Stokes expansions in finite-precision arithmetic will also affect the accuracy of the continued fraction expansions. We repeated the entire calculation with 850 bits (256 digits) and find that the relative errors in d_n and $\tilde{d}_{19,n}$ for the 638-bit calculation are uniformly less than 10^{-119} , which is far smaller than the errors in the shooting method.

For the results of figure 11 in the $\mu_0 = 1/16$ case, we computed the Stokes expansion and its Padé approximants twice, once with 212 bits (64 digits) and once with 424 bits (128 digit). Using the latter calculation to measure error in the former shows that the maximum relative error in any pole or zero in figure 11 is bounded by 9.6×10^{-29} . Thus, the 212-bit calculation has enough accuracy to distinguish the pole z_p from the zero z_0 in the Froissart doublet labeled FD in panel (b) of the figure, which differ from each other by $|z_p - z_0|/|z_p| = 4.4 \times 10^{-21}$.

S7. Secondary standing waves and the nonlinear deformation of resonant modes

In this section we investigate the secondary standing waves that oscillate on top of the primary wave with different amplitudes and phases on different bifurcation branches. Such secondary waves have been reported previously for standing waves in finite depth [26, 27, 28, 29], three-dimensional standing waves [30], and gravity-capillary standing waves [29, 19]. Here we explore the effects of nonlinearity on the shapes of the secondary waves, which deviate from the sinusoidal patterns one would get from linearization about the flat rest state.

Figure 14 shows snapshots of the wave profile $\eta^{\text{graph}}(x, t)$ for solutions D, E and F from the $\mu_0 = 1$ bifurcation plots in figures 6–8 at the dimensionless times $t \in \mathcal{T}_6$ from (4.13). These three solutions have a common period, $T = 7.267295$, which is 9.4% larger than small-amplitude waves in the linear regime at this depth; see figure 7. Just like solutions ABC at depth $\mu_0 = 3/5$ in figure 5, the non-uniqueness of solutions with this period is due to 3 possible amplitudes of a secondary standing wave with characteristics of a nearby harmonic resonance that evolves on top of the primary wave. Solutions ABC are near the (5, 3) resonant depth (0.6232354) while solutions DEF are near the (7, 3) resonant depth (1.039719). We define the primary wave to be solution E . The secondary wave of solution F is in phase with solution E , which sharpens the crest at $t = 0$ and increases the crest-to-trough height, ϵ , relative to solution E . For solution D , the secondary wave is out of phase with solution E , causing a dimple to form at the wave crest at $t = 0$ and decreasing ϵ . These changes in ϵ are also evident in the bifurcation plot of figure 7. In figure 14, solutions D and F oscillate around solution E with 7 spatial oscillations that deviate visibly from being

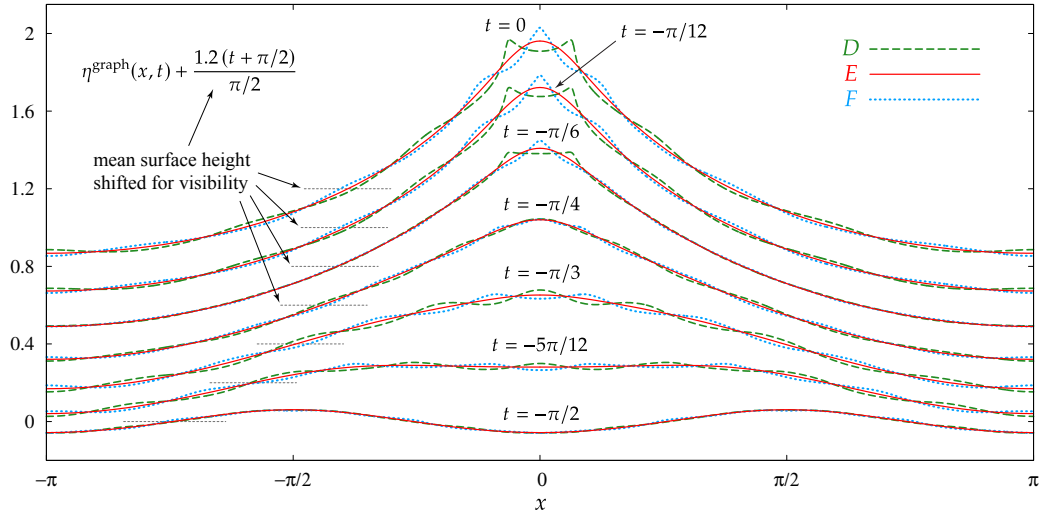


Fig. 14 Snapshots of the time-evolution of the unit-depth standing wave solutions D , E and F from the bifurcation plots in figures 6–8 at the times $t \in \mathcal{T}_6$. Vertical offsets were added to the wave profiles at successive times for visibility.

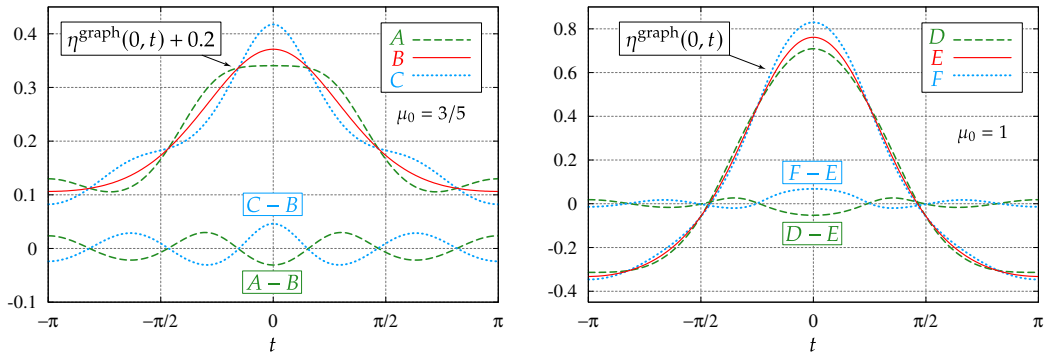


Fig. 15 Time-evolution of the wave profile above the symmetry point $x = 0$ over one period for the $\mu_0 = 3/5$ standing waves ABC from figure 5 (left) and the $\mu_0 = 1$ standing waves DEF from figures 6–8 and 14 (right). The curve labeled $A - B$ shows the difference $\eta_A^{\text{graph}}(0, t) - \eta_B^{\text{graph}}(0, t)$, with similar formulas for the other cases.

sinusoidal perturbations. The oscillations are largest near the wave crest at $x = 0$ when the wave reaches maximum amplitude at $t = 0$.

In Figure 15, we plot the time evolution of the wave profile at $x = 0$ over one cycle of the wave for solutions ABC from figure 5 (left) and solutions DEF from figures 6–8 and 14 (right). We also plot the perturbations required to move from B to A and B to C (left) and from E to D and E to F (right). These are specific perturbations from one standing wave solution of the fully nonlinear water wave equations to another, viewing solutions B and E as the primary waves and these perturbations as the secondary waves. We have not investigated the stability of solutions B and E to arbitrary perturbations [61, 62, 63]. In the left panel, a vertical offset of 0.2 was added to the wave profiles to separate them from the perturbation plots. In both panels, the secondary waves execute 3 cycles over one period of the composite wave. They deviate visibly from being sinusoidal perturbations, with non-

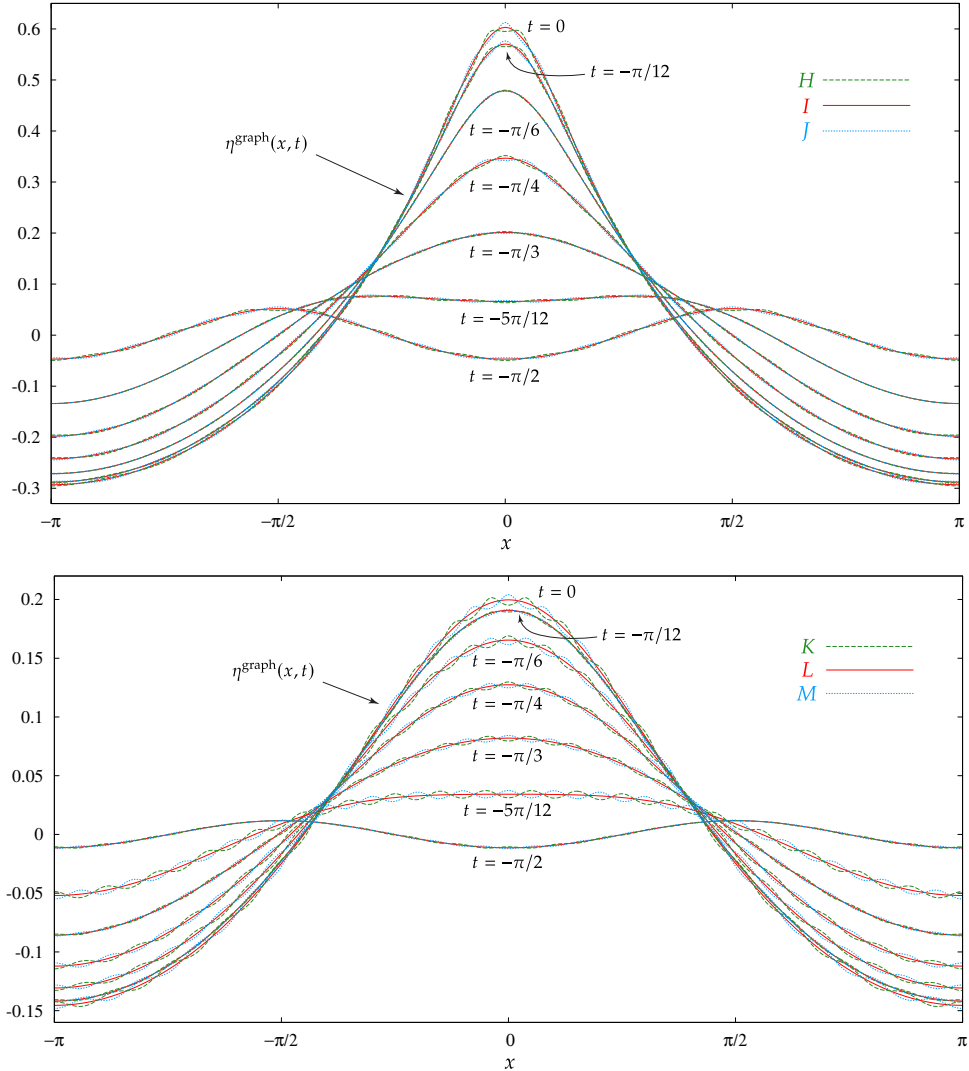


Fig. 16 Snapshots of the unit-depth standing waves labeled HIJ and KLM in figures 6–8 at times $t \in \mathcal{T}_6$.

uniform oscillations that grow largest near $t = 0$. This is especially true in the right panel due to nonlinear effects being stronger for larger-amplitude waves.

Figure 16 shows snapshots of the unit-depth standing waves HIJ and KLM from the bifurcation plots of figures 6–8 at times $t \in \mathcal{T}_6$, while figure 17 shows the time-evolution of the wave profiles above the symmetry point $x = 0$ over one period. The waves labeled HIJ have common period $T = 7.227964$ while the waves labeled KLM have common period $T = 7.195747$. Solutions H and J oscillate around solution I with 12 spatial oscillations and 4 temporal oscillations while solutions K and M oscillate around solution L with 19 spatial oscillations and 5 temporal oscillations. Combined with the results in figures 14 and 15, this confirms that these bifurcation branches correspond to the three approximate resonances $(p, j) \in \{(7, 3), (12, 4), (19, 5)\}$ in the cluster of small divisors for $\mu_0 = 1$ in figure 10. The secondary standing wave sharpens the wave crest at $t = 0$ for solutions J and M and leads

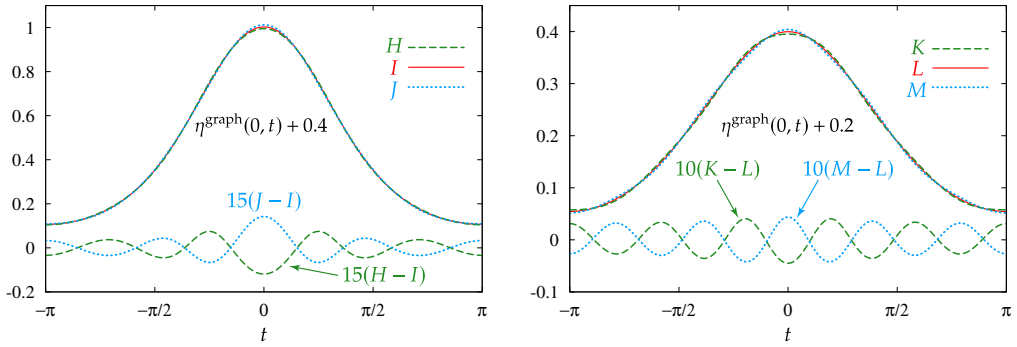


Fig. 17 Time-evolution of the unit-depth standing waves labeled HIJ and KLM evaluated at $x = 0$. The curve labeled $15(J - I)$ shows $15[\eta_j^{\text{graph}}(0, t) - \eta_i^{\text{graph}}(0, t)]$, with similar formulas for the other cases.

to dimples at the wave crest at $t = 0$ for solutions H and K . This also causes the crest-to-trough height ϵ in figure 7 to increase for solutions J and M relative to I and L , respectively, and to decrease for solutions H and K . In figure 17, we multiplied the perturbation plots by 15 (left) or 10 (right) to better see the deviation from sinusoidal behavior in the secondary standing waves. This deviation is more pronounced for solutions HIJ as they have larger amplitude than solutions KLM .

S8. A method of identifying harmonic resonances

After using numerical continuation to follow the DEF , HIJ and KLM bifurcation branches in figure 6, we noticed a persistent pole-zero pair in the Padé approximant of T in figure 7 near $\epsilon_* = 0.2738080600$. Although the pole and zero agree with each other to 24 leading digits for the 149th-order Padé approximant of T , it turns out to be an actual imperfect bifurcation rather than a spurious Froissart doublet [59]. Our goal in this section is to develop a method of identifying which harmonic resonance is responsible for such a bifurcation that has been located via Padé techniques. We wish to avoid relying on numerical continuation to extend the bifurcation branches far enough that the secondary waves become visible, as this is expensive.

We used the shooting method to compute 16 additional solutions at amplitudes $\epsilon_* \pm \delta_k$, where $\delta_k = 10^{-4.4433 - 0.4772k}$ for $0 \leq k \leq 7$. (This was an arbitrary choice with the feature that the distance to ϵ_* decreases geometrically as k increases.) These solutions had to be computed in quadruple-precision to see the effects of the bifurcation. We plotted the Fourier modes $\hat{\eta}_p$ (p even) and $\hat{\phi}_p$ (p odd) of the initial conditions (4.12) of the shooting method results as functions of ϵ for $1 \leq p \leq 50$ and found that $\hat{\eta}_{36}$ undergoes the largest jump when ϵ crosses ϵ_* . We then computed the 149th-order Padé approximant $\epsilon^{36}[28/28]_{\tilde{\tau}_{36}}(\epsilon^2)$ of $\hat{\eta}_{36}$ to see if it accurately predicts the shooting method results near this bifurcation. This is confirmed in panel (a) of figure 18, where all 16 values of $\hat{\eta}_{36}$ from the shooting method results lie on the Padé curve. (The errors, not shown, range from 3.5×10^{-28} at $\epsilon_* - \delta_0$ to 2.3×10^{-22} at $\epsilon_* + \delta_7$.) The four solutions closest to ϵ_* , with $\epsilon = \epsilon_* \pm \delta_k$, $k \in \{6, 7\}$, are labeled N , P , Q and R .

Rather than follow the side branches further by numerical continuation in order to directly observe the secondary waves, we make use of the fact that the Jacobian $J_{mk} = \partial r_m / \partial \theta_k$ from the shooting method is nearly singular near an imperfect bifurcation, where

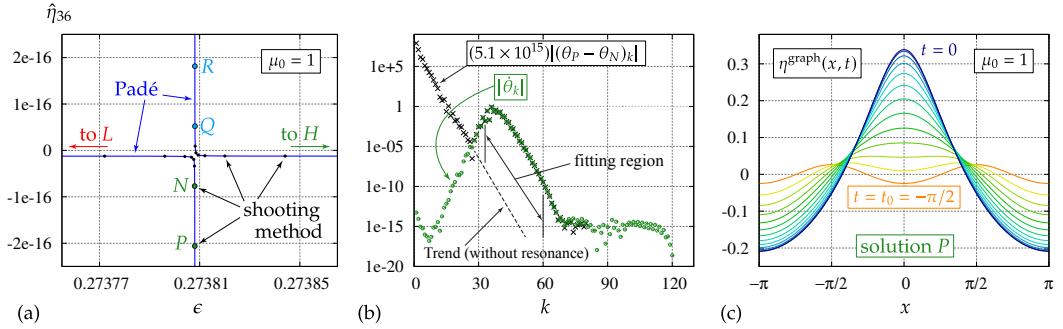


Fig. 18 An imperfect bifurcation near $\epsilon_* = 0.2738080600$ is predicted by a pole in the 149th-order Padé approximant of T . (a) We computed 16 shooting method solutions near this pole, which are the black markers and points labeled $NPQR$. (b) To identify the harmonic resonance responsible for the bifurcation, we computed the perturbation direction $\hat{\theta}$ corresponding to the right singular vector of the Jacobian at solution P with the smallest singular value and compared the high-frequency components of $(\theta_P - \theta_N)$ and $(\theta_R - \theta_Q)$ to those of $\hat{\theta}$. (c) Time-evolution of solution P for $t \in \mathcal{T}_{12}$.

r_m and θ_k were defined in (4.9) and (4.10). In this step, we drop T from the vector θ in (4.10) instead of one of the Fourier modes of the initial condition. This is the Jacobian in the variant of the algorithm where T is specified as the bifurcation parameter. At solution P , the smallest singular value of J is 3.4×10^{-9} . The second smallest is 2.3×10^{-6} and the largest is 1.395. The green circles in panel (b) of figure 18 show the magnitudes of the components of the singular vector corresponding to the smallest singular value. This is a right singular vector, which we denote by $\hat{\theta}$. Here we use a dot for a perturbation direction or a variational derivative with respect to this perturbation, not for a time derivative. The components of $\hat{\theta}$ are the Fourier modes of the initial conditions of the linearized water wave equations about solution P , given in [29], that minimize the norm of $\dot{r} = J\hat{\theta}$, subject to the constraint $\|\hat{\theta}\| = 1$. The corresponding linearized solution about solution P is denoted $(\hat{\eta}^{\text{graph}}(x, t), \hat{\phi}^{\text{graph}}(x, t))$. The components of $\hat{\theta}$ are ordered by interlacing $\hat{\phi}_k^{\text{graph}}(t_0)$ for k odd with $\hat{\eta}_k^{\text{graph}}(t_0)$ for k even, for $1 \leq k \leq d$. We set $d = 120$ in this calculation and used $M_1 = 324$ gridpoints. We did not use adaptive grids, so $N = 1$ in (4.8) and (4.9).

Panel (c) of figure 18 shows snapshots of solution P for $t \in \mathcal{T}_{12}$. The same data is shown as a contour plot in panel (a) of figure 19, except that solution P is evolved over a full period $-\frac{\pi}{2} \leq t \leq \frac{3\pi}{2}$ instead of a quarter period. The wave crest that forms at $(x, t) = (0, 0)$ appears again, shifted in space and time, at $(x, t) = (\pm\pi, \pi)$. Panels (b) and (c) of figure 19 show contour plots of the linearized solution $(\hat{\eta}^{\text{graph}}(x, t), \hat{\phi}^{\text{graph}}(x, t))$ with initial conditions $\hat{\theta}$. The solution was normalized to make $\hat{\theta}$ a unit vector in \mathbb{R}^d . The linearized velocity potential $\hat{\phi}^{\text{graph}}(x, t)$ is indistinguishable from zero at $t = 0$ and $t = \pi$ in the contour plot of panel (c). This is because $\dot{r} = J\hat{\theta}$ satisfies

$$\|\dot{r}\| = \left(\frac{1}{M_1} \sum_{m=0}^{M_1-1} \hat{\phi}^{\text{graph}}(x_{1m}, 0)^2 \right)^{1/2} = \sigma_{\min} = 3.4 \times 10^{-9}. \quad (\text{S8.1})$$

If $\hat{\phi}^{\text{graph}}$ were exactly zero at $t = 0$, a symmetry argument [31, 26, 29, 63] would ensure that $(\hat{\eta}^{\text{graph}}, \hat{\phi}^{\text{graph}})$ is time-periodic with period T and $\hat{\phi}^{\text{graph}}$ is zero again at $t = \pi$. The small

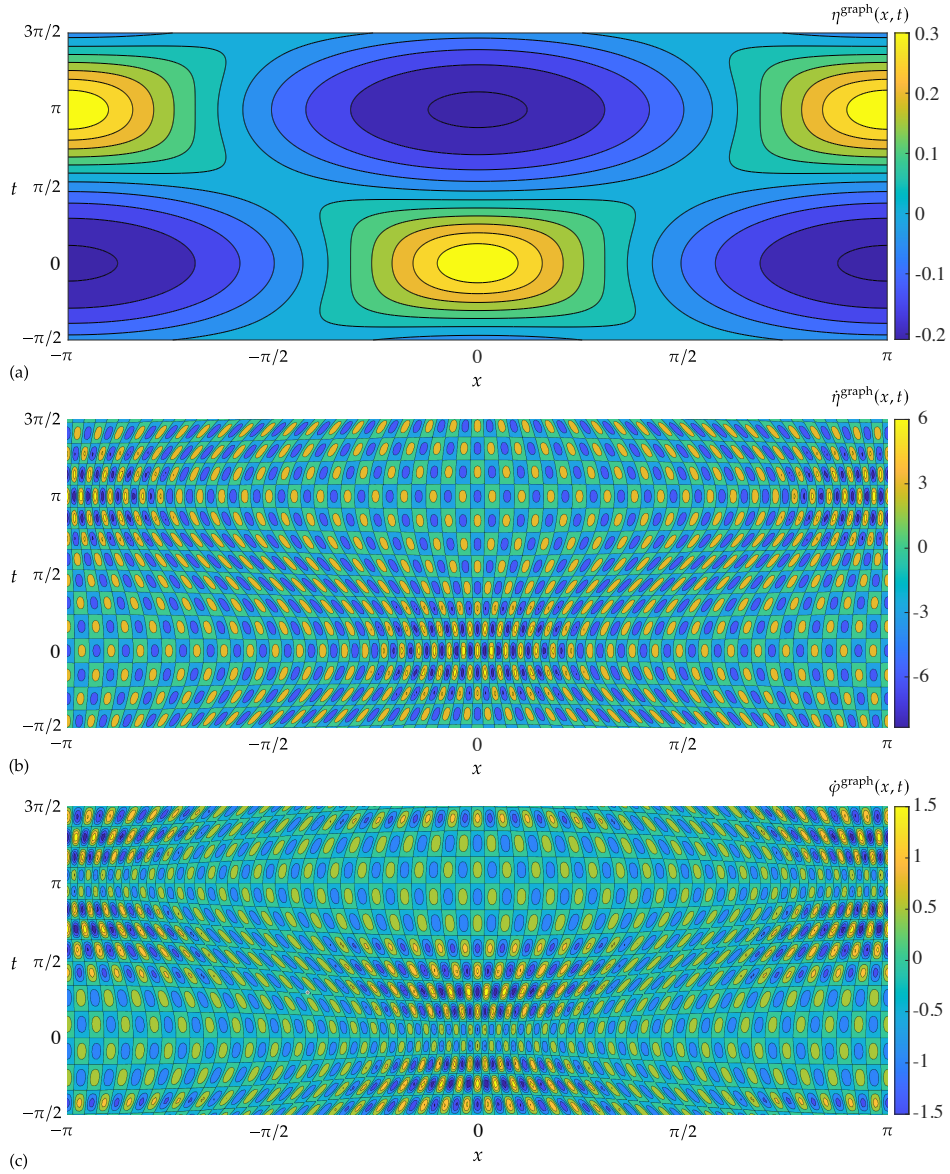


Fig. 19 Contour plot of $\eta^{\text{graph}}(x, t)$ for solution P over a full period and both components of the linearized solution about P with initial conditions given by $\hat{\theta}$, the right singular vector of J at P with the smallest singular value $\sigma_{\min} = 3.4 \times 10^{-9}$. This linearized solution gives the perturbation direction to an approximate secondary standing wave of the same period as solution P . There are 37 spatial oscillations and 7 temporal oscillations, but they are not uniform.

value of $\|\hat{r}\|$ in (S8.1) nearly achieves the same result, where we find that

$$\left(\frac{1}{M_1} \sum_{m=0}^{M_1-1} \left\{ \left[\dot{\eta}^{\text{graph}} \left(x_{1m}, \frac{3T}{4} \right) - \dot{\eta}^{\text{graph}} \left(x_{1m}, -\frac{T}{4} \right) \right]^2 + \left[\dot{\phi}^{\text{graph}} \left(x_{1m}, \frac{3T}{4} \right) - \dot{\phi}^{\text{graph}} \left(x_{1m}, -\frac{T}{4} \right) \right]^2 \right\} \right)^{1/2} = 8.2 \times 10^{-8} \quad (\text{S8.2})$$

and

$$\left(\frac{1}{M_1} \sum_{m=0}^{M_1-1} \dot{\phi}^{\text{graph}}(x_{1m}, T/2)^2 \right)^{1/2} = 1.08 \times 10^{-8}. \quad (\text{S8.3})$$

For reference on the size of the discrete L^2 norms in (S8.1)–(S8.3), we have

$$\left(\frac{1}{M_1} \sum_{m=0}^{M_1-1} \left[\dot{\eta}^{\text{graph}}(x_{1m}, -T/4)^2 + \dot{\phi}^{\text{graph}}(x_{1m}, -T/4)^2 \right] \right)^{1/2} = \sqrt{2}, \quad (\text{S8.4})$$

which follows from discrete orthogonality of the functions e^{ikx} on the grid $\{x_{1m}\}_{m=0}^{M_1-1}$ for $|k| < M_1/2$ together with $\|\dot{\theta}\| = 1$ and the fact that θ only contains positive-index Fourier modes in (4.10). We interpret $\dot{\eta}^{\text{graph}}(x, t)$ and $\dot{\phi}^{\text{graph}}(x, t)$ as the perturbation direction of a nearly time-periodic, infinitesimal secondary standing wave. Counting the oscillations in panels (b) and (c) shows that this bifurcation corresponds to the $(p, j) = (37, 7)$ harmonic resonance, but the sinusoidal pattern of the wave has been significantly distorted as it evolves over solution P , the primary wave of panel (a).

Our final task is to determine the phase of this secondary standing wave on the two bifurcation branches passing through NP and QR in panel (a) of figure 18. The main challenge is hidden by the extreme aspect ratio of the figure. The change in ϵ from point N to point P is 2.6×10^8 times larger than the change in $\hat{\eta}_{36}$, even though it looks like the bifurcation curve is nearly vertical from N to P in the plot. Most of the change in the initial condition θ from N to P is due to the dependence on ϵ of the underlying primary wave rather than the excitation of the secondary wave. Our idea is to filter this out by studying the alignment of the higher-frequency components of $(\theta_P - \theta_N)$ with those of $\dot{\theta}$. In panel (b) of figure 18, we plot the magnitudes of the components of $C(\theta_P - \theta_N)$ on top of those of $\dot{\theta}$, where $C = 5.1 \times 10^{15}$. This factor of C visually aligns the magnitudes of the components of $(\theta_P - \theta_N)$ with those of $\dot{\theta}$ over the range $33 \leq k \leq 60$.

The low-frequency components of $C(\theta_P - \theta_N)$ are large but decay rapidly. The dashed line shows the trend line if these modes had continued to decay geometrically at their initial decay rate. Instead, there is a growth phase beginning at $k = 28$ where the components of $(\theta_P - \theta_N)$ grow by 5 orders of magnitude before decaying again. We formed vectors u and v containing components $33 \leq k \leq 60$ of $(\theta_P - \theta_N)$ and $\dot{\theta}$, rescaled to make u and v unit vectors in \mathbb{R}^{28} . We find that the angle Θ between u and $-v$, computed via $\sin(\Theta/2) = \frac{1}{2}\|u - (-v)\|$, is $\Theta = 5.54 \times 10^{-8}$, which shows that the high-frequency components of $(\theta_P - \theta_N)$ are nearly perfectly aligned with those of $-\dot{\theta}$. Similarly, if we replace u by components $33 \leq k \leq 60$ of $(\theta_R - \theta_Q)$, the angle Θ between u and v , computed via $\sin(\Theta/2) = \frac{1}{2}\|u - v\|$, is also $\Theta = 5.54 \times 10^{-8}$. It was not necessary to recompute $\dot{\theta}$ at R when switching from $(\theta_P - \theta_N)$ to $(\theta_R - \theta_Q)$. The contour plots in panels (b) and (c) in figure 19 look identical whether we linearize around P or R . Since the sign of $\dot{\eta}^{\text{graph}}(0, 0)$ is positive in panel (b) of figure 19, we learn that following the bifurcation branch passing through Q and R leads to a secondary standing wave that is in phase with the primary wave, which sharpens the crest at $(x, t) = (0, 0)$ and increases ϵ . Following the branch passing through N and P leads to a secondary standing wave that is out of phase with the primary wave, which flattens the crest and decreases ϵ . A dimple would likely form at the crest if one follows the bifurcation branch far enough in that direction.

This method of studying the solution of the linearized problem about a standing wave near an imperfect bifurcation predicted by a Padé pole on the real ϵ -axis to classify the resonance responsible for the bifurcation is, to our knowledge, new, and is much less expensive than using numerical continuation to compute fully nonlinear solutions far out on

the bifurcation branches to directly observe the secondary standing waves that are excited by the resonance. It is interesting that $\hat{\eta}_{36}$ in figure 18 responds more strongly to the $(37, 7)$ resonance than $\hat{\phi}_{37}$. This shows that the strong deformation of the shape of the $(37, 7)$ resonance in panels (b) and (c) of figure 19 away from the tensor product form $\cos(37x) \cos(7t)$ and the change of variables from the graph-based formulation plotted in the figure to conformal variables have large effects on the Fourier modes $\hat{\eta}_p$ and $\hat{\phi}_p$ of the initial conditions in (4.12).